

AD-A200 825

NAVAL POSTGRADUATE SCHOOL Monterey, California



THESIS

AN INVESTIGATION OF FINITE DIFFERENCE
AND
FINITE ELEMENT VERTICAL SCHEMES
FOR THE BAROCLINIC PREDICTION EQUATIONS

by

Donn E. Sloniker

June 1988

Thesis Advisor
Co-Advisor

Roger Terry Williams
Beny Neta

Approved for public release; distribution is unlimited.

DTIC
ELECTE
DEC 01 1988
S & D
E

88 12 1 014

Unclassified

security classification of this page

REPORT DOCUMENTATION PAGE				
1a Report Security Classification Unclassified		1b Restrictive Markings		
2a Security Classification Authority		3 Distribution Availability of Report Approved for public release; distribution is unlimited.		
2b Declassification Downgrading Schedule				
4 Performing Organization Report Number(s)		5 Monitoring Organization Report Number(s)		
6a Name of Performing Organization Naval Postgraduate School	6b Office Symbol (if applicable) 35	7a Name of Monitoring Organization Naval Postgraduate School		
6c Address (city, state, and ZIP code) Monterey, CA 93943-5000		7b Address (city, state, and ZIP code) Monterey, CA 93943-5000		
8a Name of Funding Sponsoring Organization	8b Office Symbol (if applicable)	9 Procurement Instrument Identification Number		
8c Address (city, state, and ZIP code)		10 Source of Funding Numbers		
		Program Element No	Project No	Task No
		Work Unit Accession No		
11 Title (include security classification) AN INVESTIGATION OF FINITE DIFFERENCE AND FINITE ELEMENT VER- TICAL SCHEMES FOR THE BAROCLINIC PREDICTION EQUATIONS				
12 Personal Author(s) Donn E. Sloniker				
13a Type of Report Master's Thesis	13b Time Covered From To	14 Date of Report (year, month, day) June 1988	15 Page Count 117	
16 Supplementary Notation The views expressed in this thesis are those of the author and do not reflect the official policy or po- sition of the Department of Defense or the U.S. Government.				
17 Cosati Codes		18 Subject Terms (continue on reverse if necessary and identify by block number)		
Field	Group	Subgroup	numerical weather prediction, finite elements, finite differences, baroclinic instability	
19 Abstract (continue on reverse if necessary and identify by block number) <p>The vertical discretization in a linearized baroclinic prediction model was analyzed by comparing various finite element and finite difference solutions following Jordan (1985) and Shapiro (1987). The baroclinic instability experiments of Shapiro (1987) were augmented to include the unstaggered vertical scheme from Jordan (1985). Two basic wind profiles were used and the experiments were run with different resolution models and horizontal wavelengths. For a given wind profile and vertical resolution, different models performed better. The finite element models for the staggered vertical grids did not perform up to their possibilities due to the boundary elements. However, for the unstaggered vertical grid, the finite element model did better than the finite difference model in most cases.</p>				
20 Distribution Availability of Abstract <input checked="" type="checkbox"/> unclassified unlimited <input type="checkbox"/> same as report <input type="checkbox"/> DTIC users		21 Abstract Security Classification Unclassified		
22a Name of Responsible Individual Roger Terry Williams/Beny Neta		22b Telephone (include Area code) (408) 646-2296/2235	22c Office Symbol 63Wu/53Nd	

DD FORM 1473,84 MAR

83 APR edition may be used until exhausted
All other editions are obsolete

security classification of this page

Unclassified

Approved for public release; distribution is unlimited.

An Investigation of Finite Difference and
Finite Element Vertical Schemes
for the Baroclinic Prediction Equations

by

Donn E. Sloniker
Captain, United States Air Force
B.S., Brigham Young University, 1978

Submitted in partial fulfillment of the
requirements for the degree of

MASTER OF SCIENCE IN METEOROLOGY

from the

NAVAL POSTGRADUATE SCHOOL
June 1988

Author:



Donn E. Sloniker

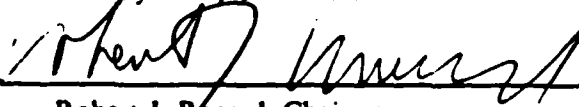
Approved by:



Roger Terry Williams, Thesis Advisor



Beny Neta, Co-Advisor



Robert J. Renard, Chairman,
Department of Meteorology



Gordon E. Schacher,
Dean of Science and Engineering

ABSTRACT

The vertical discretization in a linearized baroclinic prediction model was analyzed by comparing various finite element and finite difference solutions following Jordan (1985) and Shapiro (1987). The baroclinic instability experiments of Shapiro (1987) were augmented to include the unstaggered vertical scheme from Jordan (1985). Two basic wind profiles were used and the experiments were run with different resolution models and horizontal wavelengths. For a given wind profile and vertical resolution, different models performed better. The finite element models for the staggered vertical grids did not perform up to their possibilities due to the boundary elements. However, for the unstaggered vertical grid, the finite element model did better than the finite difference model in most cases.

Accession For	
NTIS GRA&I	<input checked="" type="checkbox"/>
DTIC TAB	<input type="checkbox"/>
Unannounced	<input type="checkbox"/>
Justification	
By	
Distribution/	
Availability Codes	
Dist	Avail and/or Special
A-1	



TABLE OF CONTENTS

I. INTRODUCTION	1
II. MODEL DESCRIPTIONS	4
A. MODEL FEATURES	4
B. GOVERNING EQUATIONS	4
C. TIME DIFFERENCING	9
D. VERTICAL GRIDS	10
E. FINITE DIFFERENCE MODELS	10
F. FINITE ELEMENT MODELS	11
1. FEM-A	11
2. FEM-B	15
3. FEM-C	17
III. EXPERIMENTS AND RESULTS	20
A. LINEAR VERTICAL SHEAR IN THE UBAR FIELD	21
1. Sixty-Layer Models	21
2. Six-Layer Models	22
3. Two-Layer Models	23
B. NONLINEAR VERTICAL SHEAR IN THE UBAR FIELD	23
1. Hyperbolic Shear Type I	23
a. Sixty-Layer Models	23
b. Six-layer Models	25
c. Four-Layer Models	27
d. Two-Layer Models	28
2. Hyperbolic Shear Type II	28
a. Sixty-Layer Models	28
b. Six-Layer Models	29
c. Four-Layer Models	30
d. Two-Layer Models	31
3. Hyperbolic Shear Type III	32
a. Sixty-Layer Models	32

b. Six-Layer Models	33
c. Four-Layer Models	35
d. Two-Layer Models	36
C. USING FINITE DIFFERENCE METHOD IN FINITE ELEMENT	
MODEL	36
1. Linear Vertical Shear in the ubar Field	37
2. Hyperbolic Type III Shear in the ubar Field	37
a. Sixty-Layer Model	37
b. Six-Layer Model	37
D. BACKWARD TILTING INITIAL VALUES	37
1. Linear Vertical Shear in the ubar Field	38
a. X-wavelength of 4000 km	38
b. X-wavelength of 3000 km	39
c. X-wavelength of 2000km	39
2. Hyperbolic Type III Shear in the ubar Field	39
a. X-wavelength of 4000 km	39
b. X-wavelength of 3000 km	39
c. X-wavelength of 2000 km	40
IV. CONCLUSIONS	89
APPENDIX A. FINITE DIFFERENCE APPROXIMATIONS	90
APPENDIX B. GALERKIN FORM OF FEM-A PROGNOSTIC EQUATIONS	92
APPENDIX C. BASIS FUNCTION EQUATIONS FOR FEM-A	95
APPENDIX D. GALERKIN FORM OF FEM-B PROGNOSTIC EQUATIONS	97
APPENDIX E. GALERKIN FORM OF FEM-C PROGNOSTIC EQUATIONS	99
LIST OF REFERENCES	102
INITIAL DISTRIBUTION LIST	104

LIST OF FIGURES

Fig. 1. Three vertical grids.	3
Fig. 2. Basis functions for grids A and B.	11
Fig. 3. Basis functions for grid C.	18
Fig. 4. 60-layer, 4000 km linear shear experiment at 96 h comparing v-component amplitudes (top) and phases (bottom).	41
Fig. 5. 60-layer, 4000 km linear shear experiment at 96 h comparing temperature amplitudes.	42
Fig. 6. 60-layer, 3000 km linear shear experiment at 96 h comparing v-component (top) and temperature (bottom) amplitudes.	43
Fig. 7. 60-layer, 2000 km linear shear experiment at 96 h comparing v-component amplitudes (top) and phases (bottom).	44
Fig. 8. 60-layer, 2000 km linear shear experiment at 96 h comparing temperature amplitudes.	45
Fig. 9. 6-layer, 4000 km linear shear experiment at 96 h comparing v-component amplitudes (top) and phases (bottom).	46
Fig. 10. 6-layer, 4000 km linear shear experiment at 96 h comparing temperature amplitudes.	47
Fig. 11. 6-layer, 3000 km linear shear experiment at 96 h comparing v-component amplitudes (top) and phases (bottom).	48
Fig. 12. 6-layer, 3000 km linear shear experiment at 96 h comparing temperature amplitudes.	49
Fig. 13. 6-layer, 2000 km linear shear experiment at 96 h comparing v-component amplitudes (top) and phases (bottom).	50
Fig. 14. 6-layer, 2000 km linear shear experiment at 96 h comparing temperature amplitudes.	51
Fig. 15. Hyperbolic tangent ubar profiles.	52
Fig. 16. 4-layer, 4000 km Type I shear experiment at 96 h comparing v-component amplitudes (top) and phases (bottom).	53
Fig. 17. 4-layer, 3000 km Type I shear experiment at 96 h comparing v-component amplitudes (top) and phases (bottom).	54
Fig. 18. 4-layer, 2000 km Type I shear experiment at 96 h comparing v-component	

amplitudes (top) and phases (bottom).	55
Fig. 19. 4-layer, 4000 km Type II shear experiment at 96 h comparing v-component amplitudes (top) and phases (bottom).	56
Fig. 20. 4-layer, 4000 km Type II shear experiment at 96 h comparing temperature amplitudes.	57
Fig. 21. 4-layer, 3000 km Type II shear experiment at 96 h comparing v-component amplitudes (top) and phases (bottom).	58
Fig. 22. 4-layer, 3000 km Type II shear experiment at 96 h comparing temperature amplitudes.	59
Fig. 23. 4-layer, 2000 km Type II shear experiment at 96 h comparing v-component amplitudes.	60
Fig. 24. 60-layer, 4000 km Type III shear experiment at 96 h comparing temperature amplitudes.	61
Fig. 25. 60-layer, 3000 km Type III shear experiment at 96 h comparing v-component amplitudes (top) and phases (bottom).	62
Fig. 26. 60-layer, 3000 km Type III shear experiment at 96 h comparing temperature amplitudes.	63
Fig. 27. 60-layer, 2000 km Type III shear experiment at 96 h comparing v-component amplitudes (top) and phases (bottom).	64
Fig. 28. 60-layer, 2000 km Type III shear experiment at 96 h comparing temperature amplitudes.	65
Fig. 29. 4-layer, 4000 km Type III shear experiment at 96 h comparing v-component amplitudes (top) and phases (bottom).	66
Fig. 30. 4-layer, 3000 km Type III shear experiment at 96 h comparing v-component amplitudes (top) and phases (bottom).	67
Fig. 31. 4-layer, 3000 km Type III shear experiment at 96 h comparing temperature amplitudes.	68
Fig. 32. 4-layer, 2000 km Type III shear experiment at 96 h comparing v-component amplitudes (top) and phases (bottom).	69
Fig. 33. 4-layer, 2000 km Type III shear experiment at 96 h comparing temperature amplitudes.	70
Fig. 34. 60-layer, 4000 km linear thermodynamic modification at 96 h comparing v-component amplitudes (top) and phases (bottom).	71
Fig. 35. 60-layer, 4000 km linear thermodynamic modification at 96 h comparing temperature amplitudes (top) and phases (bottom).	72

Fig. 36. 60-layer, 2000 km linear thermodynamic modification at 96 h comparing v-component amplitudes (top) and phases (bottom).	73
Fig. 37. 60-layer, 2000 km linear thermodynamic modification at 96 h comparing temperature amplitudes (top) and phases (bottom).	74
Fig. 38. 60-layer, 4000 km Type III thermodynamic modification at 96 h comparing v-component amplitudes (top) and phases (bottom).	75
Fig. 39. 60-layer, 4000 km Type III thermodynamic modification at 96 h comparing temperature amplitudes (top) and phases (bottom).	76
Fig. 40. 60-layer, 2000 km Type III thermodynamic modification comparing v-component (top) and temperature (bottom) amplitudes.	77
Fig. 41. 6-layer, 4000 km Type III thermodynamic modification at 96 h comparing v-component amplitudes (top) and phases (bottom).	78
Fig. 42. 6-layer, 4000 km Type III thermodynamic modification at 96 h comparing temperature amplitudes (top) and phases (bottom).	79
Fig. 43. 6-layer, 2000 km Type III thermodynamic modification at 96 h comparing v-component amplitudes (top) and phases (bottom).	80
Fig. 44. 6-layer, 2000 km Type III thermodynamic modification at 96 h comparing temperature amplitudes (top) and phases (bottom).	81
Fig. 45. 60-layer, 4000 km initial value modification (linear) comparing phase I (top) and phase II (bottom) negative phase tilt.	82
Fig. 46. 60-layer, 3000 km initial value modification (linear) comparing phase I (top) and phase II (bottom) negative phase tilt.	83
Fig. 47. 60-layer, 2000 km initial value modification (linear) comparing phase I (top) and phase II (bottom) amplitudes.	84
Fig. 48. 60-layer, 2000 km initial value modification (linear) comparing phase I (top) and phase II (bottom) negative phase tilt.	85
Fig. 49. 60-layer, 4000 km initial value modification (Type III) comparing phase I (top) and phase II (bottom) negative phase tilt.	86
Fig. 50. 60-layer, 3000 km initial value modification (Type III) comparing phase I (top) and phase II (bottom) negative phase tilt.	87
Fig. 51. 60-layer, 2000 km initial value modification (Type III) comparing phase I (top) and phase II (bottom) negative phase tilt.	88

ACKNOWLEDGMENTS

Thanks go to Mary Jordan who wrote the original numerical models used in this study and to Bruce Shapiro who made the models easy to use. I would like to thank Dr. R. Terry Williams for his help in designing the experiments and interpreting the results, and Dr. Beny Neta for his help in modifying the numerical models. My greatest thanks go to my wife, [REDACTED] for her support and understanding during the many hours that I was with the computer and not with her.

I. INTRODUCTION

At the present time, most numerical weather prediction models use finite differences to accomplish the vertical discretization even though they use finite difference, finite element, or spectral horizontal discretizations. The Canadian regional and hemispheric models (Staniforth and Daley, 1977 and 1979) which use finite elements in the vertical are an exception. The successful numerical prediction of synoptic evolutions requires a proper representation of the vertical variation of the predictive fields. Since smaller scale features such as fronts (Hoskins and Bretherton, 1972 and Williams, 1967) and the large scale planetary waves (Gall, 1976) are forced by energetic synoptic-scale features, it follows that all predictive scales of motion may be sensitive to the vertical discretization used in the numerical models.

Most of the finite difference vertical discretizations use a staggered arrangement of variables. Winninghoff (1968), Arakawa and Lamb (1977) and Schoenstadt (1980) demonstrated that staggering of variables in the horizontal improves geostrophic adjustment and the response to small scale forcing. Most quasi-geostrophic models (Charney and Phillips, 1953) use vertical staggering where the vertical motion and the temperature are carried between the levels which carry horizontal velocity and pressure. This arrangement will be referred to as grid B. Lorenz (1960) introduced a different grid for the balance equations which was designed to conserve energy. This arrangement places only the vertical velocity between the levels which carry the other variables (horizontal velocity, pressure and temperature) and will be referred to as grid A. Tokioka (1978) analyzed a number of vertical grids with linearized equations and found that grid A has a computational mode in the temperature field. Arakawa (1984) compared baroclinic instability for grids A and B in the linearized quasi-geostrophic equations. He found a false short wave instability for grid A which did not occur with grid B. This problem is related to the computational mode in the temperature field. Another difficulty with grid B is that the matrix which must be inverted to find the temperature from the pressure is singular. This is especially important for initialization. Many operational primitive equation models use grid A for energy conservation (Shapiro, 1987).

The use of finite elements for the vertical discretization can be expected to give a more accurate representation of vertical variations. The finite element method is a special case of the Galerkin procedure which represents the dependent variables with a

weighted sum of basis functions that have a prescribed spatial structure. The finite element method employs basis functions which are zero except in a limited region where they are low-order polynomials. This method has been used in engineering statics (e.g., Zienkiewicz, 1977) and it has been applied to fluid dynamics and hydrology (see Gray and Pinder, 1976). The finite element method has been successfully applied to meteorological prediction with the shallow water equations by Cullen (1973), Hinsman (1975) and Staniforth and Mitchell (1977, 1978). Cullen (1973), Neta *et al* (1986), and Neta and Williams (1986) demonstrated that finite element formulations with piecewise linear basis functions are more accurate than second order finite differences.

Jordan (1985) compared six linear, baroclinic, vorticity-divergence equation models using three grid schemes, grid A, grid B and an unstaggered grid. The three grids are depicted in Fig. 1. Shapiro (1987) improved the models for grids A and B, and corrected several problems in the heating and mountain forcing experiments. He also ran a baroclinic instability experiment without heating or mountain forcing using linear vertical shear in the mean wind profile. With the ever-increasing density of observations and the advent of satellite-based cloud pictures, transient disturbances of subsynoptic scales have been observed in certain preferred locations such as polar lows (Satyamurty *et al.* 1982). Satyamurty *et al* (1982) found that unstable modes can be generated at smaller horizontal wavelengths using hyperbolic tangent profiles. Farrell (1985) suggests that for backward tilting initial states the waves can experience rapid growth in the early stages and then settle into the most unstable growth.

The purpose of this study is to augment the baroclinic instability study by Shapiro (1987) by including the unstaggered models from Jordan (1985) and by looking at smaller resolution models and smaller wavelengths. Various hyperbolic tangent vertical profiles of the mean wind field are used to focus on more difficult baroclinic instability situations with smaller horizontal wavelengths and vertical scales, and with greater sensitivity to large local shears. This study also experiments with initial states which have a backward tilt with height in an effort to investigate the enhanced initial growth due to the tilt. The results of the experiments are given in Chapter III.

Z'_{n-1}	—————	$w = 0$	Z'_{n-1}	—————	$w = 0, T, \bar{T}, Q$
Z_{n-1}	-----	$\zeta, D, T, \bar{T}, u, \bar{u}, v, \phi, Q$	Z_{n-1}	-----	$\zeta, D, u, \bar{u}, v, \phi$
Z'_n	—————	w	Z'_n	—————	w, T, \bar{T}, Q
	⋮			⋮	
Z'_2	—————	w	Z'_2	—————	w, T, \bar{T}, Q
Z_2	-----	$\zeta, D, T, \bar{T}, u, \bar{u}, v, \phi, Q$	Z_2	-----	$\zeta, D, u, \bar{u}, v, \phi$
Z'_1	—————	w, ϕ, MTS	Z'_1	—————	$w, \phi, T, \bar{T}, Q, \text{MTS}$

GRID A

GRID B

Z'_{n-1}	—————	$\zeta, D, T, \bar{T}, u, \bar{u}, v, w, \phi, Q$

Z'_n	—————	$\zeta, D, T, \bar{T}, u, \bar{u}, v, w, \phi, Q$
	⋮	
Z'_2	—————	$\zeta, D, T, \bar{T}, u, \bar{u}, v, w, \phi, Q$

Z'_1	—————	$\zeta, D, T, \bar{T}, u, \bar{u}, v, w, \phi, Q, \text{MTS}$

GRID C

Fig. 1. Three vertical grids.

II. MODEL DESCRIPTIONS

A. MODEL FEATURES

Jordan (1985) developed six numerical models with several features to make easy modifications for a wide range of experiments. Shapiro (1987) modified the A and B models to improve the performance of the models near the boundary and used numerical integration to evaluate the entries of the matrices. He also added menus to make the transition between four experiments simple. The user is able to prescribe heating, mountain topography, velocity perturbation, or baroclinic experiments and the model will make the prescribed changes in the variables governing these cases. The vertical velocity vector in finite element model B has been corrected to include an additional element in an attempt to eliminate the oscillation in the temperature profile from Shapiro (1987). The two models for grid C have been modified to run baroclinic instability experiments and to include the same menus as the A and B models. Another menu has been added to all six models to select between linear and nonlinear wind shear profiles. The models are written in modular structure using FORTRAN 77. There is parallel construction between models. The subroutines used in one model are very similar to those used in the other models. The models can run quickly on an IBM-3033 mainframe. For example, a 96-hour forecast for a 6-layer finite element model uses less than six seconds of computer processing time; however, the same forecast for 60 layers can take up to 220 seconds.

B. GOVERNING EQUATIONS

Each model approximates the same set of governing equations. The vorticity equation (2.1), the divergence equation (2.2), the surface geopotential equation (2.3), and the first law of thermodynamics (2.4) are the prognostic equations for the forecast variables vorticity, divergence, surface geopotential and potential temperature. The surface geopotential equation is the lower boundary condition on the vertical velocity. The vertical coordinate $Z = -\ln(p/p_0)$ is used, but the non-boussinesq terms involving e^{-Z} are replaced by one. The prognostic equations in the coordinates x , y , Z and t are

$$\frac{d\zeta}{dt} + (\zeta + f)D + \beta v + \frac{\partial w}{\partial x} \frac{\partial v}{\partial Z} - \frac{\partial w}{\partial y} \frac{\partial u}{\partial Z} = 0, \quad (2.1)$$

$$\begin{aligned} \frac{dD}{dt} + \left(\frac{\partial u}{\partial x} \right)^2 + \left(\frac{\partial v}{\partial y} \right)^2 + 2 \frac{\partial u}{\partial y} \frac{\partial v}{\partial x} + \frac{\partial w}{\partial x} \frac{\partial u}{\partial z} + \frac{\partial w}{\partial y} \frac{\partial v}{\partial z} \\ + \beta u - f\zeta + \nabla^2 \phi = 0, \end{aligned} \quad (2.2)$$

$$\frac{d\phi_s}{dt} = \text{MTS and} \quad (2.3)$$

$$\frac{dT}{dt} = Q. \quad (2.4)$$

In these equations,

ζ is the vertical component of vorticity, $\zeta = \frac{\partial v}{\partial x} - \frac{\partial u}{\partial y}$,

D is the horizontal divergence, $D = \frac{\partial u}{\partial x} + \frac{\partial v}{\partial y}$,

ϕ is the geopotential, $\phi = gZ$,

ϕ_s is the surface geopotential,

T is the potential temperature,

u is the x-component of velocity,

v is the y-component of velocity,

w is the vertical velocity,

Q is the diabatic heating per unit time per unit mass,

MTS is the forced vertical velocity due to flow over mountain topography,

f is the Coriolis parameter,

β is df/dy ,

$$\frac{d(\)}{dt} = \frac{\partial(\)}{\partial t} + u \frac{\partial(\)}{\partial x} + v \frac{\partial(\)}{\partial y} + w \frac{\partial(\)}{\partial z} \quad \text{and}$$

∇^2 is the horizontal Laplacian operator.

The prognostic equations are linearized by expanding the variables into their mean and perturbation states, as in Jordan (1985). The resulting linearized forecast equations are

$$\frac{\partial \zeta'}{\partial t} = -fD' - \bar{u} \frac{\partial \zeta'}{\partial x} - \beta v', \quad (2.5)$$

$$\frac{\partial D'}{\partial t} = f\zeta' - \bar{u} \frac{\partial D'}{\partial x} - \beta u' - \frac{\partial w'}{\partial x} \frac{d\bar{u}}{dZ} - \frac{\partial^2 \phi'}{\partial x^2}, \quad (2.6)$$

$$\frac{\partial \phi_s'}{\partial t} = -\bar{u} \frac{\partial \phi_s'}{\partial x} - v' \frac{\partial \bar{\phi}_s}{\partial y} - R\bar{T}w' + MTS' \text{ and} \quad (2.7)$$

$$\frac{\partial T'}{\partial t} = -\bar{u} \frac{\partial T'}{\partial x} - v' \frac{\partial \bar{T}}{\partial y} - w' \frac{\partial \bar{T}}{\partial Z} + Q', \quad (2.8)$$

where R is the gas constant for air, $(')$ denotes perturbation quantities and $(\bar{})$ denotes mean quantities. The use of \bar{X} in the text will be used to denote mean quantities of a variable X (Shapiro, 1987).

The diagnostic variables, u' , v' , w' and ζ' , are calculated from the forecast variables using the definitions of divergence, vorticity, the hydrostatic equation and the continuity equation. The relationships are given in equations (2.9) through (2.12).

$$\frac{\partial u'}{\partial x} = D'. \quad (2.9)$$

$$\frac{\partial v'}{\partial x} = \zeta'. \quad (2.10)$$

$$\frac{\partial \phi'}{\partial Z} = RT'. \quad (2.11)$$

$$D' + \frac{\partial w'}{\partial Z} = 0. \quad (2.12)$$

The use of primes to denote perturbation quantities will be discontinued. All quantities used in the remainder of the paper will be perturbation quantities unless otherwise noted.

The mean state is assumed to be in hydrostatic and geostrophic balance. The term $\partial \bar{T}/\partial y$ in the first law of thermodynamics can be evaluated by taking $\partial/\partial y$ of the hydrostatic equation and substituting for $\partial \bar{\phi}/\partial y$ from the geostrophic relation, $\partial \bar{\phi}/\partial y = -f\bar{u}$. Thus,

$$\frac{\partial \bar{T}}{\partial y} = -\frac{f}{R} \frac{\partial \bar{u}}{\partial Z}. \quad (2.13)$$

Geostrophic balance of the mean state at the surface implies

$$\frac{\partial \bar{\phi}_s}{\partial y} = -f \bar{u}_{sfc}. \quad (2.14)$$

The expressions (2.13) and (2.14) are substituted into equations (2.8) and (2.7), respectively.

A singlewave spectral representation is used in the x-direction, with wave number $\mu = 2\pi/L$, where L is the wavelength in the x-direction. The perturbation quantities have the form

$$\zeta(x, Z, t) = A_1(Z, t) \cos \mu x + A_2(Z, t) \sin \mu x, \quad (2.15)$$

$$D(x, Z, t) = D_1(Z, t) \cos \mu x + D_2(Z, t) \sin \mu x, \quad (2.16)$$

$$T(x, Z, t) = T_1(Z, t) \cos \mu x + T_2(Z, t) \sin \mu x, \quad (2.17)$$

$$\phi_s(x, Z, t) = S_1(Z, t) \cos \mu x + S_2(Z, t) \sin \mu x, \quad (2.18)$$

$$u(x, Z, t) = U_1(Z, t) \cos \mu x + U_2(Z, t) \sin \mu x, \quad (2.19)$$

$$v(x, Z, t) = V_1(Z, t) \cos \mu x + V_2(Z, t) \sin \mu x, \quad (2.20)$$

$$w(x, Z, t) = W_1(Z, t) \cos \mu x + W_2(Z, t) \sin \mu x, \quad (2.21)$$

$$\phi(x, Z, t) = H_1(Z, t) \cos \mu x + H_2(Z, t) \sin \mu x, \quad (2.22)$$

$$Q(x, Z, t) = Q_1(Z, t) \cos \mu x + Q_2(Z, t) \sin \mu x \text{ and} \quad (2.23)$$

$$MTS(x, Z, t) = MTS_1(Z, t) \cos \mu x + MTS_2(Z, t) \sin \mu x. \quad (2.24)$$

The relations (2.15) through (2.24) are substituted into equations (2.5) through (2.12). The prognostic and diagnostic equations are separated into equations for the cosine and the sine terms. The resultant prognostic equations are

$$\frac{\partial A_1}{\partial t} = -f D_1 - \bar{u} \mu A_2 - \beta V_1, \quad (2.25)$$

$$\frac{\partial A_2}{\partial t} = -f D_2 + \bar{u} \mu A_1 - \beta V_2, \quad (2.26)$$

$$\frac{\partial D_1}{\partial t} = fA_1 - \bar{u}\mu D_2 - \beta U_1 - \mu \frac{d\bar{u}}{dZ} W_2 + \mu^2 H_1, \quad (2.27)$$

$$\frac{\partial D_2}{\partial t} = fA_2 + \bar{u}\mu D_1 - \beta U_2 + \mu \frac{d\bar{u}}{dZ} W_1 + \mu^2 H_2, \quad (2.28)$$

$$\frac{\partial T_1}{\partial t} = -\bar{u}\mu T_2 + \frac{f}{R} \frac{d\bar{u}}{dZ} V_1 - \frac{\partial \bar{T}}{\partial Z} W_1 + Q_1, \quad (2.29)$$

$$\frac{\partial T_2}{\partial t} = \bar{u}\mu T_1 + \frac{f}{R} \frac{d\bar{u}}{dZ} V_2 - \frac{\partial \bar{T}}{\partial Z} W_2 + Q_2, \quad (2.30)$$

$$\frac{\partial S_1}{\partial t} = -\bar{u}\mu S_2 + f\bar{u}_{sfc} V_1 - R\bar{T}W_1 + MTS_1 \text{ and} \quad (2.31)$$

$$\frac{\partial S_2}{\partial t} = \bar{u}\mu S_1 + f\bar{u}_{sfc} V_2 - R\bar{T}W_2 + MTS_2. \quad (2.32)$$

The resultant diagnostic equations for u and v are

$$U_1 = -\frac{D_2}{\mu}, \quad (2.33)$$

$$U_2 = \frac{D_1}{\mu}, \quad (2.34)$$

$$V_1 = -\frac{A_2}{\mu} \text{ and} \quad (2.35)$$

$$V_2 = \frac{A_1}{\mu}. \quad (2.36)$$

Geopotential values above the surface are obtained by integrating the hydrostatic equation from the surface ($Z = Z_0$) to height Z .

$$H_1 = R \int_{Z_0}^Z T_1(Z,t) dZ + S_1 \text{ and} \quad (2.37)$$

$$H_2 = R \int_{Z_0}^Z T_2(Z,t) dZ + S_2. \quad (2.38)$$

The vertical velocity is calculated by integrating the continuity equation from the top of the atmosphere ($Z = Z_T$) down to height Z . The upper boundary condition, $w = 0$ at $Z = Z_T$, is used. The diagnostic equations for the vertical velocity are

$$W_1 = \int_Z^{Z_T} D_1(Z,t) dZ \text{ and} \quad (2.39)$$

$$W_2 = \int_Z^{Z_T} D_2(Z,t) dZ. \quad (2.40)$$

Equations (2.25) through (2.40) are the prognostic and diagnostic equations that govern all six numerical models. Using the given basic state and the one-wave spectral perturbation quantities, the governing equations reduce to functions of Z and t . The models are effectively one-dimensional (Shapiro, 1987).

To display the results of each model, the sine and cosine amplitudes of each variable are combined to determine the amplitude and phase of a single cosine wave in the x -direction. A typical variable has the form:

$$Y(x,Z,t) = A(Z,t) \cos(\mu x - \delta), \quad (2.41)$$

where the amplitude is $A(Z,t)$ and the phase is $\delta(Z,t)$. The amplitude and phase are calculated at each level for all variables.

C. TIME DIFFERENCING

Two forward time steps are taken to start each model and then leapfrog time differencing is used. The leapfrog scheme is a higher order scheme than forward differencing and is the one used in many numerical models. A Robert filter is used to reduce the amplitude of the computational mode generated by the leapfrog time differencing. The filter is discussed by Haltiner and Williams (1980). For a prognostic variable F , calculate \bar{F}_{n-1} , the average value of F at time step $(n-1)\Delta t$, using equation (2.42),

$$\bar{F}_{n-1} = F_{n-1} + \gamma(F_n - 2F_{n-1} + \bar{F}_{n-2}), \quad (2.42)$$

where γ is a weighting function. Using the unaveraged values at time step $n\Delta t$, compute the tendency $(\partial F / \partial t)_n$ from its predictive equation. The predicted value at time step $(n+1)\Delta t$ is then calculated using equation (2.43),

$$F_{n+1} = \bar{F}_{n-1} + 2\Delta t \left(\frac{\partial F}{\partial t} \right)_n. \quad (2.43)$$

In all the experiments, $\gamma = 0.05$ is used. The time step for each experiment is calculated in the model by requiring, for computational stability,

$$v\Delta t = \frac{1}{2}, \quad (2.44)$$

where $v = \mu c$ and c is the typical phase speed of an external gravity wave.

D. VERTICAL GRIDS

Each of the models uses one of three vertical grids. The three methods for distributing the variables over discrete levels are depicted in Fig. 1. The staggered levels are represented by the dashed lines in Fig. 1. Notice that the heights at which the variables are defined change between the three grids. The notation used in this paper to denote the staggered and unstaggered levels is consistent with the conventions used in the coded models. The height of the unstaggered levels is denoted as Z' . The height of the staggered levels is denoted as Z . In the models, both Z_1' and Z_1 are defined to be the surface of the earth. It is assumed that the staggered level Z_1 is exactly in the middle of the layer between Z_{1-1}' and Z_1' . This distinction is important because the models can have layers with unequal depth. Thus, the height of the staggered levels is defined relative to the height of the unstaggered levels.

A finite difference model is written for each of the grid structures. The models are denoted as FDM-A, FDM-B and FDM-C. Similarly, finite element models using the three grids are indicated by FEM-A, FEM-B and FEM-C.

E. FINITE DIFFERENCE MODELS

The only differences in the equations between the three FDM models are the approximations of terms involving $\partial \bar{u} / \partial Z$ and $\partial \bar{T} / \partial Z$ in the prognostic equations and the approximations of the integral in the diagnostic geopotential equation. Centered difference approximations are used, except at the boundaries where one-sided differences are used. The finite difference approximations used in the prognostic equations are listed in Appendix A.

F. FINITE ELEMENT MODELS

1. FEM-A

The FEM-A model defines vertical velocity (w) at the unstaggered levels in terms of the basis functions $\psi_j(Z)$. The other variables are defined at the staggered levels in terms of the basis functions $\phi_j(Z)$. The expansion for a typical term is

$$A_j(Z, t) = \sum_{j=1}^{n+1} A_j^i(t) \psi_j(Z) \quad \text{or} \quad \sum_{j=1}^{n+1} A_j^i(t) \phi_j(Z). \quad (2.45)$$

The basis functions for this model are depicted in Fig. 2. The basis functions $\psi(Z)$ are defined for the unstaggered levels (solid lines at height Z') and the basis functions $\phi(Z)$ are defined for the staggered levels (dashed lines at height Z).

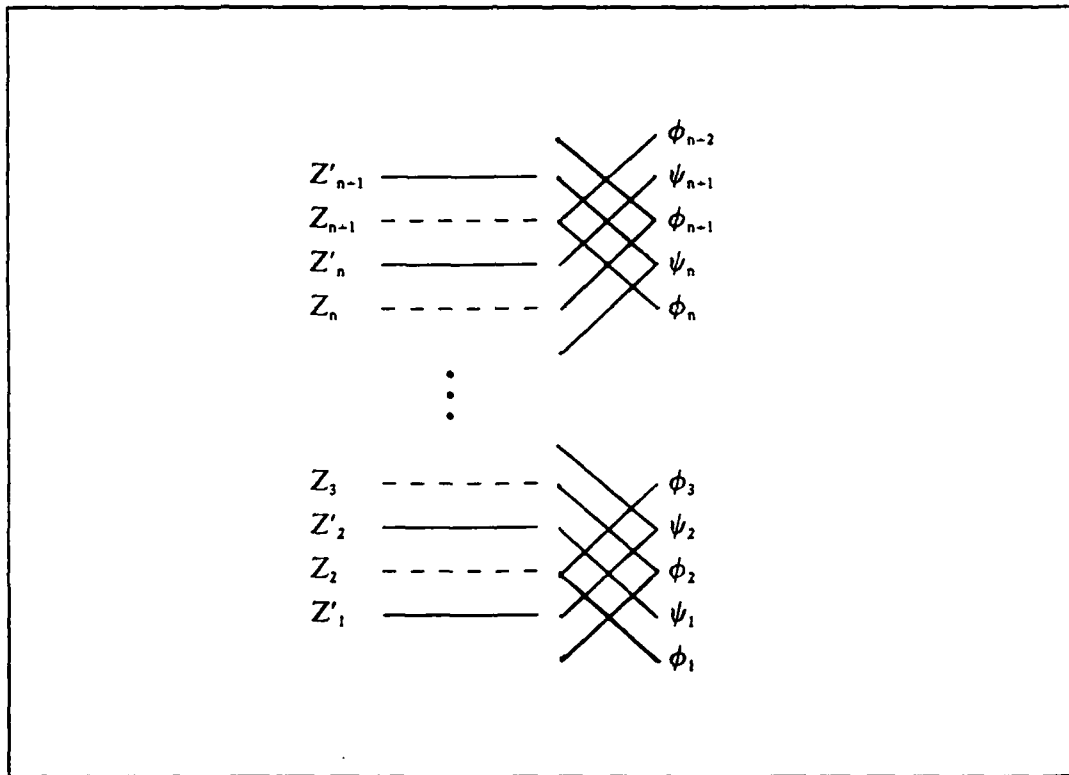


Fig. 2. Basis functions for grids A and B.

The finite element approximations for the vorticity, divergence and thermodynamic equations are derived by substituting the expansion for each dependent variable into equations (2.25) through (2.30). Each equation is multiplied by $\psi_i(Z)$ and

integrated with respect to Z from the bottom to the top of the atmosphere. Each term in the equations is the finite sum of separate integrals. Only the integrals of overlapping basis functions are nonzero. The resultant equations, listed in Appendix B, are matrix equations. For an n -layer model, the vectors $A_1, A_2, D_1, D_2, H_1, H_2, Q_1, Q_2, T_1, T_2, U_1, U_2, V_1$ and V_2 , contain $n+2$ components. The vectors W_1 and W_2 contain $n+1$ components. The matrices M, K , and Φ , defined below, are $(n+2) \times (n+2)$ matrices. The matrix P , defined below, is an $(n+1) \times (n+2)$ matrix. The mass matrix M for this model is defined by

$$M_{ij} = \int_{Z_0}^{Z_T} \phi_j(Z) \phi_i(Z) dZ \quad \text{for } |i-j| \leq 1. \quad (2.46)$$

The matrix K is defined for terms multiplied by \bar{u} ,

$$K_{ij}(\bar{u}) = \sum_{k=i-1}^{i+1} \bar{u}^k \int_{Z_0}^{Z_T} \phi_j(Z) \phi_k(Z) \phi_i(Z) dZ \quad \text{for } |i-j| \leq 1. \quad (2.47)$$

The matrix P is defined for terms multiplied by $\frac{d\bar{u}}{dZ} W$, or by $\frac{\partial \bar{T}}{\partial Z} W$,

$$P_{ij}(\bar{x}) = \sum_{k=i-1}^{i+1} \bar{x}^k \int_{Z_0}^{Z_T} \frac{d\phi_k}{dZ} \phi_j(Z) \phi_i(Z) dZ \quad \text{for } |i-j| \leq 1, \quad (2.48)$$

where \bar{x} is \bar{u} or \bar{T} .

The matrix Φ is defined for terms multiplied by $\frac{d\bar{u}}{dZ} V$,

$$\Phi_{ij}(\bar{u}) = \sum_{k=i-1}^{i+1} \bar{u}^k \int_{Z_0}^{Z_T} \frac{d\phi_k}{dZ} \phi_j(Z) \phi_i(Z) dZ \quad \text{for } |i-j| \leq 1. \quad (2.49)$$

The staggered basis functions present two general problems for evaluating the elements of the four matrices. First, for an n -layer model, portions of basis functions $\phi_1(Z)$ and $\phi_{n+2}(Z)$ are defined in the model atmosphere but the physical meaning of contributions from those terms is unclear. The contributions are included in the first

two rows and the last row of each matrix. Second, only portions of basis functions $\phi_2(Z)$ and $\phi_{n-1}(Z)$ are defined in the model atmosphere. To describe the incomplete sides of both basis functions an assumption must be made about the value of ϕ_2 at the surface and ϕ_{n-1} at the top of the atmosphere.

Assumptions are made and procedures are developed in an attempt to resolve these problems. In this model, the mean state variables, \bar{u} and \bar{T} , are defined only at the n staggered levels. However, \bar{u} and \bar{T} values defined at the nodal points of $\phi_1(Z)$ and $\phi_{n-2}(Z)$ are important in the Galerkin formulation of the $\partial \bar{u} / \partial Z$ and $\partial \bar{T} / \partial Z$ terms. In these experiments, the values of \bar{u} and \bar{T} are defined at the surface and top of the atmosphere. Jordan (1985) did not define them at the nodal points of $\phi_1(Z)$ and $\phi_{n-2}(Z)$. One of Shapiro's (1987) major modifications of these experiments was to define \bar{u} and \bar{T} at the nodal points of $\phi_1(Z)$ and $\phi_{n-2}(Z)$. For constant shear with height, \bar{u} and \bar{T} are defined at the boundaries such that the shear in the two half layers at the boundaries is the same as the shear in the other layers. To evaluate the staggered basis functions defined in the layers between the surface and Z_2 , and Z_{n-1} and the top of the atmosphere, it is assumed that the value at the boundaries of those basis functions is one-half. Thus, three-fourths of the basis functions $\phi_2(Z)$ and $\phi_{n-1}(Z)$ are defined in the model atmosphere.

The equations for the general elements of the four matrices are evaluated by substituting into equations (2.46) through (2.49) the formulas for $\phi_{i-1}(Z)$, $\phi_i(Z)$, $\phi_{i+1}(Z)$, $\psi_{i-1}(Z)$, $\psi_i(Z)$, $\psi_{i+1}(Z)$, and $\psi_{i+2}(Z)$, in terms of the local coordinate $\xi = Z - Z_i$. The equations for these basis functions defined for levels 1, 2, i , and $n+1$ are listed in Appendix C. The matrices were evaluated by integrating numerically using 2 point Gaussian Quadratures as in Shapiro (1987).

The vorticity, divergence and thermodynamic equations, written in matrix and vector form, are

$$M \frac{dA_1}{dt} = M(-fD_1 - \beta V_1) - \mu K(\bar{u})A_2, \quad (2.50)$$

$$M \frac{dA_2}{dt} = M(-fD_2 - \beta V_2) + \mu K(\bar{u})A_1, \quad (2.51)$$

$$M \frac{dD_1}{dt} = M(fA_1 - \beta U_1 + \mu^2 H_1) - \mu K(\bar{u})D_2 - \mu P(\bar{u})W_2, \quad (2.52)$$

$$M \frac{dD_2}{dt} = M(fA_2 - \beta U_2 + \mu^2 H_2) + \mu K(\bar{u})D_1 - \mu P(\bar{u})W_1, \quad (2.53)$$

$$M \frac{dT_1}{dt} = -\mu K(\bar{u})T_2 + \frac{f}{R} \Phi(\bar{u})V_1 - P(\bar{T})W_1 + MQ_1 \text{ and} \quad (2.54)$$

$$M \frac{dT_2}{dt} = \mu K(\bar{u})T_1 + \frac{f}{R} \Phi(\bar{u})V_2 - P(\bar{T})W_2 + MQ_2. \quad (2.55)$$

Equations (2.50) through (2.55) are simplified by multiplying each equation by M^{-1} and applying the Robert filter. Actually, one should not compute the inverse of M . Instead, at $t=0$ one should obtain the LU factorization of M . Thus, at each time step one only needs to forward and back solve a triangular system. The matrices $M^{-1}K$, $M^{-1}P$ and $M^{-1}\Phi$ are constants. They are constructed in the initialization subroutine and stored for use in the forecast subroutine. The matrices are multiplied by the appropriate vectors with values for time level $n\Delta t$. The resultant forecast equations are vector equations and the forecast value for the i -th vertical level is the sum of values in the i -th location of each vector equation. The prognostic equations for the vorticity, divergence and potential temperature vectors are

$$A_{1(n+1)} = A_{1(n-1)} + 2\Delta t(-fD_1 - \beta V_1 - \mu M^{-1}K(\bar{u})A_2)_{(n)}, \quad (2.56)$$

$$A_{2(n+1)} = A_{2(n-1)} + 2\Delta t(-fD_2 - \beta V_2 + \mu M^{-1}K(\bar{u})A_1)_{(n)}, \quad (2.57)$$

$$D_{1(n+1)} = D_{1(n-1)} + 2\Delta t(fA_1 - \beta U_1 + \mu^2 H_1 - \mu M^{-1}K(\bar{u})D_2 - \mu M^{-1}P(\bar{u})W_2)_{(n)}, \quad (2.58)$$

$$D_{2(n+1)} = D_{2(n-1)} + 2\Delta t(fA_2 - \beta U_2 + \mu^2 H_2 - \mu M^{-1}K(\bar{u})D_1 + \mu M^{-1}P(\bar{u})W_1)_{(n)}, \quad (2.59)$$

$$T_{1(n+1)} = T_{1(n-1)} + 2\Delta t(-\mu M^{-1}K(\bar{u})T_2 + \frac{f}{R} M^{-1}\Phi(\bar{u})V_1 - M^{-1}P(\bar{T})W_1 + Q_1)_{(n)} \text{ and} \quad (2.60)$$

$$T_{2(n+1)} = T_{2(n-1)}$$

$$+ 2\Delta t(\mu M^{-1}K(\bar{u})T_1 + \frac{f}{R} M^{-1}\Phi(\bar{u})V_2 - M^{-1}P(\bar{T})W_2 + Q_2)_{(n)}, \quad (2.61)$$

where the subscripts $(n+1)$, (n) and $(n-1)$ refer to the values of the vectors at time step $(n+1)\Delta t$, $n\Delta t$ and $(n-1)\Delta t$, respectively. The surface geopotential and the diagnostic variables are calculated using the corresponding equations in model FDM-A (see Appendix A).

2. FEM-B

The FEM-B model defines vertical velocity, potential temperature, mean state potential temperature and diabatic heating at the unstaggered levels in terms of the basis functions $\psi_i(Z)$. The other variables are defined at the staggered levels in terms of the basis functions $\phi_i(Z)$. The basis functions are the same as defined for the FEM-A model, shown in Fig. 2.

The finite element approximations for the vorticity, divergence and thermodynamic equations are derived by substituting the expansion for each dependent variable into equations (2.25) through (2.30). The vorticity and divergence equations are multiplied by $\phi_i(Z)$ and integrated with respect to Z from the bottom to the top of the atmosphere. The resultant Galerkin formulation of the vorticity and divergence equations are the same as those derived for model FEM-A. The matrices in those equations, M , K and P are given by equations (2.46) through (2.48) as defined for FEM-A. The thermodynamic equations are multiplied by $\psi_i(Z)$ because potential temperature is defined at the unstaggered levels. As before, the equations are integrated through the depth of the atmosphere. The resultant equations are listed in Appendix D. Four additional matrices are defined for the two thermodynamic equations. The mass matrix Π is

$$\Pi_{ij} = \int_{Z_0}^{Z_T} \psi_j(Z)\psi_i(Z)dZ \quad \text{for } |i-j| \leq 1. \quad (2.62)$$

The matrix Γ is defined for terms multiplied by \bar{u} ,

$$\Gamma_{ij}(\bar{u}) = \sum_{k=i-1}^{i+1} \bar{u}^k \int_{Z_0}^{Z_T} \psi_j(Z) \phi_k(Z) \psi_i(Z) dZ \quad \text{for } |i-j| \leq 1. \quad (2.63)$$

Terms multiplied by $\frac{d\bar{u}}{dZ} V$, give rise to the transpose of the matrix \mathbf{P} , defined by (2.48). The matrix Ψ is defined for terms multiplied by $\frac{\partial \bar{T}}{\partial Z} W$,

$$\Psi_{ij}(\bar{T}) = \sum_{k=i-1}^{i+1} \bar{T}^k \int_{Z_0}^{Z_T} \frac{d\psi_k}{dZ} \psi_j(Z) \psi_i(Z) dZ \quad \text{for } |i-j| \leq 1. \quad (2.64)$$

As discussed in the FEM-A model description, the staggered finite elements present problems for evaluating the elements of the matrices. In this model, \bar{u} is defined at the surface, the top of the atmosphere and at the n staggered levels. The mean state temperature, \bar{T} , is defined at the unstaggered levels so special definitions for it are not needed. Jordan (1985) did not include the contributions from the perturbation quantities defined at the nodal points of $\phi_i(Z)$ and $\phi_{n+2}(Z)$. They were included in this model as part of the Shapiro (1987) modifications. The staggered basis functions, $\phi_i(Z)$, are evaluated at the boundaries using the assumptions discussed in the previous section.

The elements of matrices Π , Γ , and Ψ are evaluated by substituting formulas for $\phi_{i-2}(Z)$, $\phi_{i-1}(Z)$, $\phi_i(Z)$, $\phi_{i+1}(Z)$, $\psi_{i-1}(Z)$, $\psi_i(Z)$, and $\psi_{i+1}(Z)$ defined in terms of the local coordinate $\xi = Z - Z_i$, into equations (2.62), (2.63) and (2.64). Formulas for these basis functions are listed in Appendix C. As in FEM-A, the matrices are evaluated by integrating numerically using 2 point Gaussian Quadratures.

The forecast matrix equations for vorticity, divergence and temperature are as described for model FEM-A. The final form of the vorticity and divergence vector equations are the same as for model FEM-A, equations (2.56) through (2.59). The thermodynamic vector equations are

$$\begin{aligned} T_{1(n+1)} &= T_{1(n-1)} \\ &+ 2\Delta t \left(-\mu \Pi^{-1} \Gamma(\bar{u}) T_2 + \frac{f}{R} \Pi^{-1} \mathbf{P}^T(\bar{u}) V_1 - \Pi^{-1} \Psi(\bar{T}) W_1 + Q_1 \right)_{(n)}, \end{aligned} \quad (2.65)$$

$$T_{2(n+1)} = T_{2(n-1)}$$

$$+ 2\Delta t(\mu\Pi^{-1}\Gamma(\bar{u})T_1 + \frac{f}{R}\Pi^{-1}P^T(\bar{u})V_2 - \Pi^{-1}\Psi(\bar{T})W_2 + Q_2)_{(n)}, \quad (2.66)$$

In this model, the vectors $A_1, A_2, D_1, D_2, H_1, H_2, U_1, U_2, V_1, V_2, W_1$ and W_2 , contain $n+2$ components. The vectors Q_1, Q_2, T_1 and T_2 contain $n+1$ components. Shapiro (1987) defined vectors W_1 and W_2 with $n+1$ components; however, since W_1 and W_2 are derived using vectors D_1 and D_2 (which have $n+2$ components) in equations (2.39) and (2.40), W_1 and W_2 have been increased to $n+2$ components. The matrices Π, Γ , and Ψ , are $(n+1) \times (n+1)$ matrices and the matrix P^T is an $(n+2) \times (n+1)$ matrix. The surface geopotential and the diagnostic variables are calculated using the corresponding equations in model FDM-B.

3. FEM-C

The unstaggered FEM model is the simplest of the three FEM models. Each of the dependent variables is expanded in terms of the basis functions $\phi_j(Z)$. The expansion for a typical term is

$$A_1(Z,t) = \sum_{j=1}^{n+1} A_1^j(t)\phi_j(Z). \quad (2.67)$$

The basis functions for this model are depicted in Fig. 3.

The finite element approximations for the vorticity, divergence and thermodynamic equations are derived by substituting the expansion for each dependent variable into equations (2.25) through (2.30). Each equation is multiplied by $\phi_i(Z)$ and integrated with respect to Z from the bottom to the top of the atmosphere. Each term in the equations is the finite sum of separate integrals. Only the integrals of overlapping basis functions are nonzero. The resultant equations, listed in Appendix E, are matrix equations. The matrices M and K are given by equations (2.46) and (2.47) as defined for FEM-A. The matrix E is defined for terms multiplied by $\frac{d\bar{u}}{dZ} V$, by $\frac{d\bar{u}}{dZ} W$, or by $\frac{\partial \bar{T}}{\partial Z} W$.

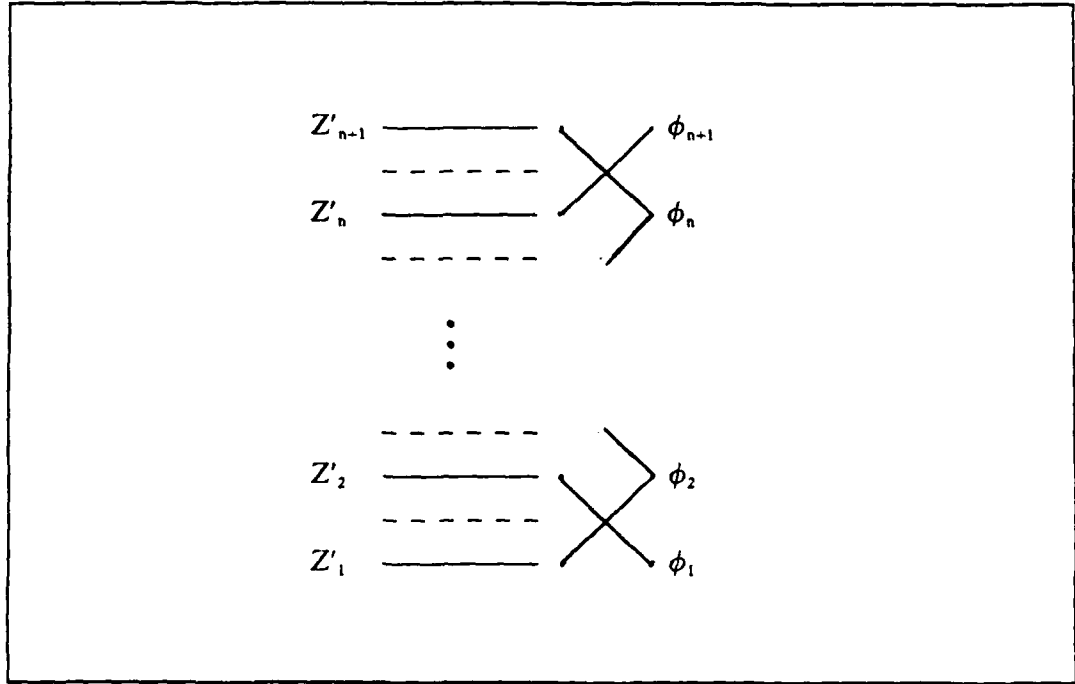


Fig. 3. Basis functions for grid C.

$$E_{ij}(\bar{x}) = \sum_{k=i-1}^{i+1} \bar{x}^k \int_{Z_0}^{Z_T} \frac{d\phi_k}{dZ} \phi_j(Z) \phi_i(Z) dZ \quad \text{for } |i-j| \leq 1, \quad (2.68)$$

where \bar{x} is \bar{u} or \bar{T} .

Note that this is the same as equation (2.49) which is only defined for $\bar{x} = \bar{u}$ and is an $(n+2) \times (n+2)$ matrix. It has been given a new name because it combines equations (2.48) and (2.49) and is now an $(n+1) \times (n+1)$ matrix. The matrices M , K and E are evaluated using the same procedures as models FEM-A and FEM-B except only the formulas for $\phi_i(\xi)$ are needed from Appendix C.

The vorticity and divergence equations, written in matrix and vector form, are given in equations (2.50) through (2.53) as defined for model FEM-A. The thermodynamic matrix equations are

$$M \frac{dT_1}{dt} = -\mu K(\bar{u}) T_2 + \frac{f}{R} E(\bar{u}) V_1 - E(\bar{T}) W_1 + M Q_1. \quad (2.69)$$

$$\tilde{\mathbf{M}} \frac{dT_2}{dt} = \mu \mathbf{K}(\bar{\mathbf{u}}) T_1 + \frac{f}{R} \mathbf{E}(\bar{\mathbf{u}}) V_2 - \mathbf{E}(\bar{\mathbf{T}}) W_2 + \mathbf{M} Q_2. \quad (2.70)$$

These forecast matrix equations are simplified as described for model FEM-A. The final form of the vorticity and divergence vector equations are the same as for model FEM-A, equations (2.56) through (2.59). The thermodynamic vector equations are

$$\begin{aligned} T_{1(n+1)} &= T_{1(n-1)} \\ &+ 2\Delta t \left(-\mu \mathbf{M}^{-1} \mathbf{K}(\bar{\mathbf{u}}) T_2 + \frac{f}{R} \mathbf{M}^{-1} \mathbf{E}(\bar{\mathbf{u}}) V_1 - \mathbf{M}^{-1} \mathbf{E}(\bar{\mathbf{T}}) W_1 + Q_1 \right)_{(n)} \text{ and} \end{aligned} \quad (2.71)$$

$$\begin{aligned} T_{2(n+1)} &= T_{2(n-1)} \\ &+ 2\Delta t \left(\mu \mathbf{M}^{-1} \mathbf{K}(\bar{\mathbf{u}}) T_1 + \frac{f}{R} \mathbf{M}^{-1} \mathbf{E}(\bar{\mathbf{u}}) V_2 - \mathbf{M}^{-1} \mathbf{E}(\bar{\mathbf{T}}) W_2 + Q_2 \right)_{(n)}. \end{aligned} \quad (2.72)$$

In this model, the vectors $A_1, A_2, D_1, D_2, H_1, H_2, Q_1, Q_2, T_1, T_2, U_1, U_2, V_1, V_2, W_1$ and W_2 contain $n+1$ components. The matrices \mathbf{M}, \mathbf{K} and \mathbf{E} are $(n+1) \times (n+1)$ matrices. The surface geopotential and the diagnostic variables are calculated using the corresponding equations in model FDM-C.

III. EXPERIMENTS AND RESULTS

Several experiments are performed for baroclinic instability with all or some of the models. The first results use the linear wind profile which was used by Shapiro (1987). Most of the experiments use a hyperbolic tangent vertical wind profile with three variations. The basic experiments use an initial v -field which is independent of Z with no temperature perturbation. These experiments are integrated for 96 hours to determine the exponential growth rate. The basic experiments use two-, four-, six- and sixty-layer models. The next to last experiment uses the finite difference method of calculating the thermodynamic variables in the finite element model for grid A. The last experiment uses an initial v -field which tilts backward (toward negative x) with height. The temperature is chosen to satisfy the thermal wind relation. These profiles are integrated out to 72 hours to investigate the enhanced initial growth due to the tilt (Farrell, 1985). The last two experiments use only the sixty-layer models except for the thermodynamic experiment which includes six-layer models. The analytical solution of each experiment does not exist except for the Eady (1949) solution for the linear shear solutions.

As in Jordan (1985) and Shapiro (1987), the sixty-layer model results are intercompared to determine if the models are converging to the same solution. The standard of comparison for the two-, four- and six-layer models is the consensus sixty-layer solution. The v -component and temperature profiles are examined in each experiment. Exponential growth rates are calculated to help compare the models.

Several parameters are defined identically in each experiment. The vertical coordinate, Z , is defined between zero and one (1000-368mb) and the vertical levels are equally spaced. The Coriolis parameter is defined at 45 degrees latitude. The mean state potential temperature increases with height from its surface value of 310.0 degrees Kelvin. The vertical shear in the u bar field is defined in each experiment as a function of Z multiplied by STRGTH, where STRGTH defines the strength of the wind at the top of the atmosphere in m/s. In all experiments, STRGTH is defined as 40 m/s. There is no diabatic heat source and no mountain topography. Unless otherwise indicated, all forecast experiments are terminated at 96 hours.

A. LINEAR VERTICAL SHEAR IN THE UBAR FIELD

The wind profile in these experiments is a linear function of Z , with $ubar = (STRGTH)Z$. Waves are generated in each model using an initial perturbation of $v' = 5.0$ m/s in the cosine term. Wavelengths (in x) of 4000, 3000 and 2000 km are used for each model for two, six and sixty levels.

1. Sixty-Layer Models

For an x -wavelength of 4000 km, the sixty-layer FEM-C and FDM-C models both converge to the same solution as the FDM-A and FDM-B models from Shapiro (1987) for the v -component amplitude and phase (Fig. 4) and the temperature amplitude (Fig. 5). All figures will be found at the end of the chapter. As in Shapiro (1987), the phase is defined between zero and 360 degrees and a discontinuity occurs in the phase profile if the phase passes through zero degrees. FDM-A, FDM-B, FDM-C and FEM-C represent the same physical solution, which is called the consensus solution. These solutions all have the same patterns which were derived by Eady (1949) for the quasi-geostrophic model. The v -field has a maximum amplitude on the boundaries and tilts backward with height. The FEM-B amplitudes in Fig. 4 and Fig. 5 are less than the consensus which indicates a smaller growth rate. The FEM-B temperature field (Fig. 5) also has an oscillation near the surface similar to what was found by Shapiro even though an additional element is added to the vertical velocity. The FEM-A scheme has a slightly larger growth rate than the consensus. This suggests that the FEM-A and FEM-B models need further improvement to take full advantage of their possibilities.

For an x -wavelength of 3000 km, the sixty-layer profiles for the v -component and temperature show the same results as the 4000 km case except that the magnitude of the amplitudes are smaller and the profiles appear to contain some oscillation (Fig. 6). The reduced amplitude agrees with the Eady (1949) theory which gives smaller growth rates for this wavelength.

At a smaller wavelength of 2000 km, the v -component and temperature amplitudes show very little growth at all but have several oscillations throughout the atmosphere (Figs. 7-8). The finite difference models and FEM-C converge to the same consensus solution. FEM-A is very close to the consensus profile, but has a slightly smaller amplitude in the middle layers of the temperature profile and a slightly larger amplitude in the v -component profile. FEM-B has a smaller amplitude than the consensus profile for the v -component and oscillates between having a smaller amplitude to having a larger amplitude in the temperature profile. The phase profiles show that all the models except FEM-A and FEM-B converge to the same phase solution (Fig. 7).

FEM-A is very close to the consensus solution but changes from being slightly greater in the lower layers to being slightly less in the upper layers. FEM-B is smaller than the consensus in the lower layers and larger in the upper layers. The lack of growth in this case agrees with the Eady theory which gives only neutral modes for this scale. Farrell (1985) has shown that a given initial state can funnel energy into the neutral modes of the problem. In this case, the most likely neutral waves which appear in the solutions are the two quasi-geostrophic solutions and internal gravity waves with small vertical scales.

2. Six-Layer Models

For the 4000 km wavelength, all the models except FEM-B and FEM-A converge to the consensus for the v-component amplitude (Fig. 9) and all the models except FEM-B are converging to the consensus solution for the temperature amplitude (Fig. 10). FEM-B has the same shape as the consensus profile but has a smaller amplitude for temperature and the v-component. FEM-A has a much smaller v-component than the consensus. The v-component phase profiles show that all the models except FEM-A and FEM-B converge to the consensus phase profile (Fig. 9). The six-layer FDM-B model is closest to the consensus.

At 3000 km, the difference among the six-layer models and between the six-layer models and the consensus profile for v-component and temperature amplitudes becomes more pronounced (Figs. 11-12). In general, the finite difference models are closer than the finite element models to the consensus profile for schemes B and C. The opposite is true for grid A except in the lower layers of the temperature amplitude profile. FEM-B has a much smaller amplitude than the consensus. The phase profiles show the models are still converging to the consensus phase profile except for FEM-B (Fig. 11).

At 2000 km, the models appear to be a little chaotic (Figs. 13-14). However, all the models depict the overall shape of the consensus profile except for the oscillations in the temperature amplitude profiles. FDM-B appears to represent the consensus better than the other models although FEM-B gives the same surface temperature prediction as the consensus profile. In the v-component amplitude profiles, the finite element models are closer than the finite difference models to the consensus profile for grids A and C but not B. However, the surface prediction for FDM-C is closer than the prediction for FEM-C. FDM-B is closest to the consensus profile for the v-component amplitude. The phase profiles show that the models for scheme A are closer to the consensus phase profile than are the models for schemes B and C (Fig. 13). Clearly, the small oscillations can not be reproduced in any six-layer scheme.

3. Two-Layer Models

The curves for the two-layer models are not shown to save space. For an x-wavelength of 4000 km, FDM-C represents the shape of the consensus profile of temperature and v-component better than the other models, but it has the benefit of an extra prediction level for these variables. FEM-C gives the best surface prediction for both the temperature and v-component. In the v-component amplitude profiles, the finite difference models are closer to the consensus amplitude than are the finite element models for schemes A and B. However, these two schemes do not have enough resolution to depict the shape of the consensus profile. The phase profiles for the v-component show general agreement among the models in representing the shape of the consensus.

At 3000 km, FDM-C again represents the shape of the consensus amplitude profile for temperature and v-component well. FEM-A is also close to the magnitude of the consensus profile. The other models give poorer results.

At 2000 km, the magnitude of FDM-C overshadows all the other models. FEM-C and FDM-A also show a tendency for growth. In the v-component phase profiles, all the A and B models have a negative tilt instead of the positive tilt of the consensus profile. FDM-C has a positive tilt in the lower atmosphere and FEM-C has a positive tilt in the upper atmosphere.

B. NONLINEAR VERTICAL SHEAR IN THE UBAR FIELD

The nonlinear vertical shear is created by using a hyperbolic tangent function of Z similar to the one used by Satyamurty *et al* (1982). In this experiment, $ubar = (STRGTH) \tanh(\alpha Z + \kappa)$ where α and κ are given different values to control the magnitude and location of the shear. Fig. 15 illustrates the three ubar profiles used in this experiment which are referred to as Type I, Type II and Type III. Waves are generated in each model using an initial perturbation of $v' = 5.0$ m/s in the cosine term. The x-wavelengths of 4000, 3000 and 2000 km are used for each model.

1. Hyperbolic Shear Type I

For this part of the experiment, $\alpha = 2.0$ and $\kappa = 0.0$. This increases the magnitude of the low level ubar shear and forces the largest gradient to occur near the surface.

a. Sixty-Layer Models

Table 1 contains the exponential growth rates for all the sixty-layer models. For an x-wavelength of 4000 km, the growth rates for Type I indicate that the sixty-layer

finite difference models and FEM-C all converge to the same growth rate after 96 hours. This is similar to the results from the linear wind profile.

Table 1 Exponential Growth Rates ($\times 10^{-5}$) Hyperbolic Shear						
60-layer Models						
	FDM-A	FDM-B	FDM-C	FEM-A	FEM-B	FEM-C
Type I						
4000 km	1.45	1.45	1.45	1.46	1.43	1.45
3000 km	1.53	1.53	1.53	1.54	1.48	1.53
2000 km	1.33	1.33	1.33	1.35	1.28	1.32
Type II						
4000 km	1.82	1.81	1.82	1.82	1.78	1.82
3000 km	2.14	2.14	2.14	2.14	2.09	2.14
2000 km	2.46	2.46	2.46	2.46	2.40	2.47
Type III						
4000 km	2.89	2.89	2.89	2.89	2.83	2.89
3000 km	3.21	3.22	3.22	3.21	3.14	3.22
2000 km	3.02	3.03	3.03	3.01	2.90	3.04

The growth rate for FEM-A is slightly larger and the growth rate for FEM-B is slightly smaller. FDM-A, FDM-B, FDM-C and FEM-C all converge to the same solution for the v-component and temperature amplitudes and represent the consensus solution. The FEM-A model has a slightly higher amplitude than the consensus profile and the shape is the same as the consensus profile. The FEM-B model has a lower temperature amplitude than the consensus profile, but the shape is the same except for an oscillation in the lower layers similar to the linear shear case. The difference between FEM-B and the consensus profile is greater in the lower layers than in the upper layers. For the v-component amplitude, the amplitude for FEM-B is again lower than the consensus profile, but there is no oscillation in the lower layers of the atmosphere. The profiles for the v-component phase are the same for all six models. The profiles are not shown because the consensus profile is included with the lower resolution curves.

For an x-wavelength of 3000 km, the growth rates show the same the results as 4000 km except the growth rates are greater. The v-component and temperature profiles also show the same results as 4000 km. Again, the amplitudes are larger for the smaller wavelength. The v-component phase profiles show that FDM-A, FDM-B, FDM-C and FEM-C are identical, but FEM-A and FEM-B have a slightly larger phase.

For an x-wavelength of 2000 km, the growth rates show the same results as 4000 km except the growth rates are smaller. The v-component and temperature profiles also show the same results as 4000 km, but the amplitudes are smaller. The amplitude profiles also appear to contain some oscillation. The v-component phase profiles are identical for all the models except FEM-A which has a slightly larger phase. This profile clearly has the instability shifted to smaller wavelengths than the linear profile due to the vertical wind shear being larger near the surface.

b. Six-layer Models

The profiles for the six- and two-layer models are not shown to save space. Table 2 contains the exponential growth rates for six-, four- and two-layer models for Type I. For an x-wavelength of 4000 km, the growth rates show that all the models except FEM-B are converging to the growth rate of the consensus profile. The v-component amplitude profiles support the convergence of the models to the consensus profile. The finite difference models are closer to the consensus solution than are the finite element models for grids A and B, but FEM-C is closer than FDM-C. All models represent the low level shear well. Although the growth rates show that both FDM-A and FEM-C are closest to the consensus, the amplitude profiles show that FEM-C is closest to the consensus profile. The temperature amplitude also shows the convergence of the models to the consensus solution except for FEM-B. In this case, the surface prediction for both FEM-B and FDM-B is considerably less than the consensus. The v-component phase profiles show a moderate amount of negative tilt in the lower half of the atmosphere corresponding to the low level shear region. All the models have the same phase profile shape, but scheme C is closer to the consensus solution than are schemes A and B. This difference is due to a difference in phase speed between the schemes.

Table 2
Exponential Growth Rates ($\times 10^{-5}$)
Hyperbolic Shear Type I

Models							
	Consensus	FDM-A	FDM-B	FDM-C	FEM-A	FEM-B	FEM-C
6 Layers							
4000 km	1.45	1.44	1.42	1.49	1.43	1.36	1.46
3000 km	1.53	1.52	1.48	1.54	1.49	1.41	1.55
2000 km	1.33	1.37	1.41	1.46	1.37	1.52	1.54
4 Layers							
4000 km	1.45	1.35	1.36	1.58	1.32	1.33	1.51
3000 km	1.53	1.40	1.48	1.66	1.31	1.46	1.64
2000 km	1.33	1.50	1.48	-0.20*	1.15	1.55	1.43
2 Layers							
4000 km	1.45	1.29	1.03	1.49	1.09	1.07	1.36
3000 km	1.53	1.51	1.00	1.83	1.13	0.98	1.51
2000 km	1.33	1.75	0.24*	2.66	1.10	-0.87*	2.07
* These cases do not converge to a steady growth rate							

The growth rates for an x-wavelength of 3000 km give results similar to those for 4000 km except that FDM-C is closer than FEM-C to the consensus solution. The v-component amplitude and phase profiles are also similar. In this case, however, FDM-A is closest to the consensus amplitude profile instead of FEM-C, but FEM-B is still farthest from the consensus. The phase results are identical to the results for the 4000 km wavelength case.

At an x-wavelength of 2000 km, a few more changes are observed from the longer wavelengths. For this wavelength, the growth rates indicate that all the six-layer models are growing faster than the consensus solution. Although the growth rates for FDM-A and FEM-A are the same, the difference between the finite difference and finite element models for grids B and C is much greater at the smaller wavelength. These differences are also observed in the v-component and temperature amplitude profiles. Although the growth rates for FDM-A and FEM-A are the same, the amplitude profiles show that FEM-A is slightly closer to the v-component consensus solution, but FDM-A

is slightly closer to the temperature amplitude consensus. This may occur because the growth rate is computed at the first layer above $Z = 0$ and the differences between FDM-A and FEM-A occur above this level.

c. Four-Layer Models

In the 4000 km wavelength case, the growth rates show that the four-layer models do not converge to the consensus solution as well as the six-layer 4000 km models. Otherwise, the results are basically the same. The finite difference models are closer than the finite element models for grids A and B, but not grid C. However, the v-component amplitude profiles indicate that FEM-C is closest only at the second layer, where the growth rate is computed, and the top layer (Fig. 16). The amplitude profiles also show the lesser convergence of the four-layer models to the consensus solution. The v-component phase profiles give the same results as the six-layer models, but with a slightly greater difference between the four-layer models and the consensus.

For the 3000 km wavelength, the growth rates for the four-layer models again indicate results similar to the six-layer models. The finite difference models are closer to the consensus solution than are the finite element models, but FDM-B is closest to the consensus growth rate instead of FDM-A. FEM-A has the worst growth rate in this case. Also, the four-layer models do not converge to the consensus solution as well as do the six-layer models (Fig. 17). The v-component amplitude profiles support the growth rate results. The phase results for the four-layer models are similar to the results for the six-layer models. The primary difference is that except for FEM-C the four-layer model phase profiles are not as close to the consensus phase profile as are the six-layer models.

For the 2000 km wavelength, the growth rates indicate much less convergence of the four-layer models to the consensus solution. In fact, FDM-C fails to converge to a steady growth rate altogether. For this case, the finite element model growth rates are closer than the finite difference model rates to the consensus solution for schemes A and C, but not scheme B. All the models except FEM-A and FDM-C grow much faster than the consensus. FEM-C is closest to the consensus growth rate. FEM-C also reflects the shape of the v-component amplitude consensus profile better than the other four-layer models (Fig. 18). All the models except FDM-C depict the same shape as the phase consensus and FEM-C is again closest to the consensus solution. Note that the shorter waves also have smaller vertical scales.

d. Two-Layer Models

For the 4000 km wavelength, the growth rates indicate that the two-layer finite difference models are closer to the consensus solution than are the finite element models for grids A and C, but not grid B. FEM-C is closest to the consensus amplitude profile for v-component and temperature. Schemes A and B do not have enough resolution to depict the low level shear in the v-component amplitude profile. The grid C models attempt to reflect the low level shear, but the surface predictions are considerably less than the consensus solution. All six models reflect the negative tilt of the consensus phase profile even though they have only two levels. FEM-C is closest to the consensus phase profile.

The growth rates for the 3000 km case indicate that the finite difference models are closer than the finite element models to the consensus growth rate for grids A and B, but FEM-C is closer than FDM-C. The scheme B models and FEM-A have much lower growth rates than the consensus and FDM-C has a larger growth rate. FEM-C is closest to the consensus amplitude profile for the v-component, but FDM-A is closest in the middle and lower levels of the temperature profile. Although grid B also predicts the temperature at the surface, its prediction is much poorer than the consensus solution. The two-layer A and B models do not have enough resolution to depict the shape of consensus v-component phase profile but they still reflect the negative tilt.

For the 2000 km wavelength, the growth rates for FDM-A, FDM-C and FEM-C are much greater than the consensus growth rate, and FEM-A is slightly less than and closest to the consensus. FDM-B and FEM-B grow very little and their growth rates do not converge to a steady growth rate. The finite element models are closer than the finite difference models to the consensus v-component and temperature amplitude profiles for schemes A and C, but not for scheme B. FEM-A is closest in magnitude to the consensus solution.

2. Hyperbolic Shear Type II

For this part of the experiment, $\alpha = 4.0$ and $\kappa = 0.0$. This increases the magnitude of the low level shear but keeps the largest gradient near the surface.

a. Sixty-Layer Models

For an x-wavelength of 4000 km, the growth rates for Type II indicate that the sixty-layer A and C models all converge to the same growth rate after 96 hours (Table 1). The growth rate for FDM-B is nearly the same but slightly smaller and the growth rate for FEM-B is the smallest. FDM-A, FDM-C, FEM-A and FEM-C all converge to the same solution for the v-component and temperature amplitudes and

represent the consensus solution. The FDM-B model has a slightly smaller amplitude than the consensus profile, but the shape is the same as the consensus profile. The FEM-B model has a lower temperature amplitude than the consensus profile and the shape is the same except for a similar oscillation to that of the linear shear case in the lower layers. The difference between FEM-B and the consensus profile is greater in the lower layers than in the upper layers. For the v-component amplitude, the amplitude for FEM-B is again lower than the consensus profile, but there is no oscillation in the lower layers of the atmosphere. The magnitudes of the growth rates and the amplitude profiles are greater than for the Type I case. The profiles for the v-component phase are the same for all six models. The sixty-layer profiles are not shown because the consensus profile is included with the lower resolution curves.

For an x-wavelength of 3000 km, the growth rates for all the sixty-layer models are identical except for FEM-B and are greater than the 4000 km growth rates. The v-component and temperature profiles show results similar to the 4000 km case, but with larger amplitudes. The v-component phase profiles show that all the models have identical phases at 96 hours except for FEM-A which has a slightly larger phase.

For an x-wavelength of 2000 km, the results are the same as for the 3000 km case except FEM-C has a slightly larger growth rate. However, the v-component and temperature profiles show the same results as for 4000 km except the amplitudes are larger for 2000 km. The v-component phase profiles are identical for all the models except FEM-A which has a slightly larger phase.

b. Six-Layer Models

To save space, the profiles for the six- and two-layer models are not shown. Table 3 contains the exponential growth rates for six-, four- and two-layer models for Type II. For an x-wavelength of 4000 km, the growth rates indicate that the finite element models are closer to the consensus growth rate than are the finite difference models for grids B and C, but not for grid A. The growth rates for grid C are closer than the rates for grids A and B to the consensus. FEM-C is closest to the consensus growth rate. All the models represent the shape of the consensus profile well except for the grid B temperature prediction. FEM-C is closest to the consensus amplitude profile. The v-component phase profiles show the negative tilt in the lower half of the atmosphere corresponding to the region of low level shear. All the six-layer models have the same shape as the consensus phase profile, but scheme C is closer to the consensus than are schemes A and B.

<p>Table 3 Exponential Growth Rates ($\times 10^{-5}$) Hyperbolic Shear Type II</p>							
Models							
	Consensus	FDM-A	FDM-B	FDM-C	FEM-A	FEM-B	FEM-C
6 Layers							
4000 km	1.82	1.68	1.63	1.93	1.66	1.67	1.87
3000 km	2.14	1.95	1.95	2.26	1.89	1.99	2.23
2000 km	2.46	2.29	2.43	2.14	2.05	2.45	2.54
4 Layers							
4000 km	1.82	1.63	1.36	1.82	1.51	1.35	1.78
3000 km	2.14	1.97	1.61	1.89	1.70	1.59	2.05
2000 km	2.46	2.48	1.82	2.47	1.98	1.84	2.25
2 Layers							
4000 km	1.82	1.16	0.57	1.80	1.17	0.49	1.58
3000 km	2.14	1.38	1.42	2.32	1.23	0.56*	1.90
2000 km	2.46	1.72	0.25*	3.16	1.30	-0.34*	2.57
* These cases do not converge to a steady growth rate							

For the 3000 km wavelength case, the growth rates indicate results similar to the 4000 km case. For grids A and C, the finite difference models are closer to the consensus profile than are the finite element models although the differences are greater in the low level shear region than in the upper levels. FEM-B is closer than FDM-B to the consensus amplitude profile except at the midpoint of the temperature profile. FDM-C is closest to the consensus profile except in the lowest levels of the temperature profile above the surface where FEM-B is closest. The phase profiles show the same results as the 4000 km case. For the 2000 km wavelength case, all the results are the same as the results for 4000 km.

c. *Four-Layer Models*

The growth rates for the four-layer 4000 km wavelength models indicate the finite difference models are closer than the finite element models to the consensus growth rate. Schemes A and B have much smaller growth rates than both scheme C and the

consensus solution. FDM-C has the same growth rate as the consensus. Overall, the v-component and temperature amplitude profiles show that the finite difference models are closer to the consensus profile than are the finite element models (Figs. 19-20). However, for scheme B the finite element model is closer to the consensus amplitude profile for the temperature. For scheme C, the finite element model is closer to the consensus at the surface and at $Z = 0.25$ for the v-component profile. Otherwise, FDM-C is closest to the consensus profile. The v-component phase profiles show the negative tilt in the lower half of the atmosphere corresponding to the region of low level shear (Fig. 19). All the six-layer models have the same shape as the consensus phase profile, but scheme C is closer to the consensus than are schemes A and B.

For the 3000 km wavelength, the growth rates for the four-layer models indicate results similar to the 4000 km case, except that FEM-C is closer than FDM-C to the consensus solution. FEM-C is also closest to the growth rate for the consensus. Overall, the finite difference models are closer than the finite element models to the consensus amplitude profile for schemes A and B, but not for scheme C in the v-component profiles (Fig. 21). The finite element models are closer than the finite difference models for grids B and C, but not grid A for the temperature profile (Fig. 22). FEM-C is closest to the consensus except in the middle layers of the temperature profile where FDM-A is closest. For the phase profiles, the results for this case are the same as the results for the 4000 and 3000 km cases (Fig. 21).

Growth rates for the four-layer models in the 2000 km case indicate that the finite difference models are closer than the finite element models to the consensus solution for grids A and C. FDM-B and FEM-B are nearly identical. FDM-C is closest to the growth rate for the consensus solution. In this case, the finite element models are closer than the finite difference models to the consensus amplitude profile for scheme B in the lower half of the atmosphere and for scheme C, but not for scheme A except in the upper levels of the v-component amplitude profile (Fig. 23). FEM-C is closest to the consensus profile.

d. Two-Layer Models

For the 4000 km wavelength, the growth rates indicate that the two-layer finite difference models are closer to the consensus solution than are the finite element models for grids B and C, but not for grid A. FEM-C is slightly closer than FDM-A to the consensus. FDM-C is closest to the growth rate for the consensus solution, but FEM-C is closest overall to the consensus amplitude profile for v-component and temperature. Schemes A and B do not have enough resolution to depict the low level shear

in the v-component amplitude profile. The grid C models attempt to reflect the low level shear, but the surface predictions are considerably less than the consensus solution. All six models reflect the negative tilt of the v-component even though they have only two levels and FEM-C is closest to the consensus phase profile.

For the 3000 km case, the growth rates show that the finite difference models are closer than the finite element models to the consensus for schemes A and C, but not for scheme B. FEM-B appears to be closer than FDM-B to the consensus growth rate, but FEM-B does not converge to a steady growth rate. The growth rate for FDM-C is closest to the consensus. The amplitude profiles for scheme C are also closest to the consensus amplitude profile for the v-component and temperature, and schemes A and B have much smaller magnitudes than the consensus. The finite difference models are closer than the finite element models to the consensus for schemes A and C except for FEM-C at the top layer. FEM-B is closer than FDM-B. For the v-component phase, all of the models depict the negative tilt of the consensus profile.

At 2000 km, the growth rates for grid C are greater than the consensus, and the growth rates for grids A and B are much less than the consensus growth rate. The growth rates for grid B do not converge to a steady growth rate. The growth rate for FEM-C is closest to the consensus. The finite element models are closer to the consensus amplitude profile for temperature and v-component than are the finite difference models for grids B and C, but not for grid A. Scheme C has a greater magnitude than the consensus, especially FDM-C. FDM-A is closest to the consensus in magnitude but does not have enough resolution to depict the low level shear.

3. Hyperbolic Shear Type III

For this part of the experiment, $\alpha = 4.0$ and $\kappa = 1.0$. This causes the strongest shear to occur at about $Z = 0.25$ instead of at the surface, and provides a variety of responses that are less sensitive to the lower boundary conditions.

a. Sixty-Layer Models

At the 4000 km wavelength, all the growth rates are identical except for FEM-B which has a smaller growth rate (Table I). All of the sixty-layer models except FDM-B and FEM-B converge to the same solution for the v-component and temperature amplitude profiles. FDM-B is identical to the consensus profiles except at the surface of the temperature profile. FEM-B shows the same results as the Type II case, but the temperature oscillations are smaller (Fig. 24). The magnitudes of the growth rates and the amplitude profiles are larger than those for Type I and Type II. The phase

profiles of all the models converge to the same solution except FEM-B which has a slightly larger phase.

For 3000 km, FDM-B, FDM-C and FEM-C have identical growth rates. FDM-A and FEM-A also have identical but slightly smaller growth rates and FEM-B has the smallest growth rate. The v-component and temperature amplitude profiles show small differences between the models, especially near the strongest shear region at $Z = 0.25$ (Figs. 25-26). For the v-component amplitude profiles, the finite difference models converge to the same solution and represent the consensus solution. FEM-A has a slightly smaller amplitude and FEM-C has a slightly larger amplitude in the shear zone. In the temperature profiles, the differences are slightly larger for FEM-A and FEM-C. The results for FEM-B are the same as the previous cases, but again the oscillations are smaller. For the v-component phase profiles, all the models converge to the same phase except FEM-A and FEM-B which are slightly larger (Fig. 25).

At the 2000 km wavelength, the growth rates show a little more variation than in the other cases. FDM-B and FDM-C are identical and represent the consensus growth rate. Although very close to the consensus, the growth rate for FDM-A is slightly smaller and FEM-C is a little larger. FEM-A has a slightly smaller growth rate than FEM-A and FEM-B has the smallest growth rate. The v-component and temperature amplitudes also show more variations among the models in the region of the strongest shear than in previous sixty-layer cases (Figs 27-28). FDM-B and FDM-C are identical and represent the consensus profile. FDM-A is very close to the consensus, but slightly smaller in magnitude. FEM-A has a smaller magnitude than the consensus and FDM-A. FEM-C has a larger magnitude than the consensus. FEM-B has a much smaller magnitude than the consensus. The differences among the models are slightly greater for the temperature profiles than the v-component profiles. However, for the phase profiles, the finite difference models and FEM-C converge to the same phase. FEM-A is slightly greater and FEM-B is slightly smaller (Fig. 27).

b. Six-Layer Models

To save space, the profiles for the six- and two-layer models are not shown. Table 4 contains the exponential growth rates the six-, four- and two-layer models for Type III. For a wavelength of 4000 km, the growth rates for the finite element models are closer to the consensus than are the growth rates for the finite difference models for schemes A and C, but not B. FDM-B is closest to the consensus growth rate. Overall, the finite element models are closer than the finite difference models to the consensus amplitude profile for v-component and temperature for grids A and C. For grid B, the

finite difference model is closer to the consensus than the finite element model except at the lowest level above the surface. In general, grid B is closest to the consensus amplitude profile. For the phase profiles, all of the models are close to the consensus profile, but grid B is closest.

Table 4
Exponential Growth Rates ($\times 10^{-5}$)
Hyperbolic Shear Type III

Models							
	Consensus	FDM-A	FDM-B	FDM-C	FEM-A	FEM-B	FEM-C
6 Layers							
4000 km	2.89	2.56	2.80	2.60	2.71	2.78	2.71
3000 km	3.22	2.70	2.96	2.55	2.99	3.02	2.89
2000 km	3.03	2.08	2.38	0.98**	2.98	2.91	1.31**
4 Layers							
4000 km	2.89	2.26	2.93	2.48	2.48	2.93	2.48
3000 km	3.22	1.81	3.40	2.44	2.49	3.45	2.68
2000 km	3.03	1.65	3.76	1.95	1.54	3.95	1.77
2 Layers							
4000 km	2.89	2.23	2.13	2.53	1.61	2.37	2.24
3000 km	3.22	2.55	2.13	3.23	1.63	2.44	2.76
2000 km	3.03	2.68	1.02*	4.20	1.41	0.27*	3.59
* These cases do not converge to a steady growth rate							
** These models are still converging to a steady growth rate							

For the 3000 km case, the growth rates indicate that all the models are at least 8 percent less than the consensus growth rate. The finite element models are closer than the finite difference models to the consensus and FEM-B is closest. Overall, the finite element models are closer than the finite difference models to the consensus amplitude profile for v-component and temperature. The only exceptions are at the top layer of the v-component amplitude profiles and at the midpoint of the temperature profiles where FDM-B is closer. In general, FEM-B is closest to the consensus. For the phase profiles, the A and B profiles are closer than the C profiles to the consensus, and FDM-A is closest to consensus phase profile for the v-component.

For a wavelength of 2000 km, the growth rates for the finite element models are closer than the growth rates for the finite difference models to the consensus growth rate with FEM-A being closest. The growth rates for the finite difference models and FEM-C are much less than the growth rate for the consensus. The growth rates for the C models are still converging at 96 hours, but even after 192 hours the growth rates increase only slightly. The amplitude profiles for the v-component and temperature also show that the finite element models are closer than the finite difference models to the consensus. FEM-A is closest to the consensus amplitude profile. For the phase profiles, the scheme A models are closer to the consensus phase profile than are the scheme B and C models.

c. Four-Layer Models

At an x-wavelength of 4000 km, the growth rates for FDM-B and FEM-B are the same and closest to the consensus growth rate. For schemes A and C the growth rates for the finite element models are closer to the consensus than are the growth rates for the finite difference models. The growth rates for schemes A and C are much less than the consensus. The finite element models are closer than the finite difference models to the consensus amplitude profile for grids A and C (Fig. 29). For grid B, FDM-B is closer than FEM-B and is the closest overall to the consensus profile. For the phase profiles, all the models follow the shape of the consensus profile well (Fig. 29). FEM-C is closest to the consensus phase profile.

For 3000 km, the growth rates for the finite element models are closer than the finite difference models to the consensus for schemes A and C, but not B. FDM-B is closest to the consensus and schemes A and C are much less than the consensus. For grids A and C, the finite element models are closer than the finite difference models to the consensus amplitude profile for the v-component and temperature (Figs. 30-31). For grid B, FDM-B is closer than FEM-B to the consensus profile except in the upper layers of the v-component profile. Otherwise, FDM-B is closest to the consensus profile for this case. For the phase profiles, FEM-C is closest to consensus phase profile (Fig. 30).

For 2000 km, the growth rates show that none of the four-layer model growth rates are close to the consensus. The growth rates for the finite difference models are closer than the finite element models to the consensus growth rate. The growth rates for the grid B models are much greater than the consensus and the growth rates for the grid A and C models are much less. The growth rate for FDM-B is closest to the consensus growth rate. The amplitude profiles for the v-component and temperature show the same results as the growth rates (Figs. 32-33). The phase profiles show that all the

models except FDM-C have the same shape as the consensus profile and that scheme C is closest to the consensus (Fig. 32).

d. Two-Layer Models

For the 4000 km wavelength, the growth rates indicate that none of the models grow as rapidly as the consensus model for this case. For grids A and C, the growth rates for the finite difference models are closer than the rates for the finite element models to the consensus growth rate. FEM-B is closer to the consensus than FDM-B, and FDM-C is closest to the consensus. The finite element profiles are closer than the finite difference profiles to the consensus for scheme B and equal to or slightly closer to the consensus for scheme C. FDM-A is closer than FEM-A. FEM-B is closest to the consensus in this case except at the surface for the temperature profile where FEM-C is better. However, all the surface predictions are considerably less than the consensus prediction. For the phase profiles, all six models reflect the negative tilt of the v-component even though they have only two levels. FEM-C is closest to the consensus phase profile.

For the 3000 km case, the growth rates indicate the same results as the 4000 km case. The amplitude profiles show that except for grid B, the finite difference models are closer than the finite element models to the v-component and temperature amplitude consensus profile. FDM-C is closest to the consensus profile. For the phase profiles, all the models follow the shape of the consensus phase profile except FDM-C. FEM-A is closest to the consensus phase profile for this case.

At the 2000 km x-wavelength, the growth rates indicate that the grid C models have a much greater growth rate than the consensus model and that FEM-A and the grid B models have a much smaller growth rate. FDM-A also has a smaller growth rate than the consensus, but it is closer to the consensus than are the other models. Overall, the finite element models are closer than the finite difference models to the consensus amplitude profile for grids B and C, but not grid A. FDM-A is closest to the consensus profile in magnitude, but does not have enough resolution to depict the low level shear. For the v-component phase profiles, the models have a negative tilt similar to the consensus profile, but do not have enough resolution to depict the shape of the consensus profile. FDM-C is closest to the consensus phase profile.

C. USING FINITE DIFFERENCE METHOD IN FINITE ELEMENT MODEL

In this experiment, the finite difference equations and coefficients for the thermodynamic predictive equations are used in the finite element model for scheme A

instead of the matrix equations. The model is run with linear vertical shear in the ubar field for sixty-layer models and with hyperbolic Type III vertical shear in the ubar field for six- and sixty-layer models. Waves are generated in the model using an initial perturbation of $v' = 5.0$ m/s in the cosine term. Horizontal wavelengths of 4000 and 2000 km are used. The results are compared with the unmodified FDM-A and FEM-A profiles.

1. Linear Vertical Shear in the ubar Field

For both 4000 and 2000 km wavelengths, the temperature and v-component amplitude profile of the modified FEM-A model is identical to the unmodified FEM-A model (Figs.34-37). The phase profiles show the same results.

2. Hyperbolic Type III Shear in the ubar Field

a. Sixty-Layer Model

When the x-wavelength is 4000 km, the v-component amplitude shows that the modified sixty-layer FEM-C model has a greater amplitude than the unmodified models throughout the entire atmosphere (Fig. 38). The temperature amplitude of the modified FEM-C model is greater than the amplitudes of the unmodified models in the region of greatest vertical shear in the ubar field (Fig. 39). The phase profiles show that the phase for the modified model is identical to the unmodified FEM-A model (Fig. 38-39). For the 2000 km wavelength, the results are the same, but the difference between the amplitudes for the modified and unmodified models is greater (Fig. 40).

b. Six-Layer Model

For the 4000 km wavelength, the temperature and v-component amplitudes of the modified FEM-A model are nearly the same as the profiles for FDM-A (Figs. 41-42). The phase profiles show the modified FEM-C model is closer to the unmodified FEM-C model except in the middle layers of the temperature phase profile (Figs. 41-42).

When the x-wavelength is 2000 km, the temperature and v-component amplitude profiles show that the modified model lies between FDM-A and the unmodified FEM-C but is slightly closer to the finite difference model (Figs. 43-44). The phase profile of the modified FEM-C is closer to the unmodified FEM-C than to the finite difference model.

D. BACKWARD TILTING INITIAL VALUES

For this experiment, the initial phase in equation (2.41) is set to give a negative tilt by letting $\delta = bZ$ for the vorticity and temperature initial conditions. The experiment is run for the sixty-layer FDM-C model with linear ubar shear and with hyperbolic Type

III ubar shear. Each case is run with $b = \pi$ and $b = 4\pi$ which are called phase I and phase II respectively. The x-wavelengths of 4000, 3000 and 2000 km are used in each case.

1. Linear Vertical Shear in the ubar Field

a. X-wavelength of 4000 km

The growth rates for this case do not converge to a steady growth rate although they appear to be converging for the 3000 and 4000 km wavelengths for phase I (Table 5). The phase profile for phase I shows a negative tilt of about 110 degrees at 12 hours which becomes less negative by 72 hours (Fig. 45). For phase II, the phase profile has a much stronger negative tilt at 12 hours which also becomes more vertical with time.

Table 5 Exponential Growth Rates ($\times 10^{-5}$) Linear Shear (Negative Initial Phase) Sixty-layer FDM-C Model			
X-wavelength (km)			
	4000	3000	2000
Phase I			
12 hours	2.51	2.81	2.85
24 hours	1.50	1.60	0.91
36 hours	1.48	1.34	-0.37
48 hours	1.29	1.00	-0.23
60 hours	1.24	0.92	0.76
72 hours	1.21	0.87	-0.43
Phase II			
12 hours	1.07	1.35	1.88
24 hours	0.89	1.82	3.49
36 hours	2.28	3.20	2.62
48 hours	2.58	2.37	0.87
60 hours	2.03	1.64	-0.59
72 hours	1.64	1.21	0.01

b. X-wavelength of 3000 km

The growth rates show the same general results as the 4000 km results except the growth rates are smaller for phase I and slightly greater until 36 hours for phase II. The phase profiles give the same results as the 4000 km case (Fig. 46).

c. X-wavelength of 2000km

In this case, the growth rates show no apparent convergence to a steady growth rate. The amplitude profiles show there is growth for about 24 hours and then the profile oscillates back and forth without growing (Fig. 47). This is expected because the Eady solution is not unstable for this wavelength. Phase II has the same pattern except it increases in magnitude for 48 hours before decreasing slightly. For the phase profiles, phase I has a slightly negative tilt at 12 hours which becomes positive by 72 hours (Fig. 48). Phase II has a greater negative tilt than phase I at 12 hours, but it is less than the tilt for the 4000 and 3000 km cases. The tilt for phase II becomes positive by 48 hours and then becomes negative again at 72 hours.

2. Hyperbolic Type III Shear in the ubar Field

a. X-wavelength of 4000 km

The growth rates for the first 12 hours are much greater than the growth rates for the linear case, but converge quickly to a steady growth rate for phase I (Table 6). For phase II, the early growth rates are larger and converge slower than the rates for phase I. However, the growth rates for both phase I and phase II converge to the same value. The phase profiles show less negative tilt than the linear case (Fig. 49). Phase II has a larger negative tilt than phase I at 12 hours in the region of the strongest vertical shear in the ubar field ($Z = 0.25$). This negative tilt becomes less negative with time but the change is less pronounced than in the linear case.

b. X-wavelength of 3000 km

In this case, the results are similar to the results for 4000 km. The growth rates are greater than at 4000 km. The phase results are also the same as the 4000 km case except for less negative tilt at 12 hours (Fig. 50).

Table 6
Exponential Growth Rates ($\times 10^{-5}$)
Hyperbolic Shear Type III (Negative Initial Phase)
Sixty-layer FDM-C Model

X-wavelength (km)			
	4000	3000	2000
Phase I			
12 hours	4.33	4.50	3.93
24 hours	2.89	3.25	3.20
36 hours	2.84	3.23	3.06
48 hours	2.88	3.21	3.03
60 hours	2.89	3.21	3.04
72 hours	2.89	3.21	3.03
Phase II			
12 hours	4.44	5.46	6.37
24 hours	4.24	4.30	3.47
36 hours	3.12	3.29	3.06
48 hours	2.90	3.22	3.04
60 hours	2.88	3.21	3.04
72 hours	2.89	3.21	3.03

c. X-wavelength of 2000 km

At 2000 km, the same trend is still evident although the growth rates decrease slightly from the 3000 km case after 12 hours. The growth rates do not oscillate as they did in the linear case. The phase profiles show the negative tilt at 12 hours is less than the previous cases (Fig. 51).

The results of this experiment agree with the findings of Farrell (1985) that large initial growth rates can occur in the early time steps and converge to the most unstable growth. In the future, this type of time evolution should be used to test the various schemes for various wavelengths.

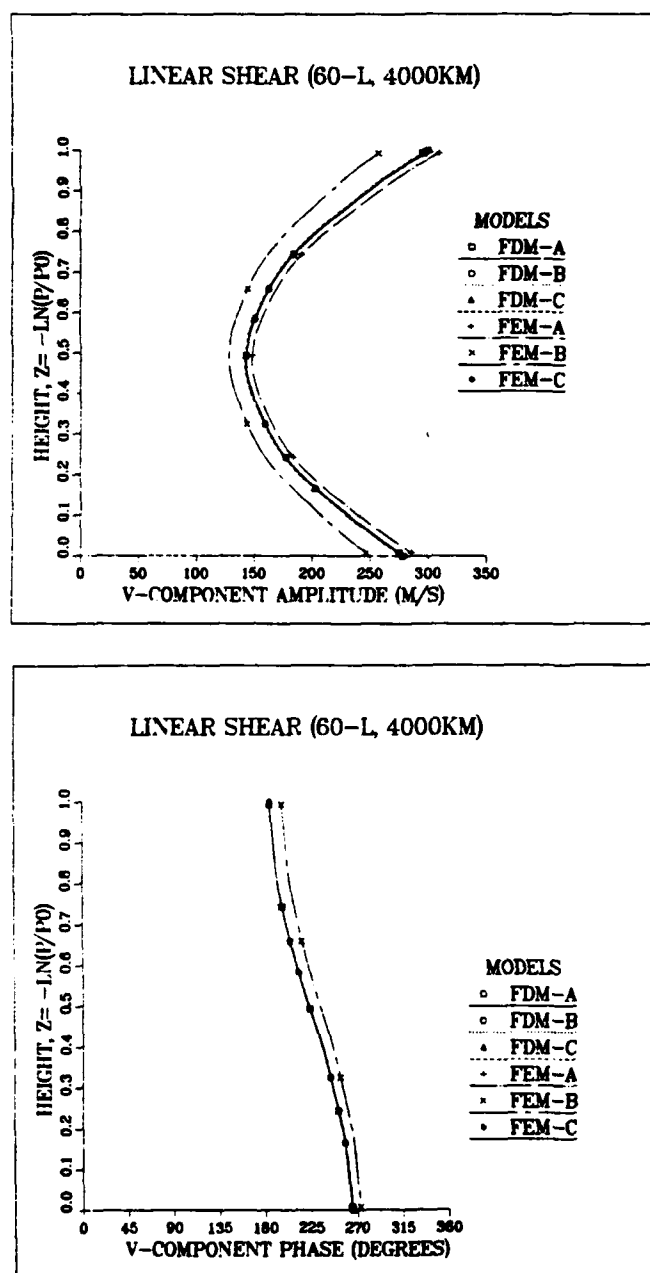


Fig. 4. 60-layer, 4000 km linear shear experiment at 96 h comparing v-component amplitudes (top) and phases (bottom).

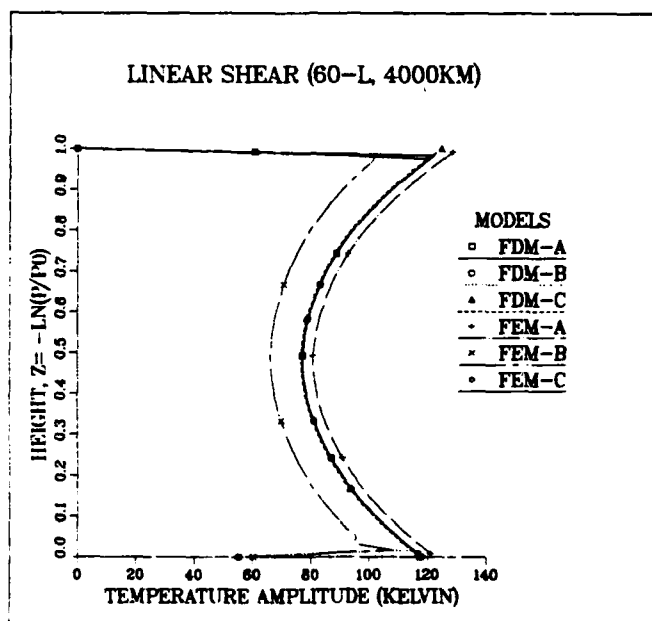


Fig. 5. 60-layer, 4000 km linear shear experiment at 96 h comparing temperature amplitudes.

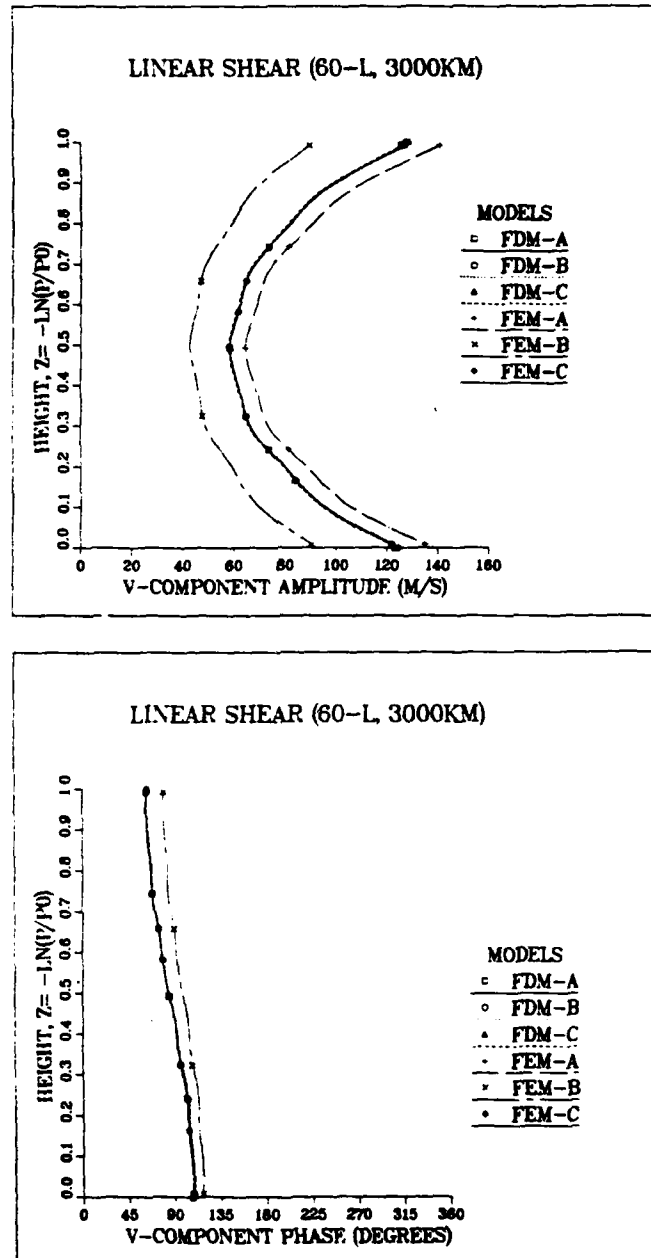


Fig. 6. 60-layer, 3000 km linear shear experiment at 96 h comparing v-component (top) and temperature (bottom) amplitudes.

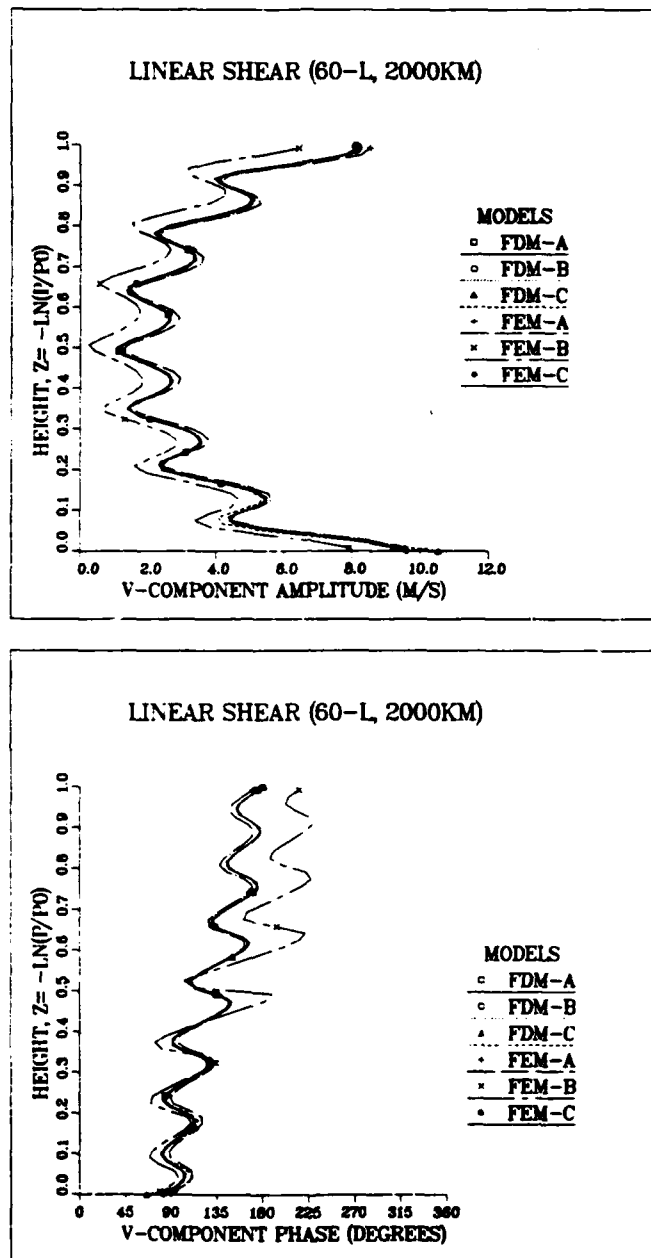


Fig. 7. 60-layer, 2000 km linear shear experiment at 96 h comparing v-component amplitudes (top) and phases (bottom).

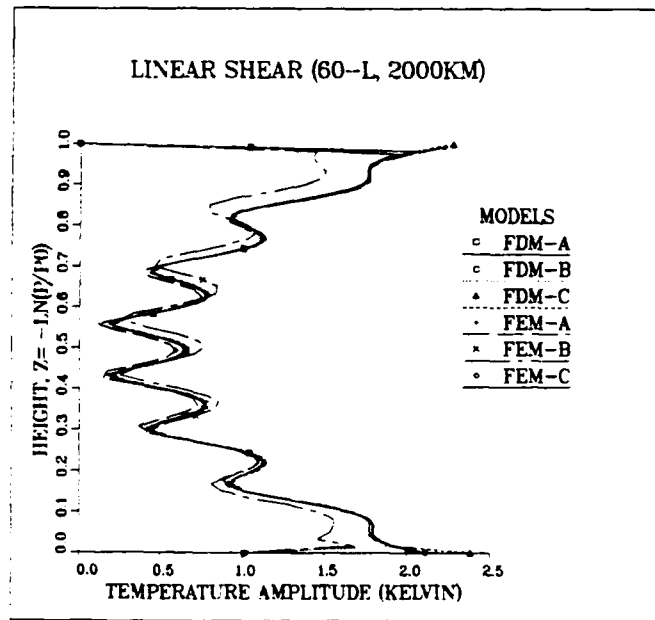


Fig. 8. 60-layer, 2000 km linear shear experiment at 96 h comparing temperature amplitudes.

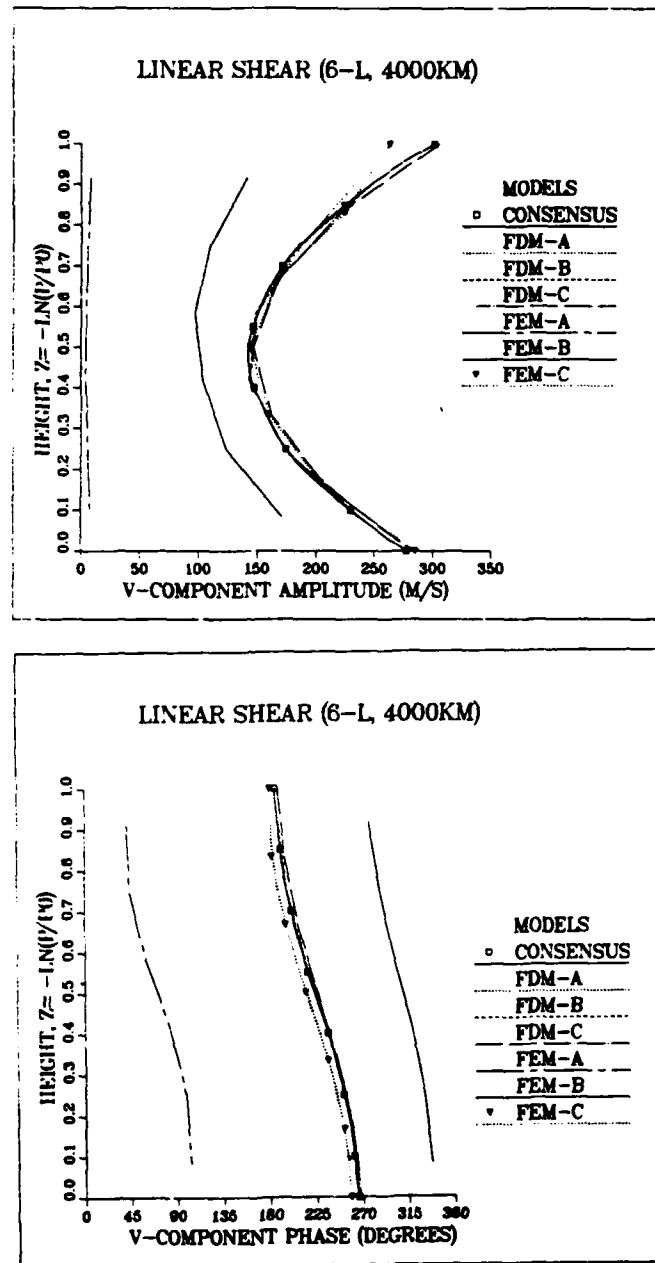


Fig. 9. 6-layer, 4000 km linear shear experiment at 96 h comparing v-component amplitudes (top) and phases (bottom).

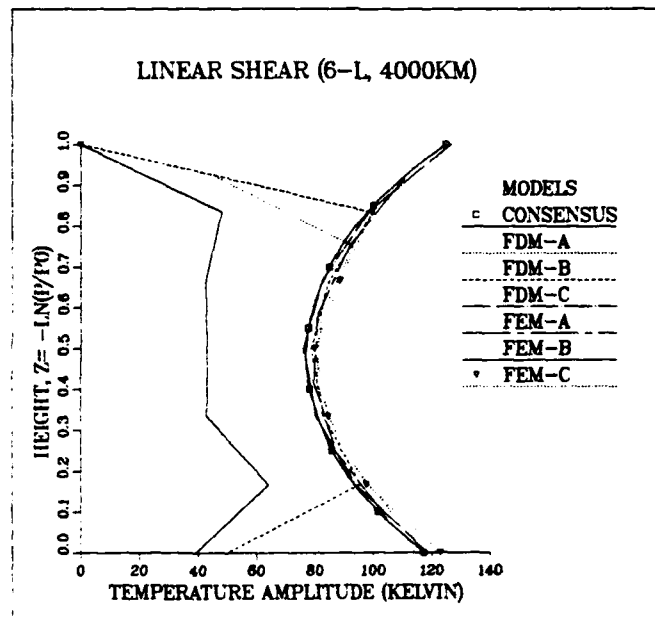


Fig. 10. 6-layer, 4000 km linear shear experiment at 96 h comparing temperature amplitudes.

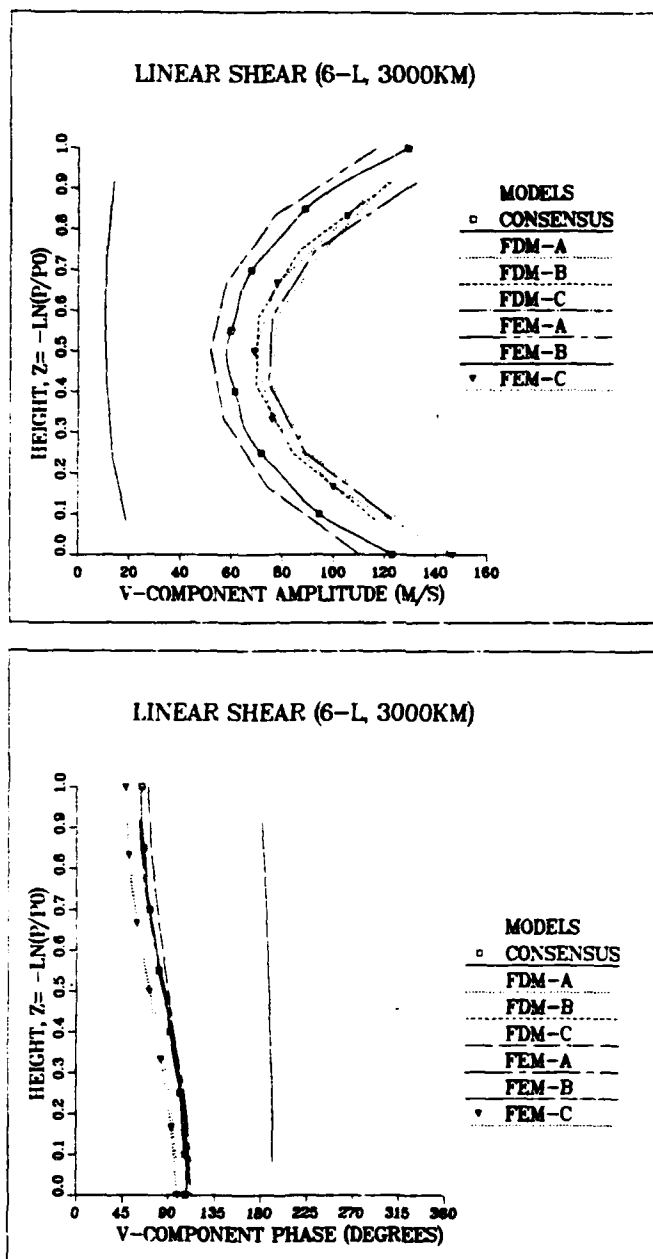


Fig. 11. 6-layer, 3000 km linear shear experiment at 96 h comparing v-component amplitudes (top) and phases (bottom).

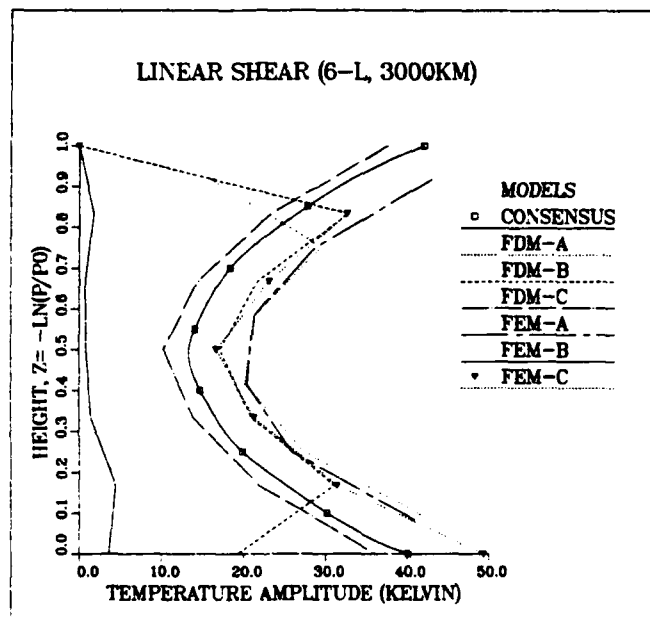


Fig. 12. 6-layer, 3000 km linear shear experiment at 96 h comparing temperature amplitudes.

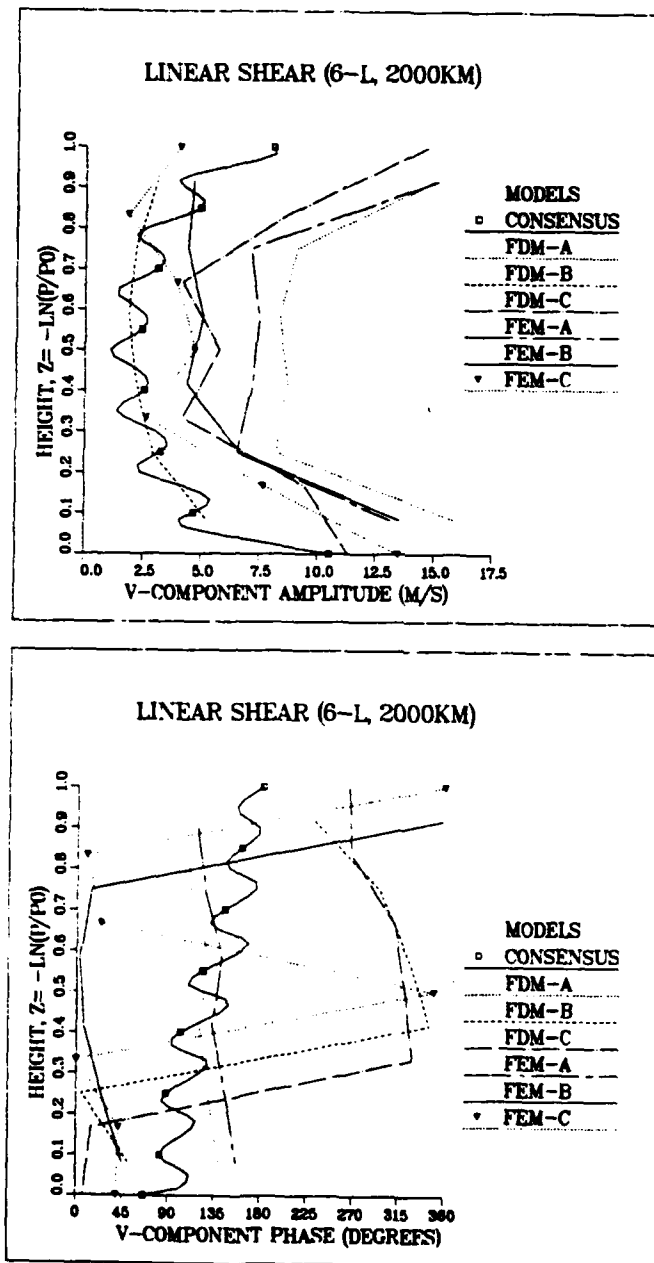


Fig. 13. 6-layer, 2000 km linear shear experiment at 96 h comparing v-component amplitudes (top) and phases (bottom).

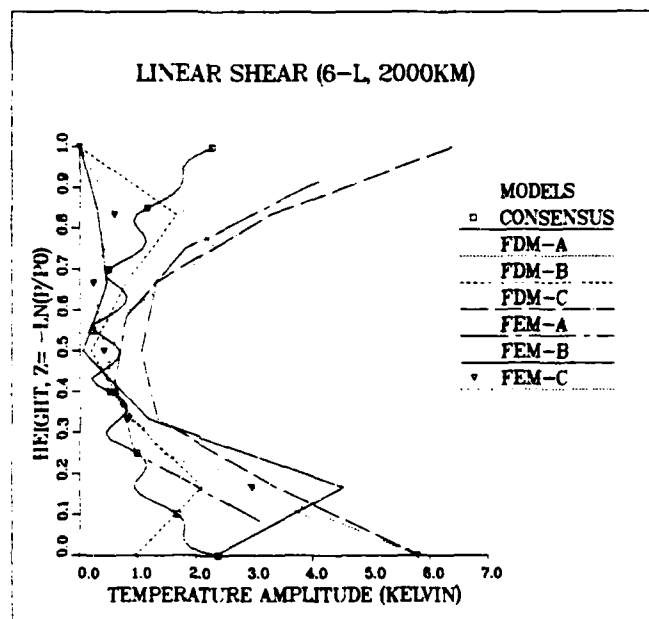


Fig. 14. 6-layer, 2000 km linear shear experiment at 96 h comparing temperature amplitudes.

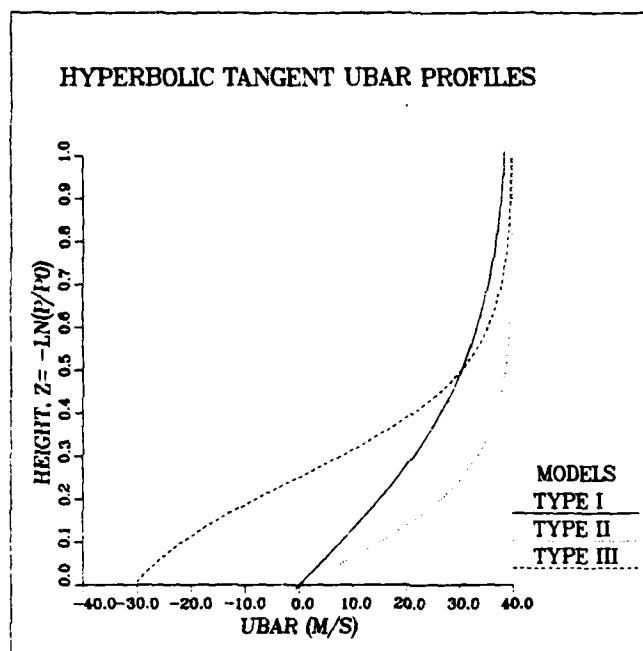


Fig. 15. Hyperbolic tangent ubar profiles.

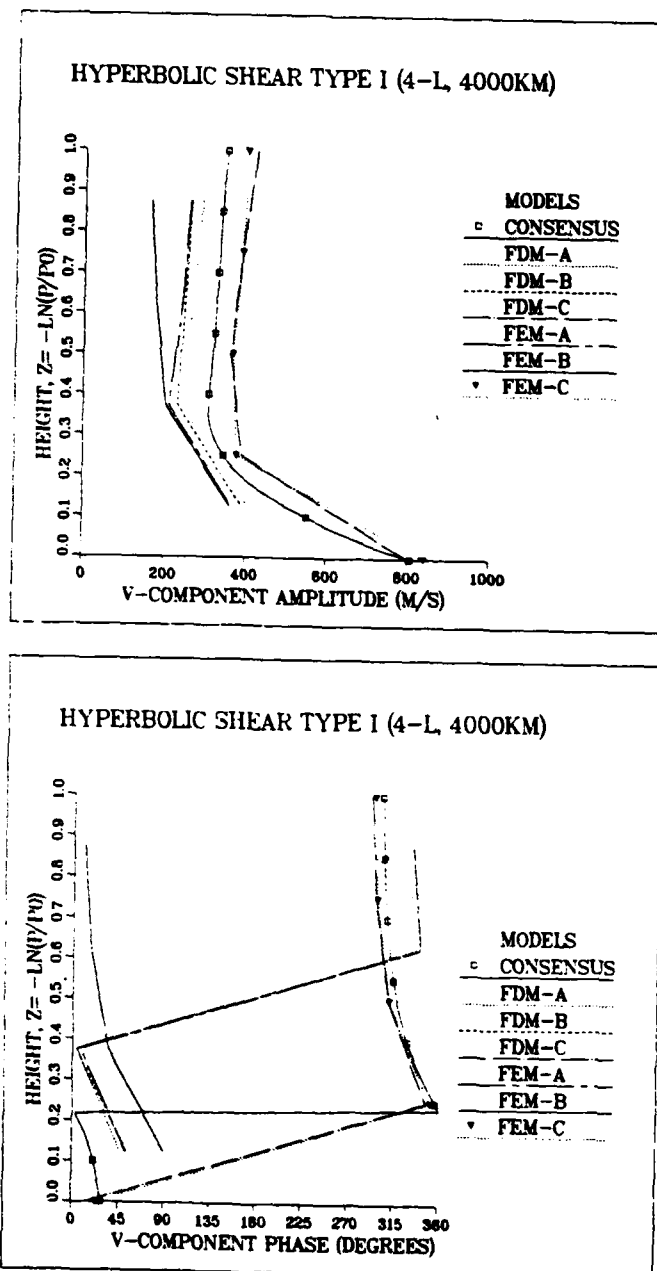


Fig. 16. 4-layer, 4000 km Type I shear experiment at 96 h comparing v-component amplitudes (top) and phases (bottom).

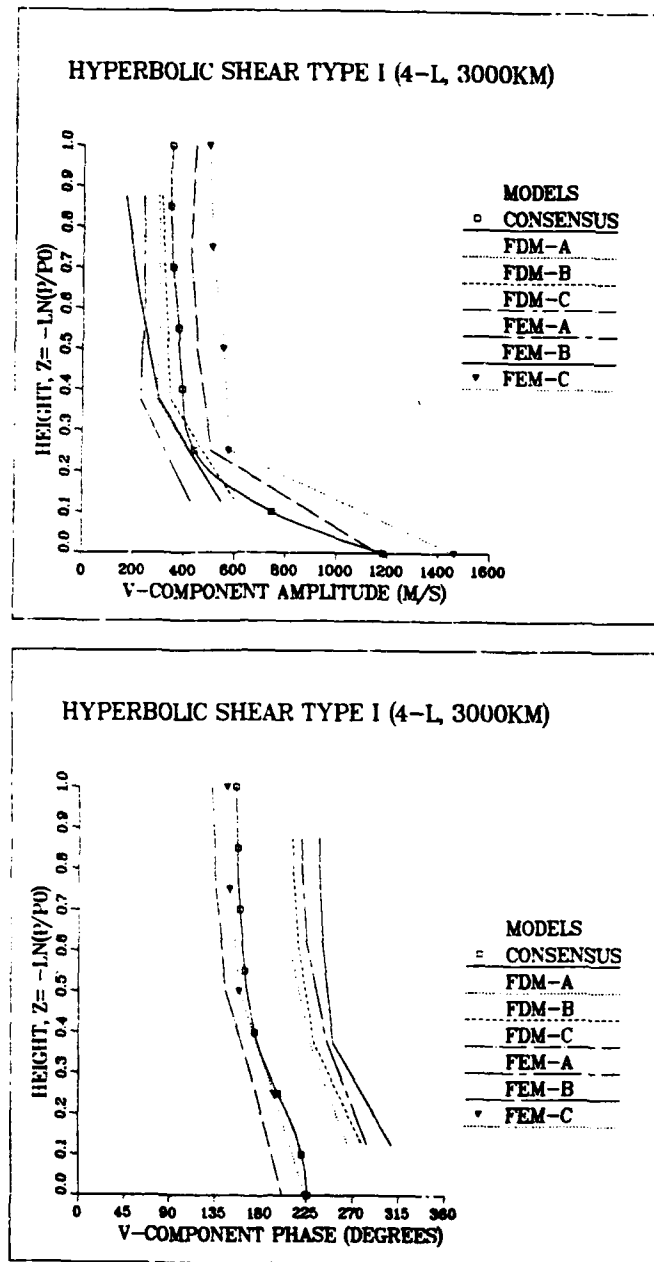


Fig. 17. 4-layer, 3000 km Type I shear experiment at 96 h comparing v-component amplitudes (top) and phases (bottom).

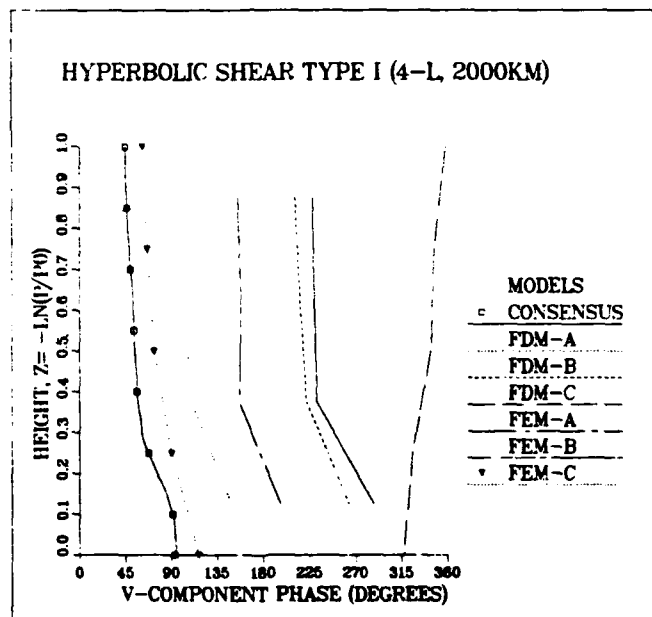
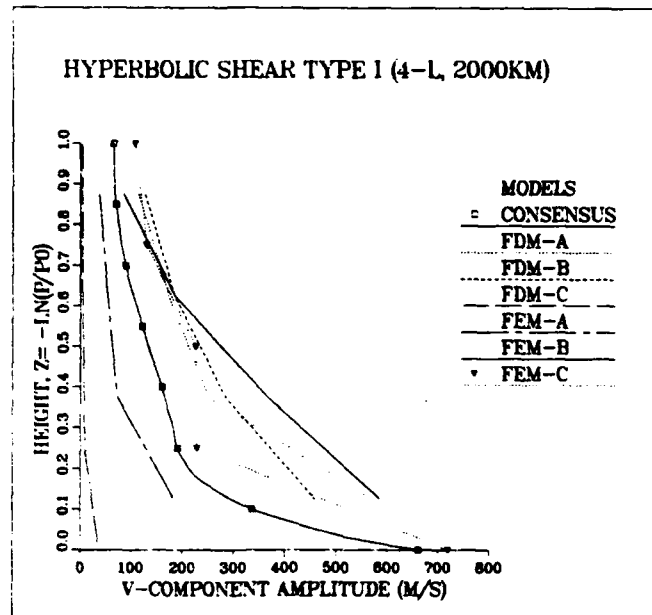


Fig. 18. 4-layer, 2000 km Type I shear experiment at 96 h comparing v-component amplitudes (top) and phases (bottom).

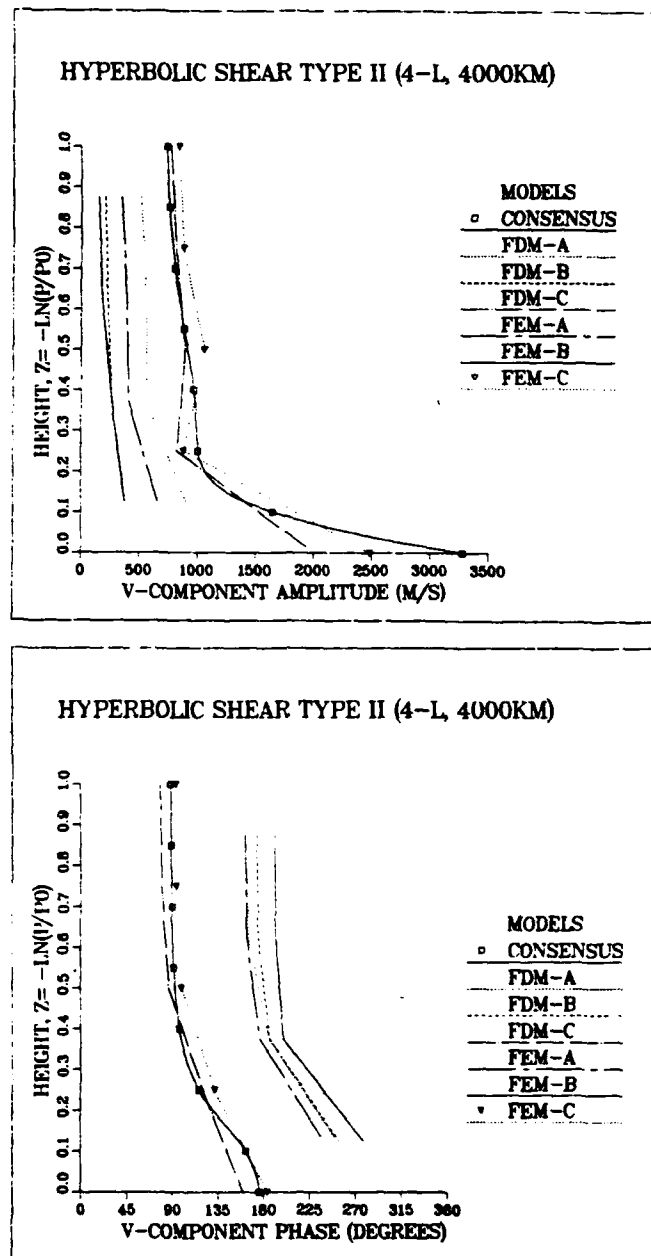


Fig. 19. 4-layer, 4000 km Type II shear experiment at 96 h comparing v-component amplitudes (top) and phases (bottom).

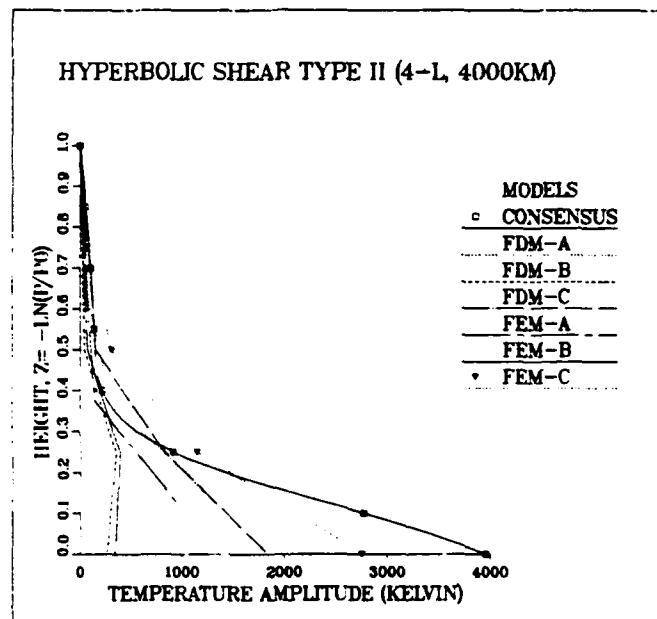


Fig. 20. 4-layer, 4000 km Type II shear experiment at 96 h comparing temperature amplitudes.

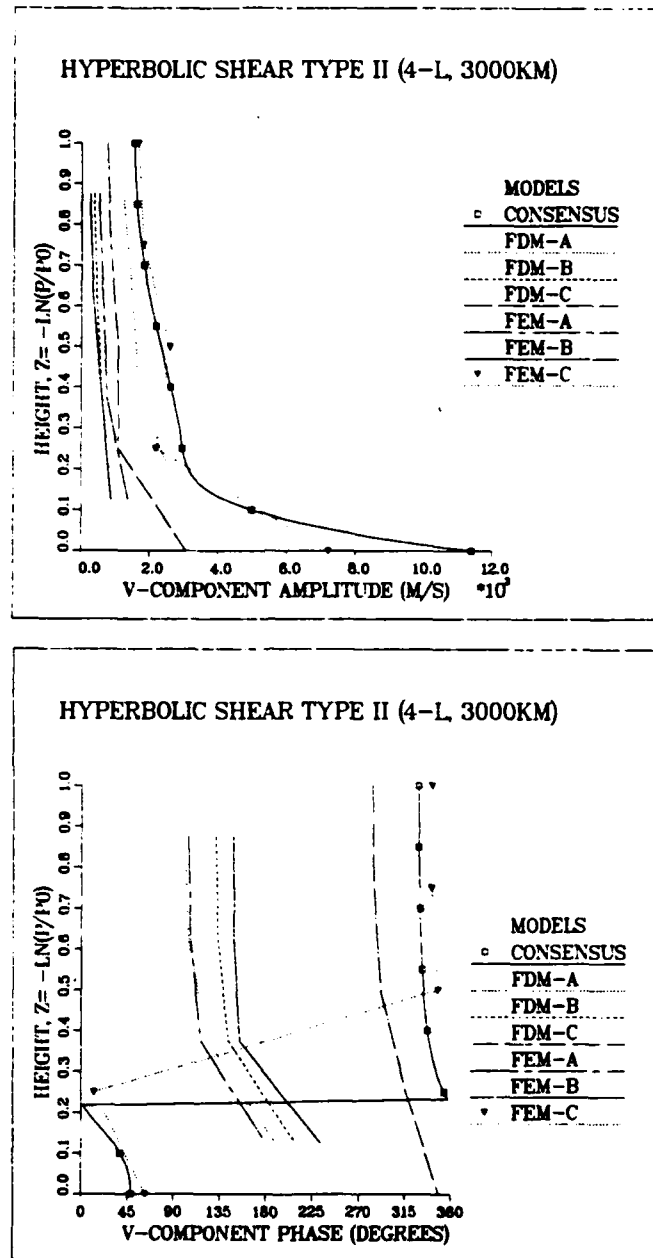


Fig. 21. 4-layer, 3000 km Type II shear experiment at 96 h comparing v-component amplitudes (top) and phases (bottom).

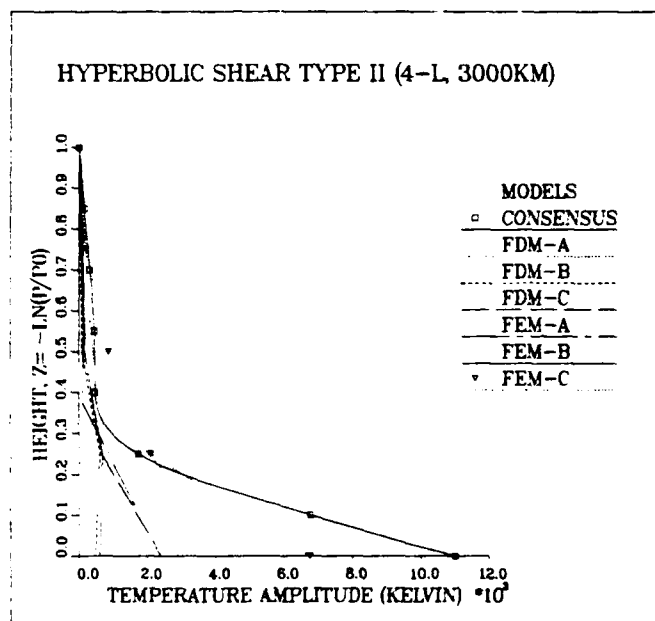


Fig. 22. 4-layer, 3000 km Type II shear experiment at 96 h comparing temperature amplitudes.

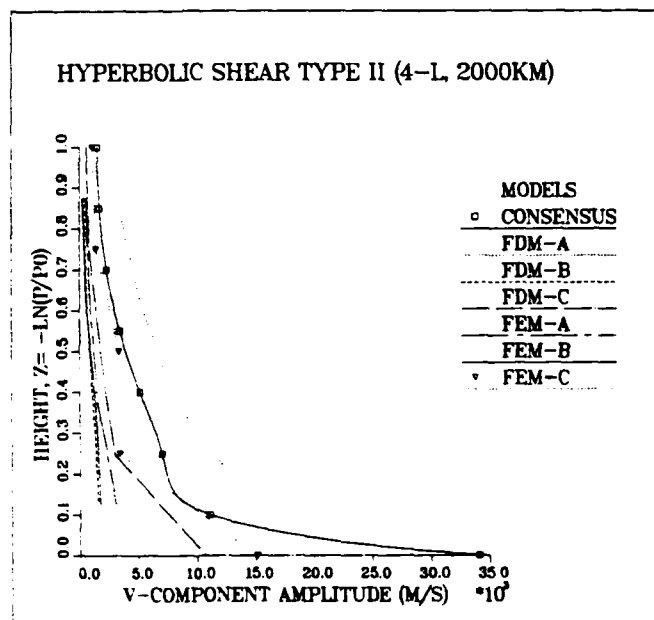


Fig. 23. 4-layer, 2000 km Type II shear experiment at 96 h comparing v-component amplitudes.

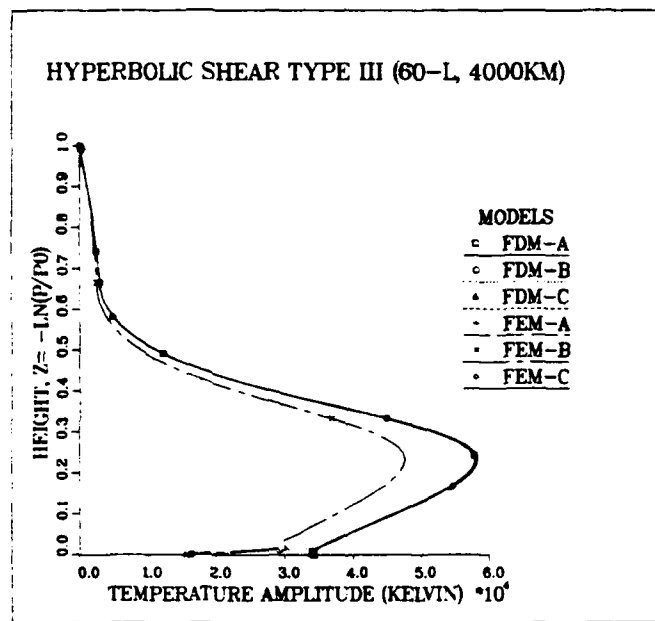


Fig. 24. 60-layer, 4000 km Type III shear experiment at 96 h comparing temperature amplitudes.

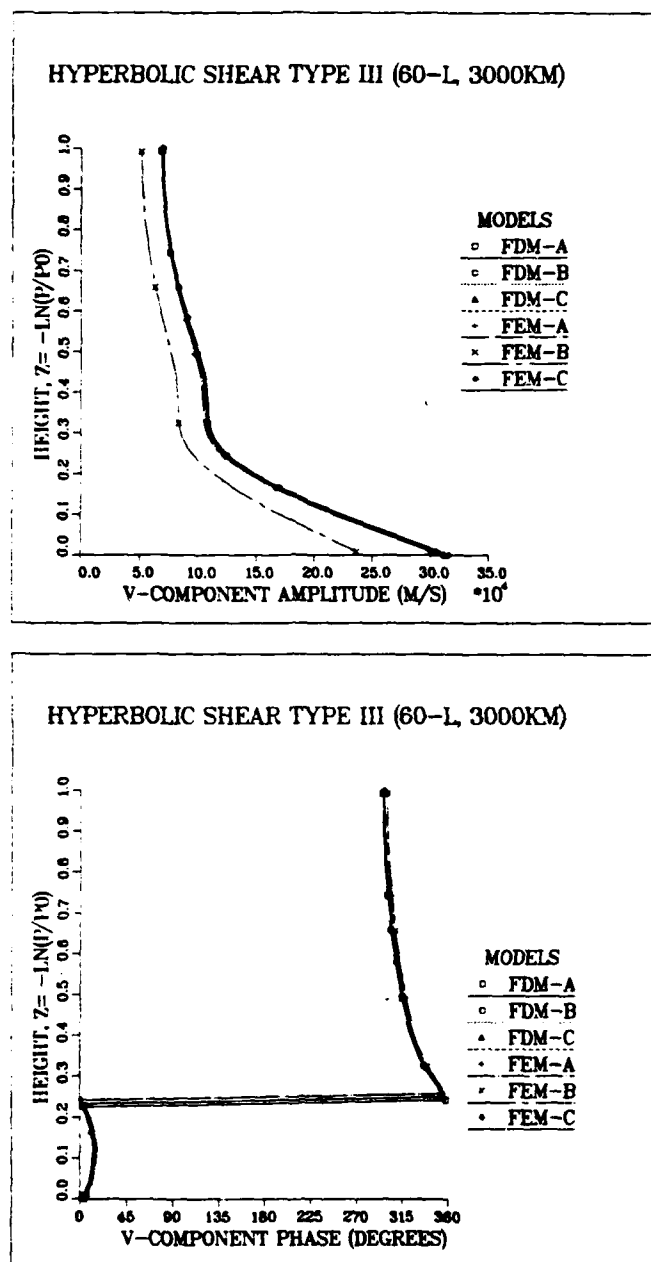


Fig. 25. 60-layer, 3000 km Type III shear experiment at 96 h comparing v-component amplitudes (top) and phases (bottom).

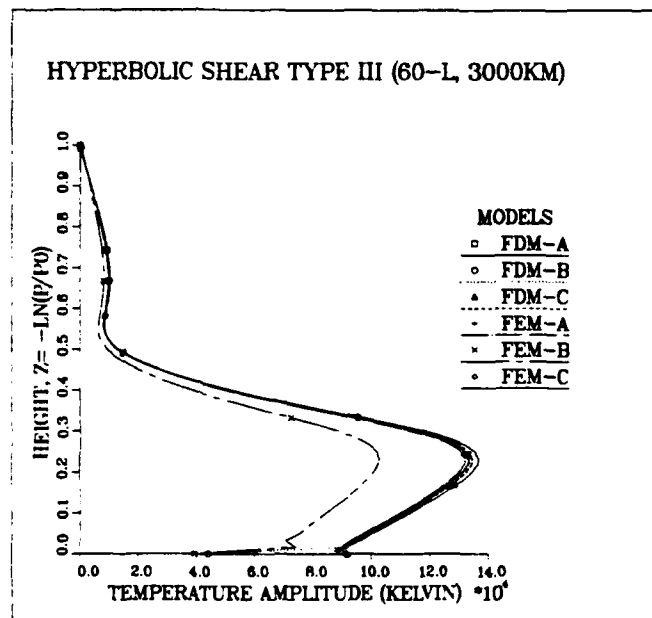


Fig. 26. 60-layer, 3000 km Type III shear experiment at 96 h comparing temperature amplitudes.

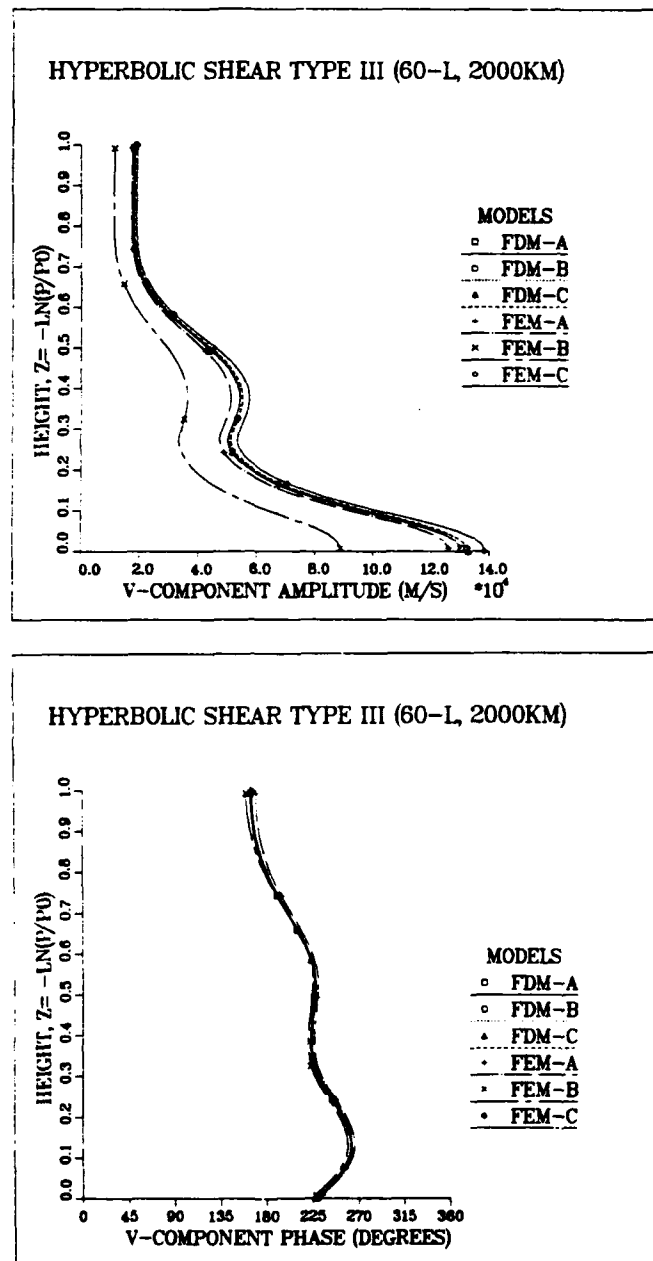


Fig. 27. 60-layer, 2000 km Type III shear experiment at 96 h comparing v-component amplitudes (top) and phases (bottom).

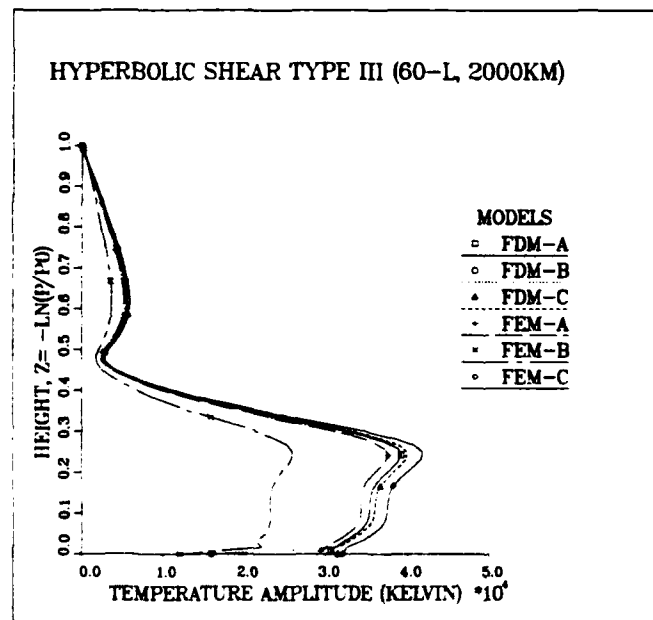


Fig. 28. 60-layer, 2000 km Type III shear experiment at 96 h comparing temperature amplitudes.

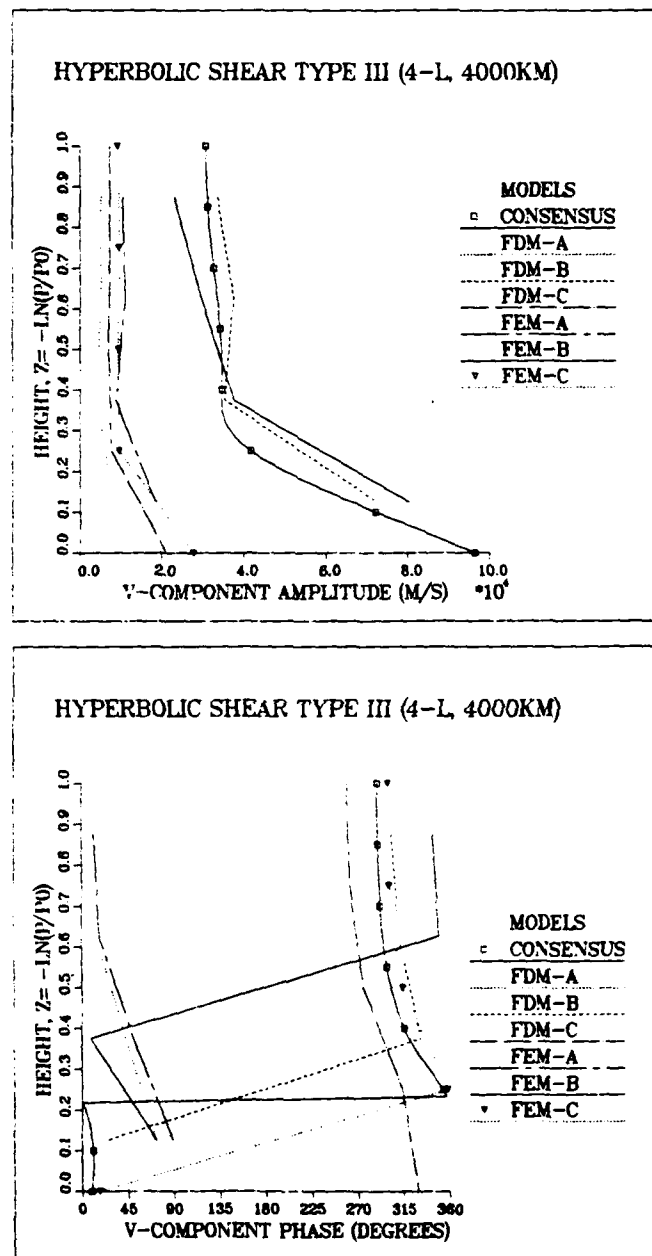


Fig. 29. 4-layer, 4000 km Type III shear experiment at 96 h comparing v-component amplitudes (top) and phases (bottom).

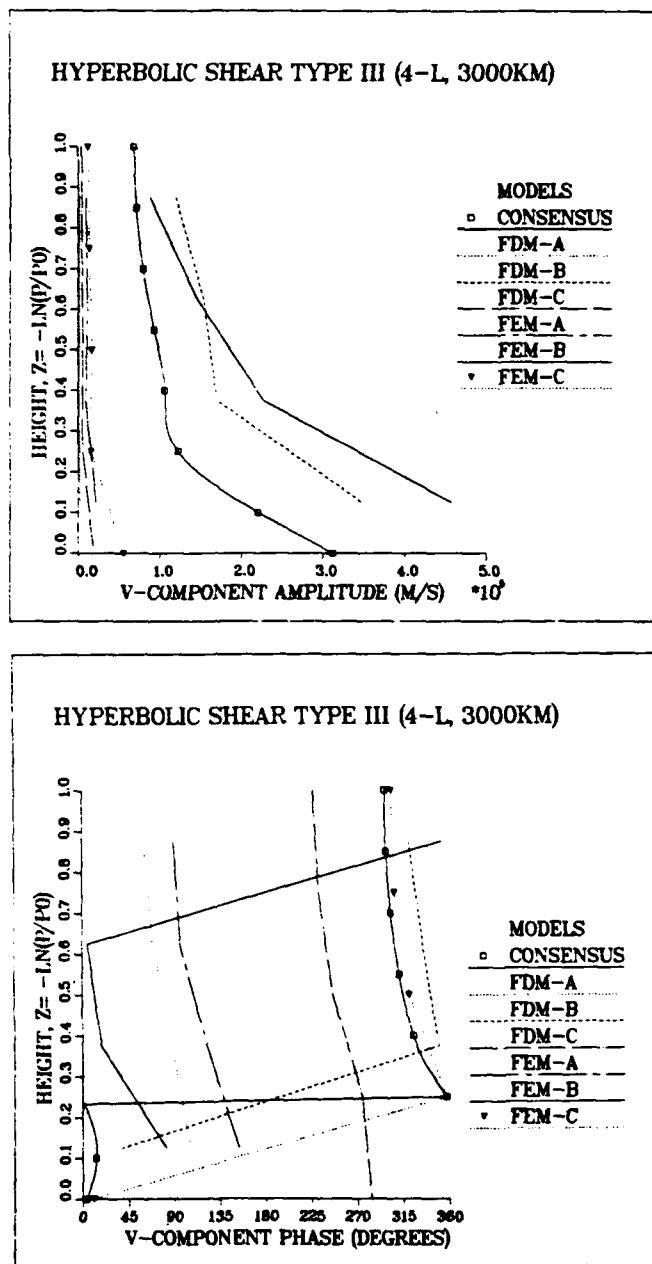


Fig. 30. 4-layer, 3000 km Type III shear experiment at 96 h comparing v-component amplitudes (top) and phases (bottom).

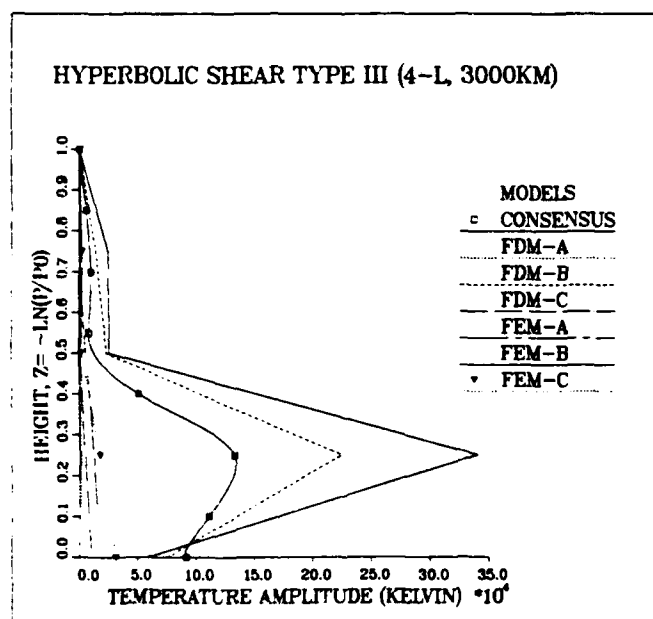


Fig. 31. 4-layer, 3000 km Type III shear experiment at 96 h comparing temperature amplitudes.

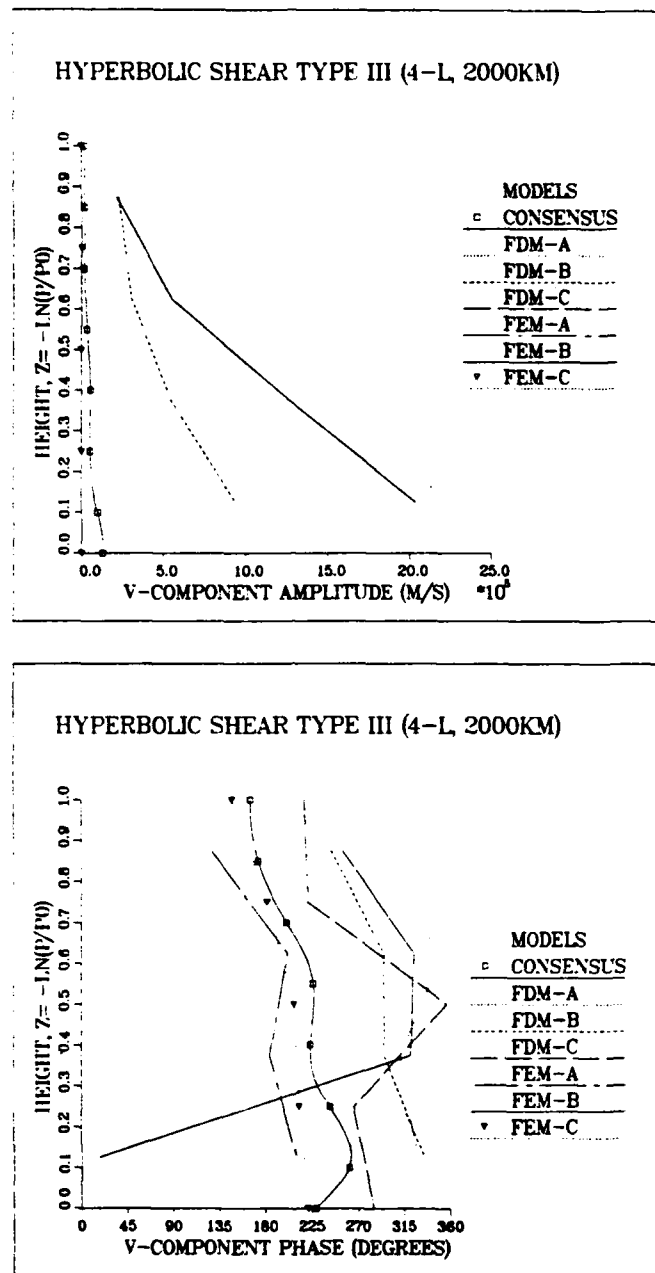


Fig. 32. 4-layer, 2000 km Type III shear experiment at 96 h comparing v-component amplitudes (top) and phases (bottom).

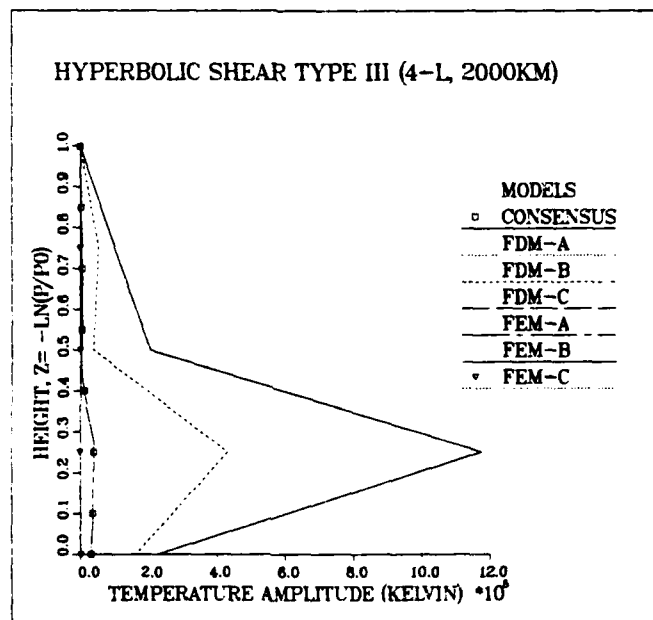


Fig. 33. 4-layer, 2000 km Type III shear experiment at 96 h comparing temperature amplitudes.

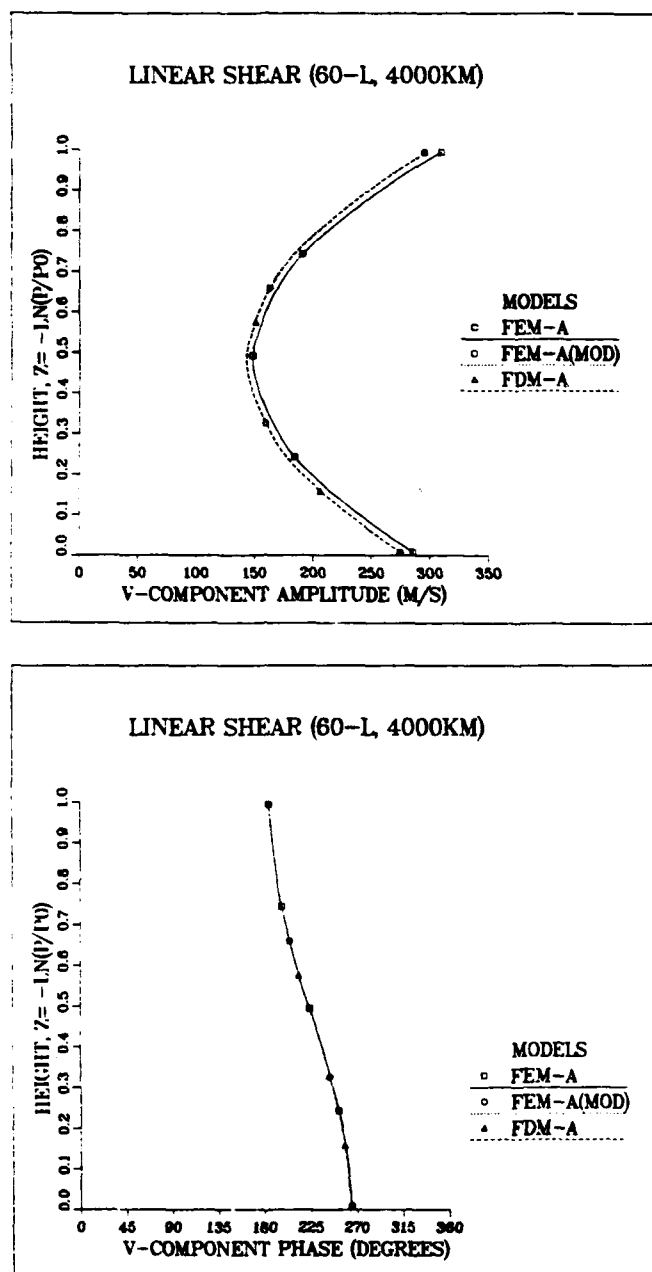


Fig. 34. 60-layer, 4000 km linear thermodynamic modification at 96 h comparing v-component amplitudes (top) and phases (bottom).

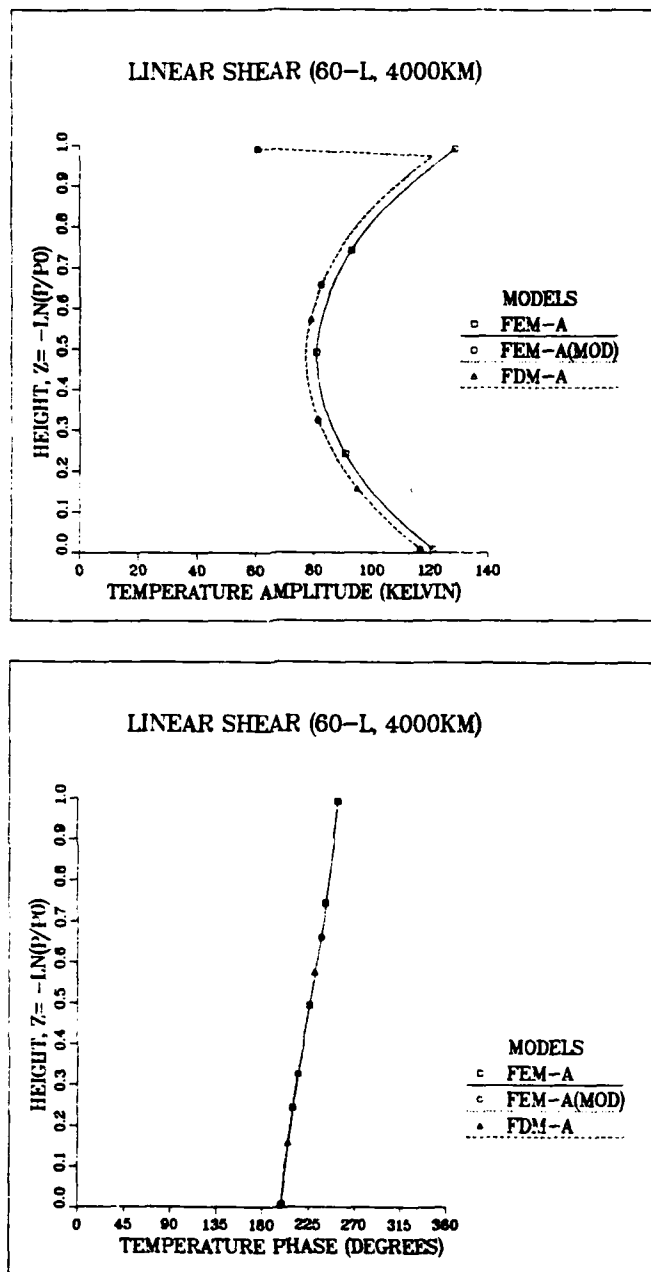


Fig. 35. 60-layer, 4000 km linear thermodynamic modification at 96 h comparing temperature amplitudes (top) and phases (bottom).

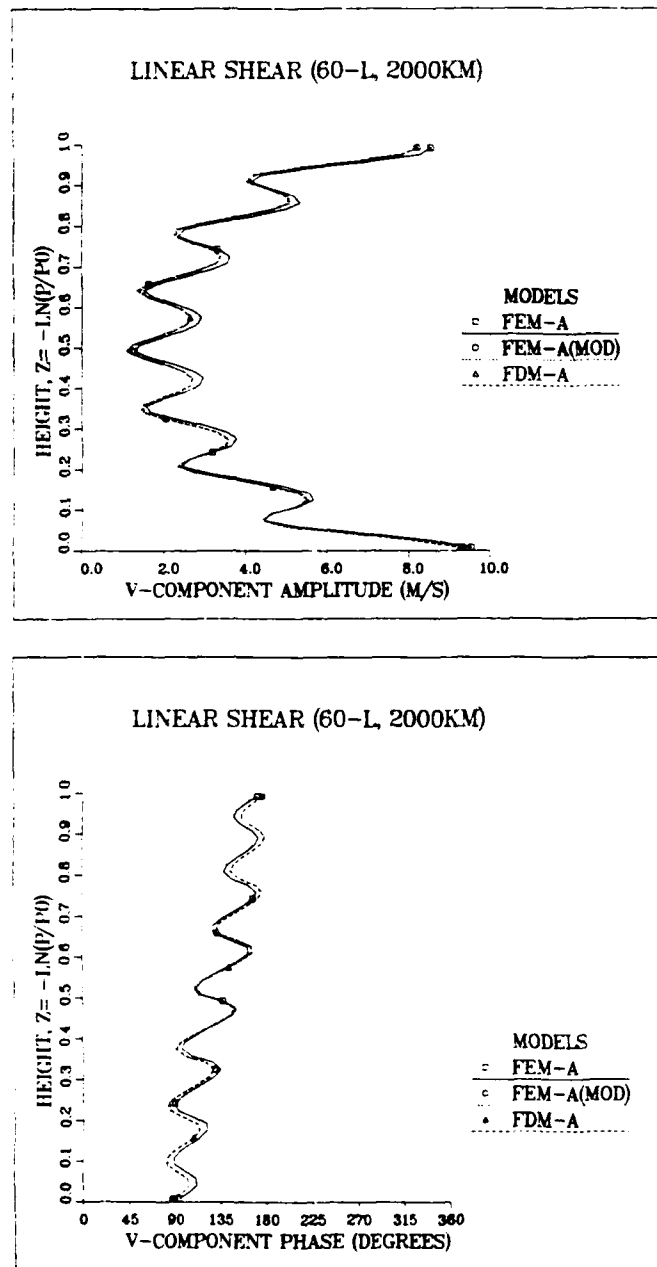


Fig. 36. 60-layer, 2000 km linear thermodynamic modification at 96 h comparing v-component amplitudes (top) and phases (bottom).

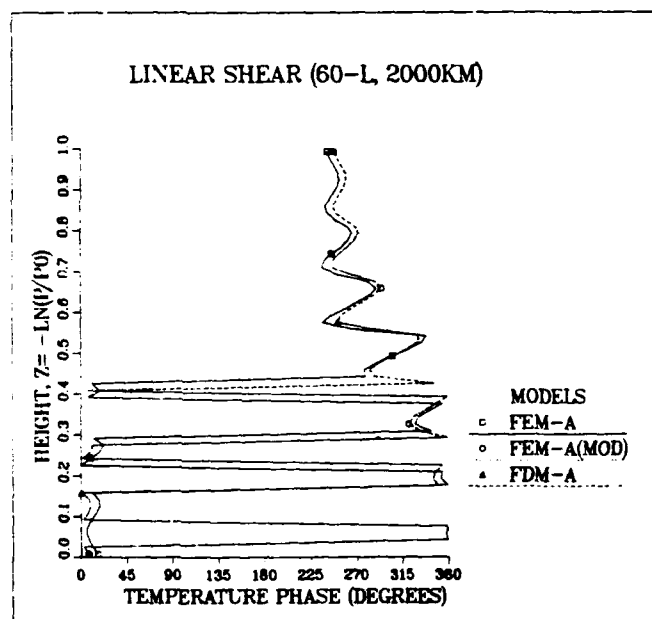
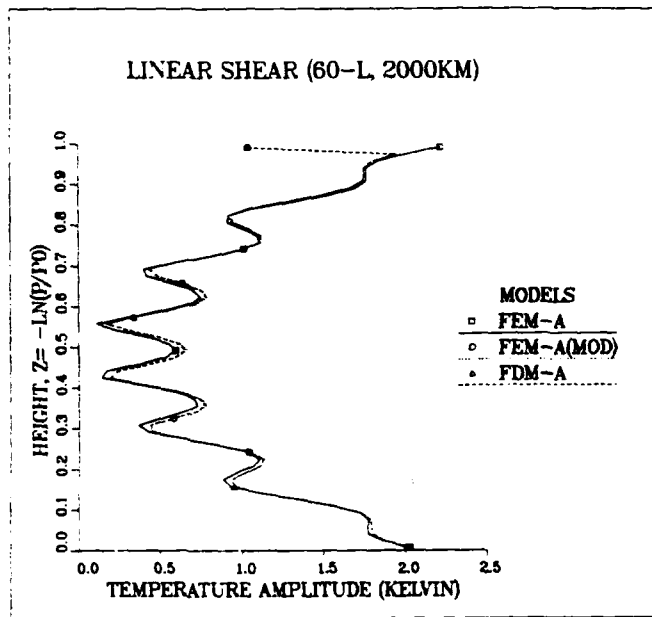


Fig. 37. 60-layer, 2000 km linear thermodynamic modification at 96 h comparing temperature amplitudes (top) and phases (bottom).

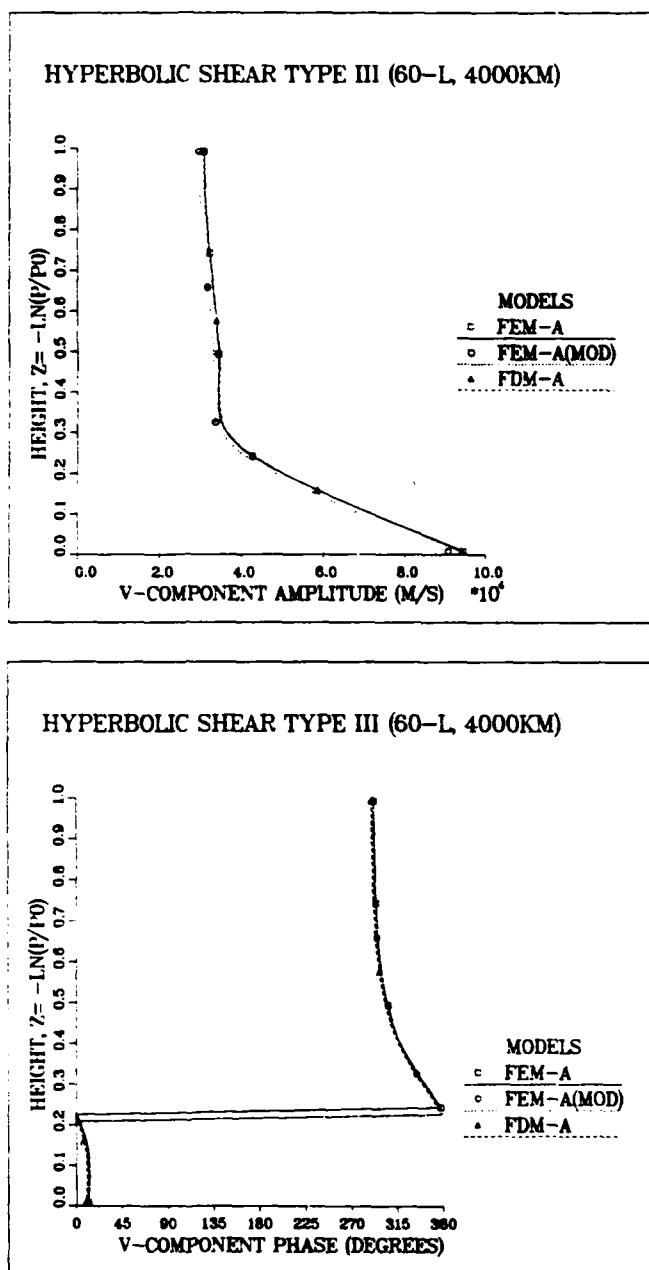


Fig. 38. 60-layer, 4000 km Type III thermodynamic modification at 96 h comparing v-component amplitudes (top) and phases (bottom).

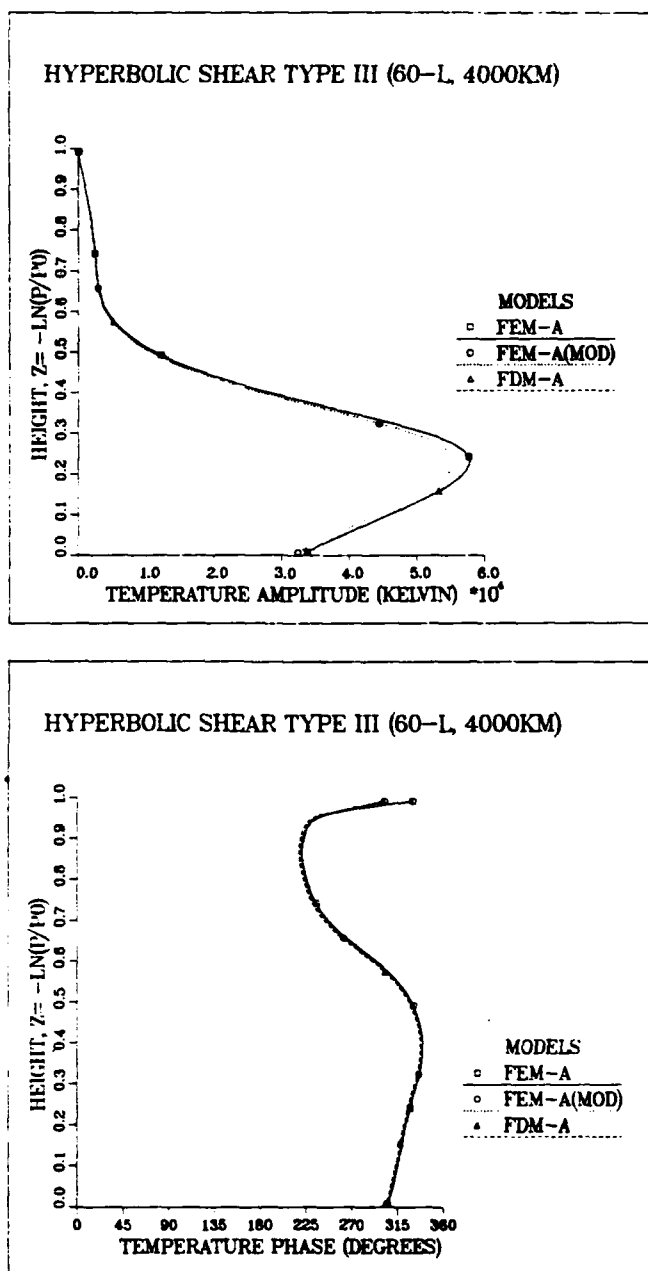


Fig. 39. 60-layer, 4000 km Type III thermodynamic modification at 96 h comparing temperature amplitudes (top) and phases (bottom).

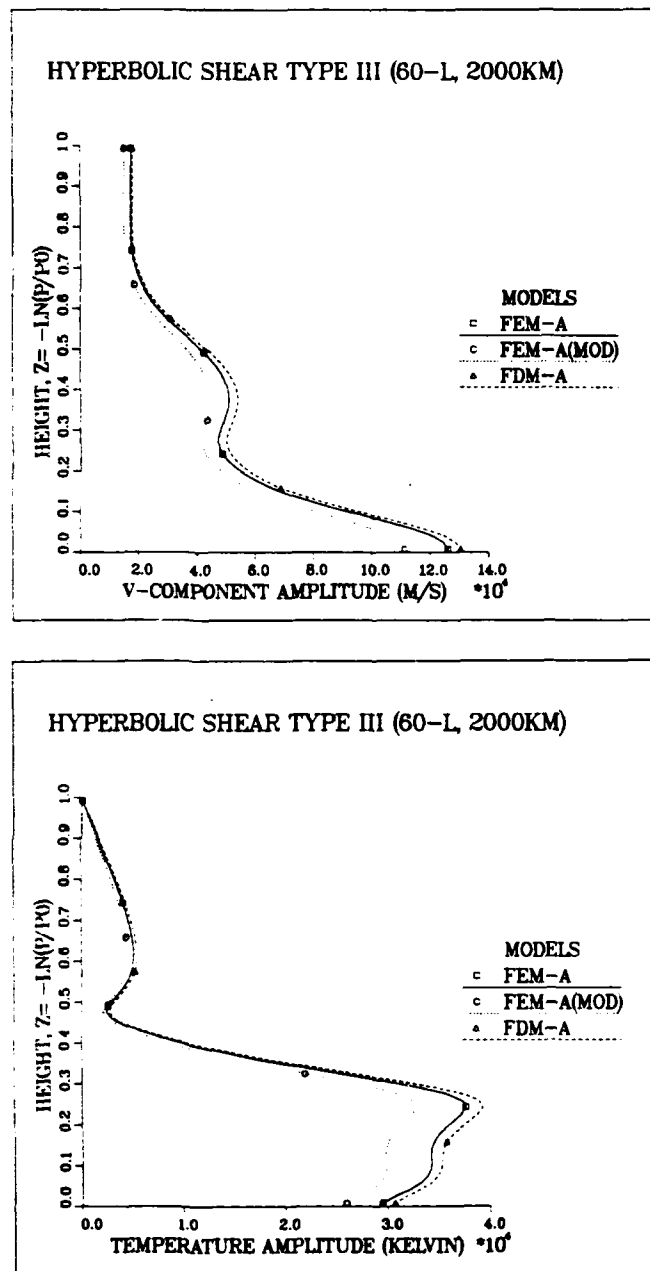


Fig. 40. 60-layer, 2000 km Type III thermodynamic modification comparing v-component (top) and temperature (bottom) amplitudes.

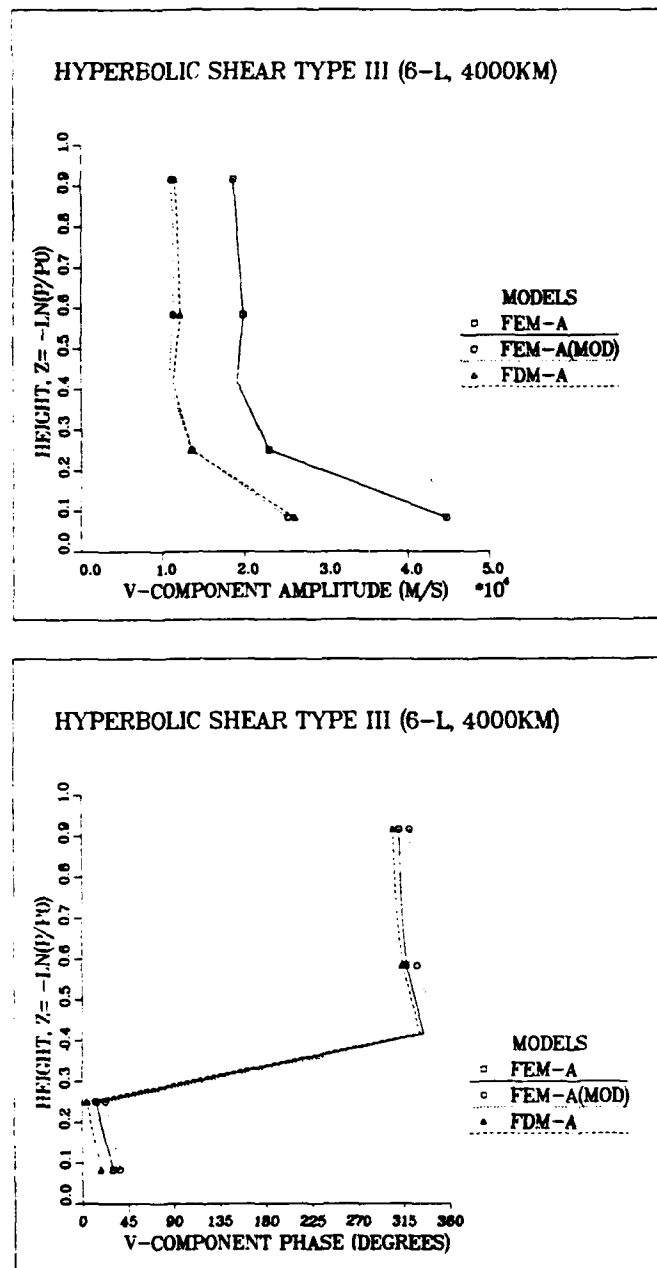


Fig. 41. 6-layer, 4000 km Type III thermodynamic modification at 96 h comparing v-component amplitudes (top) and phases (bottom).

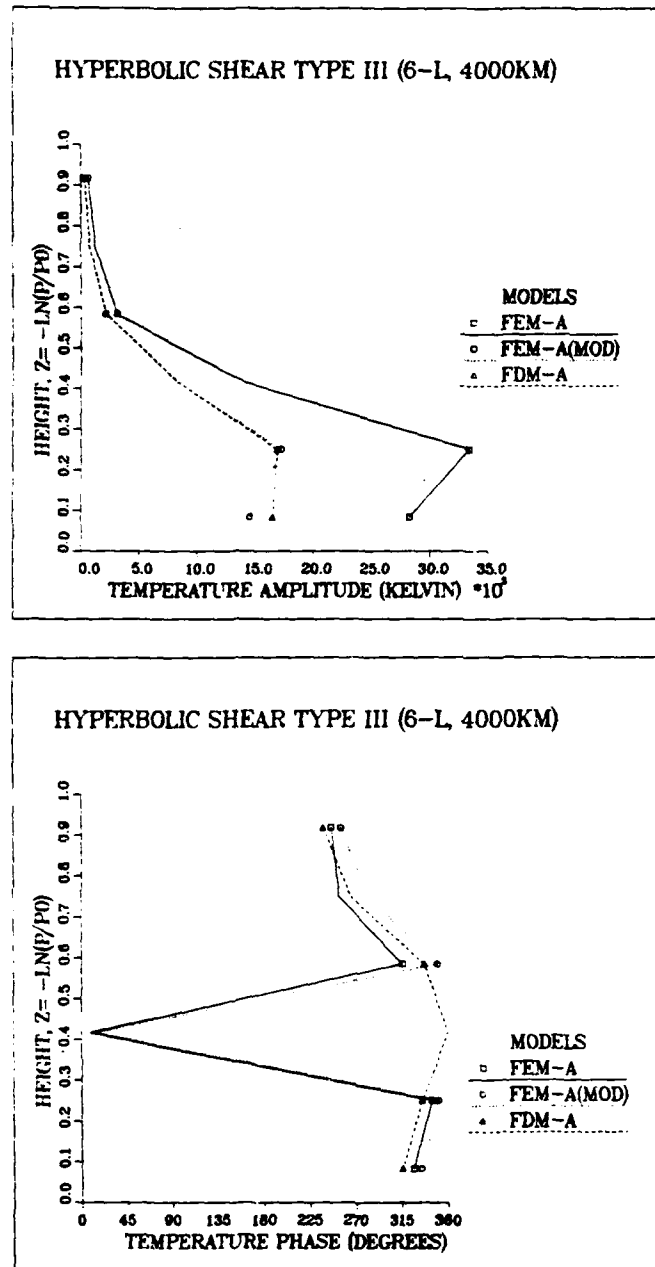


Fig. 42. 6-layer, 4000 km Type III thermodynamic modification at 96 h comparing temperature amplitudes (top) and phases (bottom).

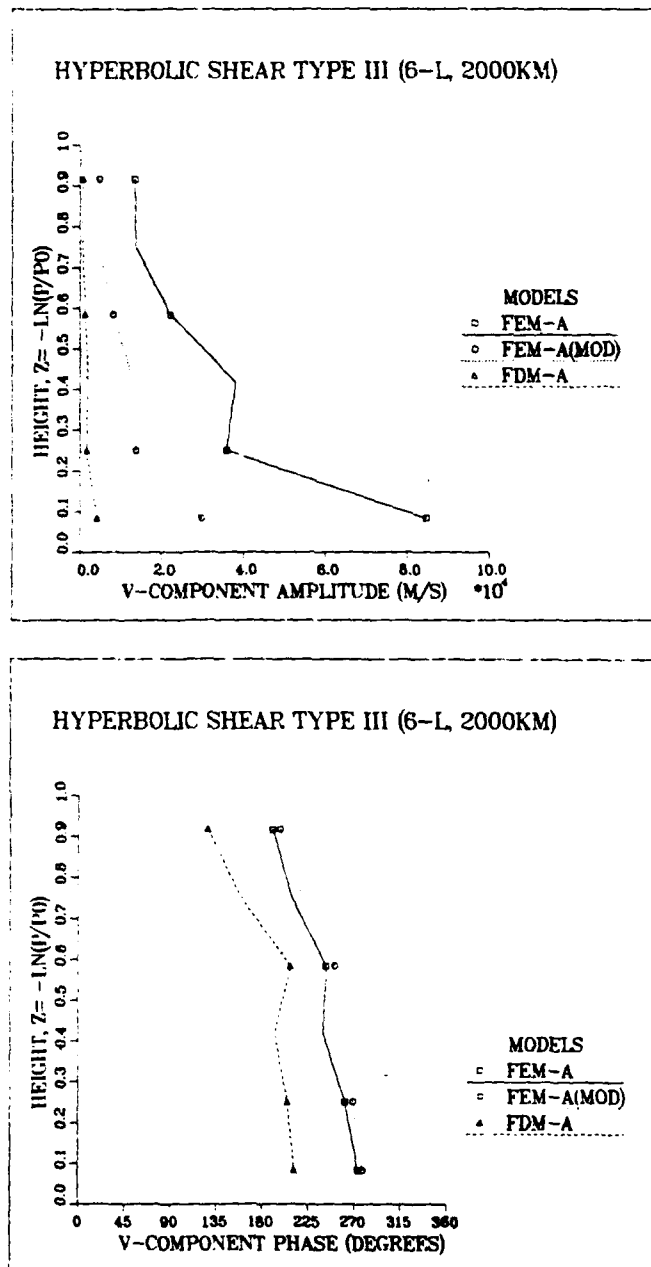


Fig. 43. 6-layer, 2000 km Type III thermodynamic modification at 96 h comparing v-component amplitudes (top) and phases (bottom).

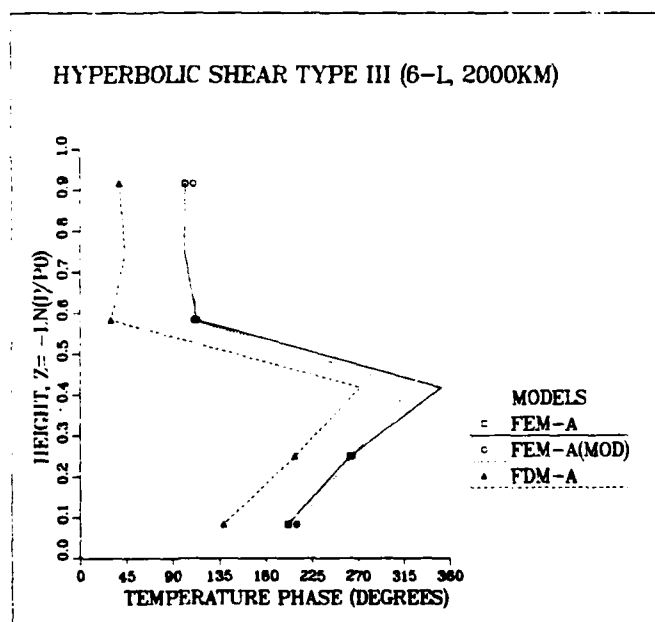
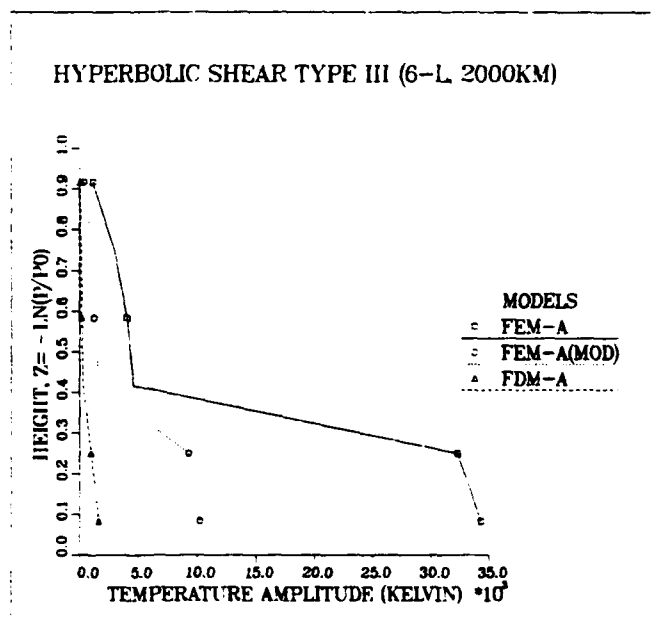


Fig. 44. 6-layer, 2000 km Type III thermodynamic modification at 96 h comparing temperature amplitudes (top) and phases (bottom).

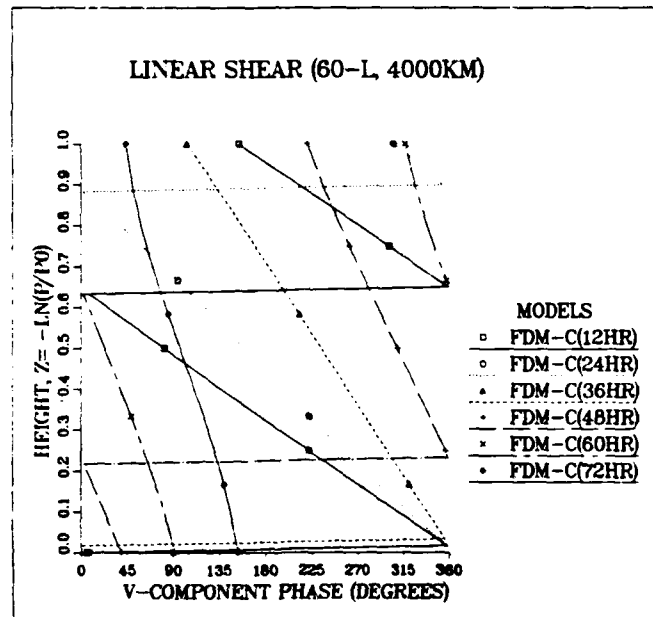
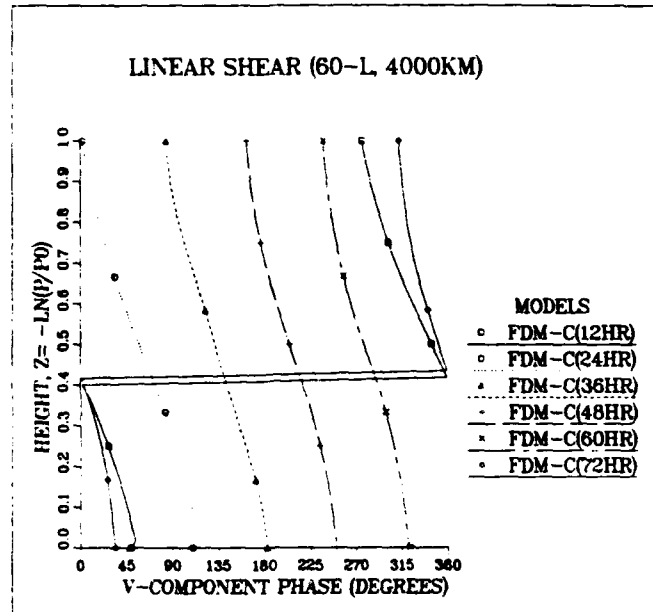


Fig. 45. 60-layer, 4000 km initial value modification (linear) comparing phase I (top) and phase II (bottom) negative phase tilt.

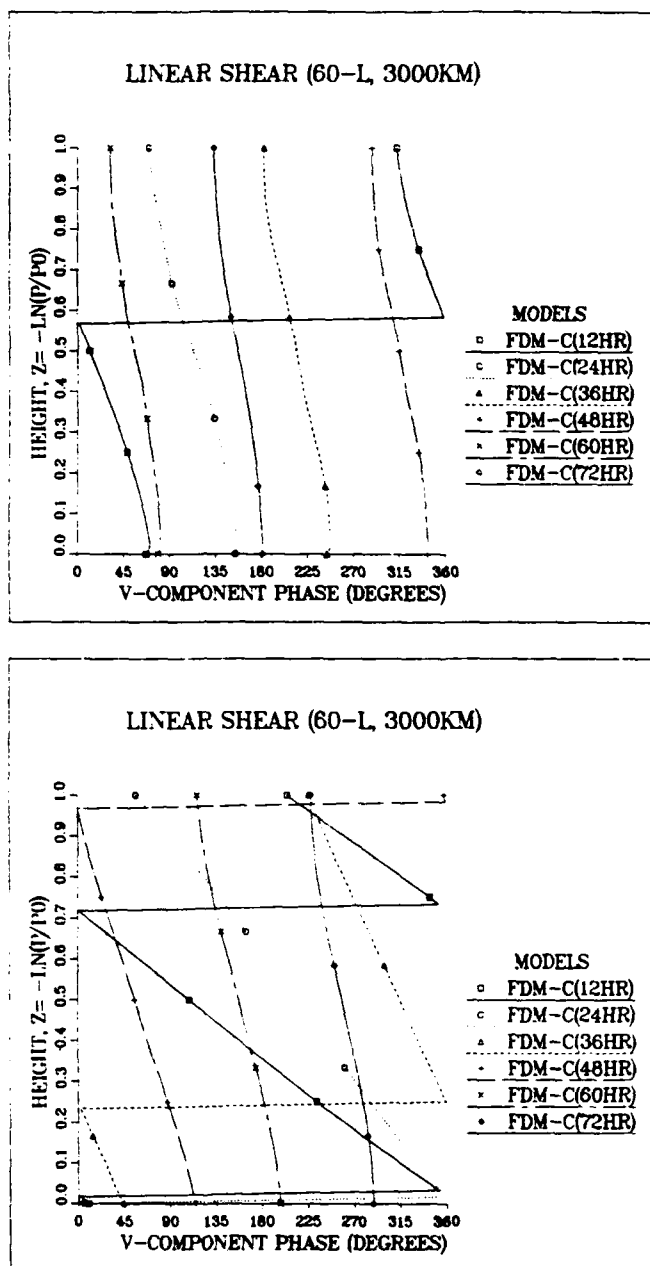


Fig. 46. 60-layer, 3000 km initial value modification (linear) comparing phase I (top) and phase II (bottom) negative phase tilt.

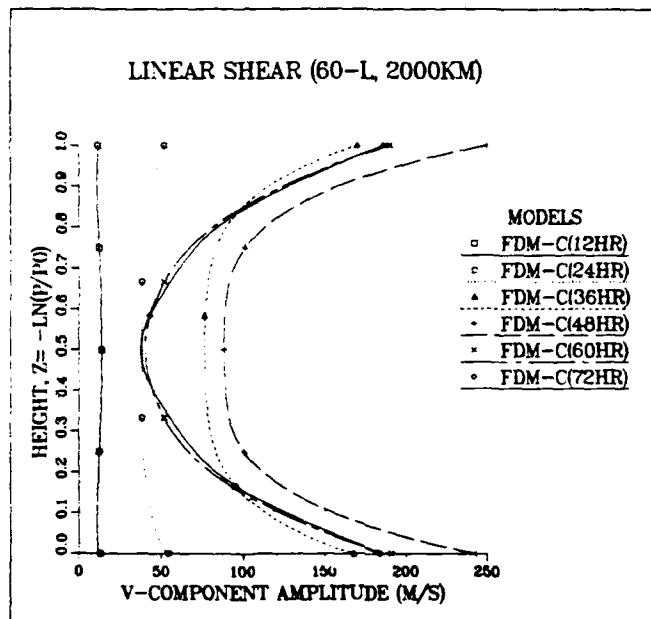
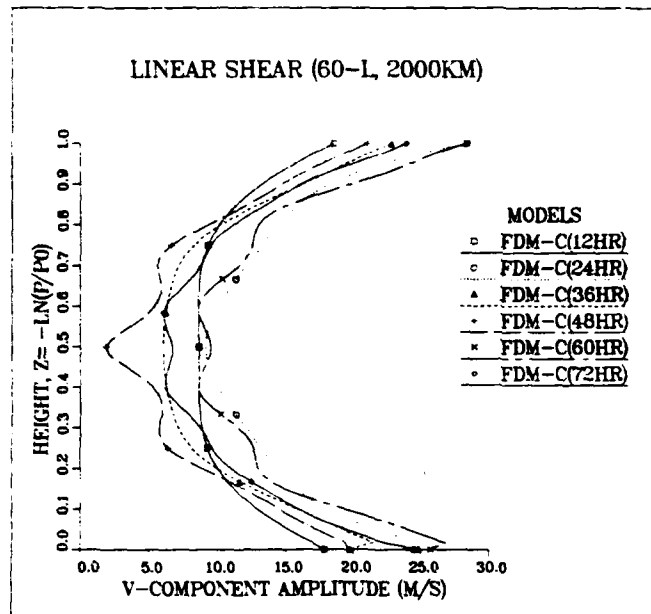


Fig. 47. 60-layer, 2000 km initial value modification (linear) comparing phase I (top) and phase II (bottom) amplitudes.

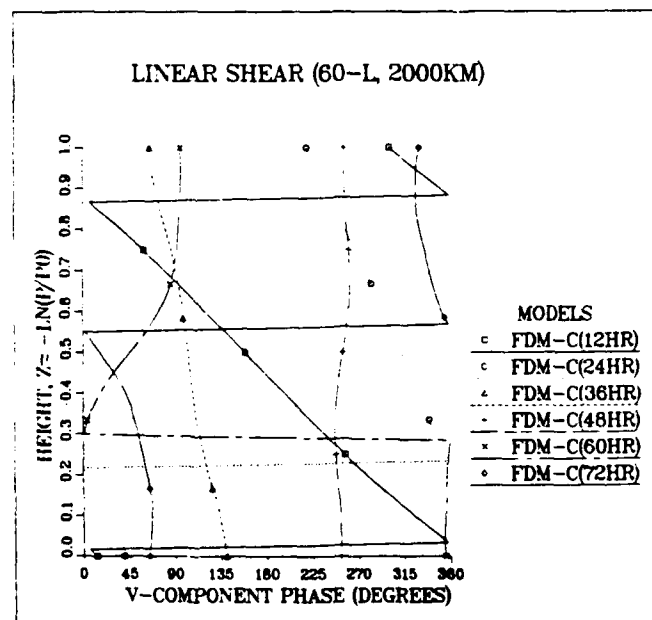
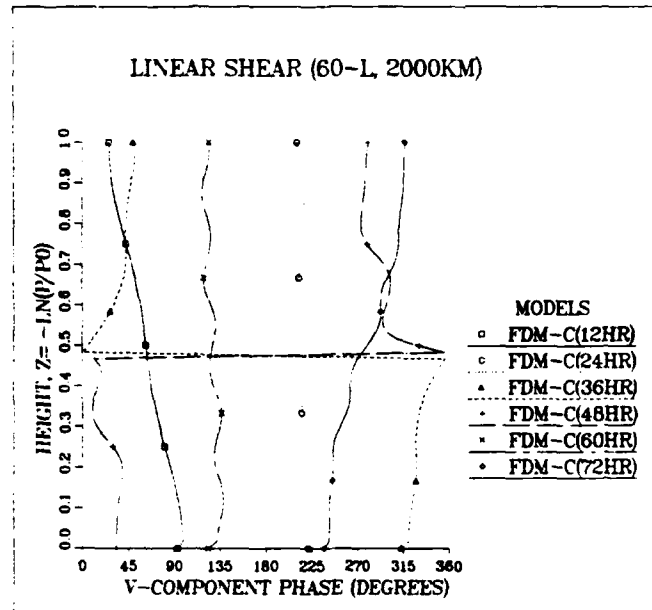


Fig. 48. 60-layer, 2000 km initial value modification (linear) comparing phase I (top) and phase II (bottom) negative phase tilt.

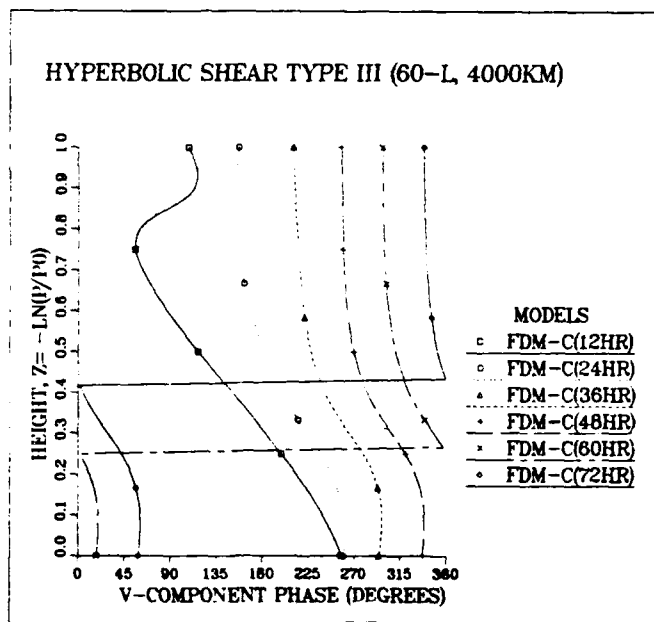
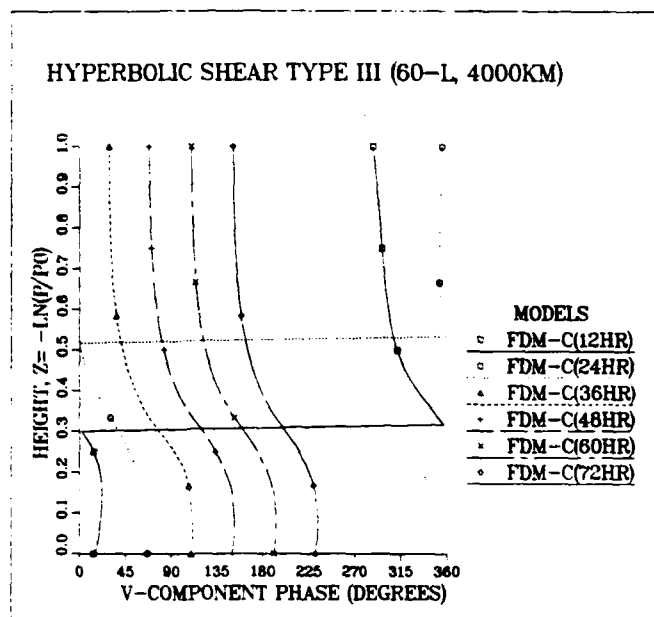


Fig. 49. 60-layer, 4000 km initial value modification (Type III) comparing phase I (top) and phase II (bottom) negative phase tilt.

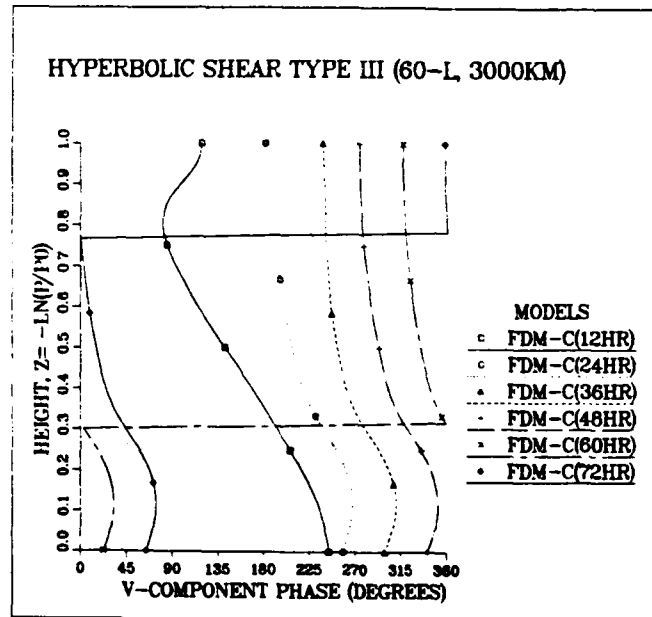
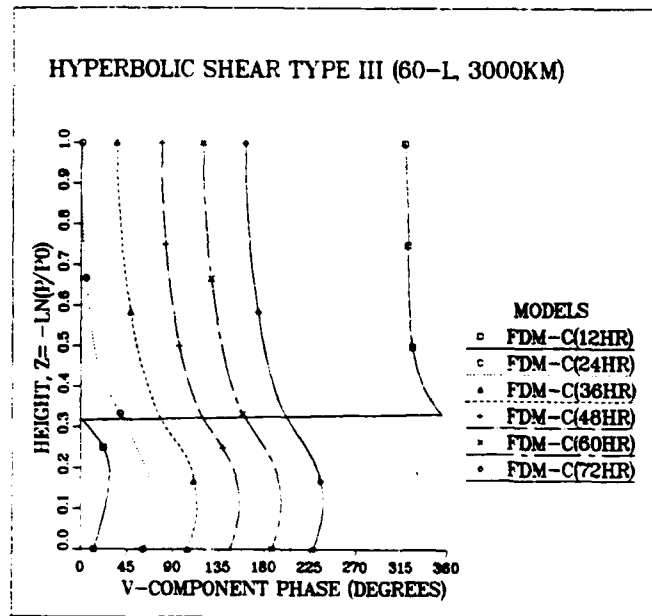


Fig. 50. 60-layer, 3000 km initial value modification (Type III) comparing phase I (top) and phase II (bottom) negative phase tilt.

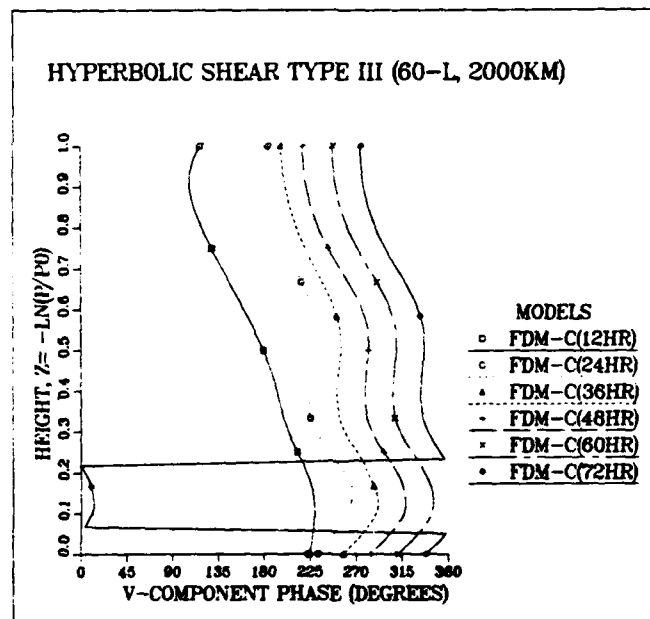
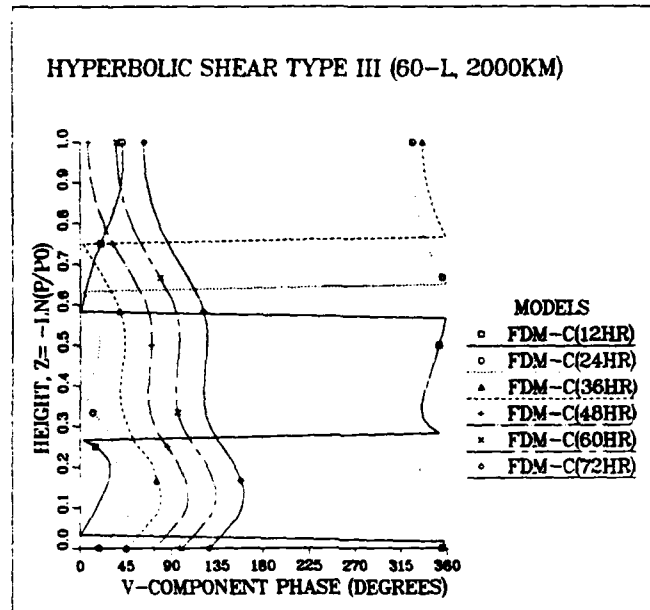


Fig. 51. 60-layer, 2000 km initial value modification (Type III) comparing phase I (top) and phase II (bottom) negative phase tilt.

IV. CONCLUSIONS

With a linear vertical ubar profile, FEM-B still has an oscillation near the lower boundary of the temperature profile after correcting the length of the vertical velocity vector and is the poorest of the six models. FEM-A is better than FEM-B but is still not equal to the consensus profile. In the hyperbolic tangent vertical ubar profiles, the finite element models do not perform as well as the finite difference models for Types I and II except for the six-layer model for Type II. Grid A is closest to the consensus for most of the Type I and Type II cases. However, for Type III, the finite element models are better than the finite difference models in many of the cases. FEM-B shows much improvement in Type III. This may be because the maximum vertical shear in the ubar field occurs near $Z = 0.25$, which may be far enough from the boundary to enable FEM-B to overcome its earlier problems near the boundary.

Overall, scheme C is often better than A and B, especially FEM-C. Scheme C may have an advantage because it predicts the variables at one more level than the A and B models except for the vertical velocity and temperature. However, even for the temperature profile, where grid B predicts the same number of levels as grid C, scheme C often has the better surface prediction. Grid A seems to perform surprisingly well in spite of the analysis of Arakawa (1984).

Future research should concentrate on the boundary elements for FEM-A and FEM-B. Perhaps new hybrid elements could be employed. Another approach would be to continue the work of isolating the effects of the vorticity, divergence and thermodynamic terms in the finite element models. This could be accomplished by using the finite difference method for these equations in the finite element models and observing each term's contribution.

So far, all the baroclinic instability experiments have used a T_{bar} field that increases linearly with height, which may not be too challenging for simple finite difference models to solve. A vertical T_{bar} field that is not linear, such as the hyperbolic tangent profile used for the ubar field in this study, may allow the finite element models to take full advantage of their possibilities. Finally, future work should continue the initial value growth experiments by evaluating all the models and by using smaller resolution models and smaller wavelength in x . Smaller horizontal wavelengths may lead to a different type of growth.

APPENDIX A. FINITE DIFFERENCE APPROXIMATIONS

1. For terms of the form $\frac{d\bar{u}}{dZ}W$:

a. FDM-A and FDM-B, at level $Z = Z_i$:

$$\frac{d\bar{u}}{dZ} W = \frac{1}{2} [W_i \left(\frac{\bar{u}_{i+1} - \bar{u}_i}{Z_{i+1} - Z_i} \right) + W_{i-1} \left(\frac{\bar{u}_i - \bar{u}_{i-1}}{Z_i - Z_{i-1}} \right)]$$

b. FDM-C, at level $Z = Z'_i$:

$$\frac{d\bar{u}}{dZ} W = \frac{1}{2} W_i \left[\left(\frac{\bar{u}_{i+1} - \bar{u}_i}{Z'_{i+1} - Z'_i} \right) + \left(\frac{\bar{u}_i - \bar{u}_{i-1}}{Z'_i - Z'_{i-1}} \right) \right]$$

2. For terms of the form $\frac{\partial \bar{T}}{\partial Z}W$:

a. FDM-A, at level $Z = Z_i$:

$$\frac{\partial \bar{T}}{\partial Z} W = \frac{1}{2} [W_i \left(\frac{\bar{T}_{i+1} - \bar{T}_i}{Z_{i+1} - Z_i} \right) + W_{i-1} \left(\frac{\bar{T}_i - \bar{T}_{i-1}}{Z_i - Z_{i-1}} \right)]$$

b. FDM-B, at level $Z = Z_i$:

$$\frac{\partial \bar{T}}{\partial Z} W = \frac{1}{2} W_i \left[\left(\frac{\bar{T}_{i+1} - \bar{T}_i}{Z'_{i+1} - Z'_i} \right) + \left(\frac{\bar{T}_i - \bar{T}_{i-1}}{Z'_i - Z'_{i-1}} \right) \right]$$

c. FDM-C, at level $Z = Z_i$:

$$\frac{\partial \bar{T}}{\partial Z} W = \frac{1}{2} W_i \left[\left(\frac{\bar{T}_{i+1} - \bar{T}_{i-1}}{Z'_{i+1} - Z'_i} \right) + \left(\frac{\bar{T}_i - \bar{T}_{i-1}}{Z'_i - Z'_{i-1}} \right) \right]$$

3. For terms of the form $\frac{d\bar{u}}{dZ}V$:

a. FDM-A, at level $Z = Z_i$:

$$\frac{d\bar{u}}{dZ} V = \frac{1}{2} V_i \left[\left(\frac{\bar{u}_{i+1} - \bar{u}_i}{Z_{i+1} - Z_i} \right) + \left(\frac{\bar{u}_i - \bar{u}_{i-1}}{Z_i - Z_{i-1}} \right) \right]$$

b. FDM-B, at level $Z = Z'_i$:

$$\frac{d\bar{u}}{dZ} V = \frac{1}{2} (V_{i+1} + V_i) \left(\frac{\bar{u}_{i+1} - \bar{u}_i}{Z_{i+1} - Z_i} \right)$$

c. FDM-C, at level $Z = Z'_i$:

$$\frac{d\bar{u}}{dZ} V = \frac{1}{2} V_i \left[\left(\frac{\bar{u}_{i+1} - \bar{u}_i}{Z'_{i+1} - Z'_i} \right) + \left(\frac{\bar{u}_i - \bar{u}_{i-1}}{Z'_i - Z'_{i-1}} \right) \right]$$

APPENDIX B. GALERKIN FORM OF FEM-A PROGNOSTIC EQUATIONS

1. Vorticity Equations (2.25) and (2.26):

$$\begin{aligned} \sum_{j=i-1}^{i+1} \frac{dA_1^j}{dt} \int_{Z_0}^{Z_T} \phi_j \phi_i dZ = -f \sum_{j=i-1}^{i+1} D_1^j \int_{Z_0}^{Z_T} \phi_j \phi_i dZ \\ - \mu \sum_{k=i-1}^{i+1} \bar{u}^k \sum_{j=i-1}^{i+1} A_2^j \int_{Z_0}^{Z_T} \phi_j \phi_k \phi_i dZ - \beta \sum_{j=i-1}^{i+1} V_1^j \int_{Z_0}^{Z_T} \phi_j \phi_i dZ. \end{aligned} \quad (B.1)$$

$$\begin{aligned} \sum_{j=i-1}^{i+1} \frac{dA_2^j}{dt} \int_{Z_0}^{Z_T} \phi_j \phi_i dZ = -f \sum_{j=i-1}^{i+1} D_2^j \int_{Z_0}^{Z_T} \phi_j \phi_i dZ \\ + \mu \sum_{k=i-1}^{i+1} \bar{u}^k \sum_{j=i-1}^{i+1} A_1^j \int_{Z_0}^{Z_T} \phi_j \phi_k \phi_i dZ - \beta \sum_{j=i-1}^{i+1} V_2^j \int_{Z_0}^{Z_T} \phi_j \phi_i dZ. \end{aligned} \quad (B.2)$$

Note that in these equations, and the equations that follow, the basis functions are functions of Z ($\phi_i = \phi_i(Z)$ and $\psi_i = \psi_i(Z)$). All of the other variables, A , D , H , Q , T , u , U , V , and W , are functions of time ($A_i = A_i(t)$, $D_i = D_i(t)$, $H_i = H_i(t)$, $Q_i = Q_i(t)$, $T_i = T_i(t)$, $u_i = u_i(t)$, $U_i = U_i(t)$, $V_i = V_i(t)$, $W_i = W_i(t)$).

2. Divergence Equations (2.27) and (2.28):

$$\begin{aligned}
\sum_{j=i-1}^{i+1} \frac{dD_1^j}{dt} \int_{Z_0}^{Z_\tau} \phi_j \phi_i dZ &= f \sum_{j=i-1}^{i+1} A_1^j \int_{Z_0}^{Z_\tau} \phi_j \phi_i dZ \\
&- \mu \sum_{k=i-1}^{i+1} \bar{u}^k \sum_{j=i-1}^{i+1} D_2^j \int_{Z_0}^{Z_\tau} \phi_j \phi_k \phi_i dZ - \beta \sum_{j=i-1}^{i+1} U_1^j \int_{Z_0}^{Z_\tau} \phi_j \phi_i dZ \\
&- \mu \sum_{k=i-1}^{i+1} \bar{u}^k \sum_{j=i-1}^{i+1} W_2^j \int_{Z_0}^{Z_\tau} \frac{d\phi_k}{dZ} \phi_j \phi_i dZ + \mu^2 \sum_{j=i-1}^{i+1} H_1^j \int_{Z_0}^{Z_\tau} \phi_j \phi_i dZ.
\end{aligned} \tag{B.3}$$

$$\begin{aligned}
\sum_{j=i-1}^{i+1} \frac{dD_2^j}{dt} \int_{Z_0}^{Z_\tau} \phi_j \phi_i dZ &= f \sum_{j=i-1}^{i+1} A_2^j \int_{Z_0}^{Z_\tau} \phi_j \phi_i dZ \\
&+ \mu \sum_{k=i-1}^{i+1} \bar{u}^k \sum_{j=i-1}^{i+1} D_1^j \int_{Z_0}^{Z_\tau} \phi_j \phi_k \phi_i dZ - \beta \sum_{j=i-1}^{i+1} U_2^j \int_{Z_0}^{Z_\tau} \phi_j \phi_i dZ \\
&- \mu \sum_{k=i-1}^{i+1} \bar{u}^k \sum_{j=i-1}^{i+1} W_1^j \int_{Z_0}^{Z_\tau} \frac{d\phi_k}{dZ} \phi_j \phi_i dZ + \mu^2 \sum_{j=i-1}^{i+1} H_2^j \int_{Z_0}^{Z_\tau} \phi_j \phi_i dZ.
\end{aligned} \tag{B.4}$$

3. Thermodynamic Equations (2.29) and (2.30):

$$\begin{aligned}
 \sum_{j=i-1}^{i+1} \frac{dT_1^j}{dt} \int_{Z_0}^{Z_\tau} \phi_j \phi_i dZ &= -\mu \sum_{k=i-1}^{i+1} \bar{u}^k \sum_{j=i-1}^{i+1} T_2^j \int_{Z_0}^{Z_\tau} \phi_j \phi_k \phi_i dZ \\
 &+ \frac{f}{R} \sum_{k=i-1}^{i+1} \bar{u}^k \sum_{j=i-1}^{i+1} v_1^j \int_{Z_0}^{Z_\tau} \frac{d\phi_k}{dZ} \phi_j \phi_i dZ \\
 &- \sum_{k=i-1}^{i+1} \bar{T}^k \sum_{j=i-1}^{i+1} w_1^j \int_{Z_0}^{Z_\tau} \frac{d\phi_k}{dZ} \psi_j \phi_i dZ + \sum_{j=i-1}^{i+1} Q_1^j \int_{Z_0}^{Z_\tau} \phi_j \phi_i dZ.
 \end{aligned} \tag{B.5}$$

$$\begin{aligned}
 \sum_{j=i-1}^{i+1} \frac{dT_2^j}{dt} \int_{Z_0}^{Z_\tau} \phi_j \phi_i dZ &= \mu \sum_{k=i-1}^{i+1} \bar{u}^k \sum_{j=i-1}^{i+1} T_1^j \int_{Z_0}^{Z_\tau} \phi_j \phi_k \phi_i dZ \\
 &+ \frac{f}{R} \sum_{k=i-1}^{i+1} \bar{u}^k \sum_{j=i-1}^{i+1} v_2^j \int_{Z_0}^{Z_\tau} \frac{d\phi_k}{dZ} \phi_j \phi_i dZ \\
 &- \sum_{k=i-1}^{i+1} \bar{T}^k \sum_{j=i-1}^{i+1} w_2^j \int_{Z_0}^{Z_\tau} \frac{d\phi_k}{dZ} \psi_j \phi_i dZ + \sum_{j=i-1}^{i+1} Q_2^j \int_{Z_0}^{Z_\tau} \phi_j \phi_i dZ.
 \end{aligned} \tag{B.6}$$

APPENDIX C. BASIS FUNCTION EQUATIONS FOR FEM-A

1. Notation:

$$\Delta_i = Z_i - Z_{i-1}$$

$$\Delta'_i = Z'_i - Z'_{i-1}$$

$$\xi = Z - Z_i$$

2. For the general case:

$$\begin{aligned}\phi_i(\xi) &= \frac{\xi - \Delta'_i + .5\Delta'_{i-1}}{.5(\Delta'_i + \Delta'_{i-1})} & -\Delta'_2 - \frac{\Delta'_{i-1}}{2} \leq \xi \leq -\frac{\Delta'_i}{2} \\ &= \frac{-\xi + .5\Delta'_{i+1}}{.5(\Delta'_i + \Delta'_{i+1})} & -\frac{\Delta'_i}{2} \leq \xi \leq \frac{\Delta'_{i+1}}{2}\end{aligned}$$

for any i sufficiently far from the boundaries, $3 \leq i \leq n$.

$$\begin{aligned}\psi_i(\xi) &= \frac{\xi + \Delta'_i}{\Delta'_i} & -\Delta'_i \leq \xi \leq 0 \\ &= \frac{-\xi + \Delta'_{i+1}}{\Delta'_{i+1}} & 0 \leq \xi \leq \Delta'_{i+1}\end{aligned}$$

for $2 \leq i \leq n$.

3. For special cases, $\phi_1, \phi_2, \phi_{n-1}, \phi_{n-2}, \psi_1, \psi_{n-1}$:

$$\phi_1(\xi) = \frac{-\xi + .5\Delta'_2}{\Delta'_2}$$

$$\begin{aligned}\phi_2(\xi) &= \frac{\xi + 1.5\Delta'_2}{\Delta'_2} & -\Delta'_2 \leq \xi \leq -.5\Delta'_2 \\ &= \frac{-\xi + .5\Delta'_3}{.5(\Delta'_2 + \Delta'_3)} & -.5\Delta'_2 \leq \xi \leq .5\Delta'_3\end{aligned}$$

$$\psi_1(\xi) = \frac{-\xi + \Delta'_2}{\Delta'_2} \quad 0 \leq \xi \leq \Delta'_2$$

$$\psi_{n+1}(\xi) = \frac{\xi + \Delta'_{n+1}}{\Delta'_{n+1}}$$

$$\begin{aligned} \phi_{n+1}(\xi) &= \frac{\xi - \Delta'_{n+1} + .5\Delta'_n}{.5(\Delta'_{n+1} + \Delta'_n)} & -\frac{\Delta'_n}{2} - \Delta'_{n+1} \leq \xi \leq -\frac{\Delta'_{n+1}}{2} \\ &= \frac{-\xi + .5\Delta'_{n+1}}{\Delta'_{n+1}} & 0 \leq \xi \leq -\Delta'_{n+1} \end{aligned}$$

$$\phi_{n+2}(\xi) = \frac{\xi + .5\Delta'_{n+1}}{\Delta'_{n+1}}$$

APPENDIX D. GALERKIN FORM OF FEM-B PROGNOSTIC EQUATIONS

1. The vorticity equations have the same form as the vorticity equations for model FEM-A, equations (B.1) and (B.2).
2. The divergence equations are the same as the divergence equations in model FEM-A, equations (B.3) and (B.4).
3. Thermodynamic Equations (2.29) and (2.30):

$$\begin{aligned}
 \sum_{j=-1}^{i+1} \frac{dT_1^j}{dt} \int_{Z_0}^{Z_T} \psi_j \psi_i dZ &= -\mu \sum_{k=-1}^{i+1} \bar{u}^k \sum_{j=-1}^{i+1} T_2^j \int_{Z_0}^{Z_T} \psi_j \phi_k \psi_i dZ \\
 &+ \frac{f}{R} \sum_{k=-1}^{i+1} \bar{u}^k \sum_{j=-1}^{i+1} V_1^j \int_{Z_0}^{Z_T} \frac{d\phi_k}{dZ} \phi_j \psi_i dZ \\
 &- \sum_{k=-1}^{i+1} \bar{T}^k \sum_{j=-1}^{i+1} W_1^j \int_{Z_0}^{Z_T} \frac{d\psi_k}{dZ} \psi_j \psi_i dZ + \sum_{j=-1}^{i+1} Q_1^j \int_{Z_0}^{Z_T} \psi_j \psi_i dZ.
 \end{aligned} \tag{D.1}$$

$$\begin{aligned}
\sum_{j=1}^{i+1} \frac{dT_2^j}{dt} \int_{Z_0}^{Z_T} \psi_j \psi_i dZ &= \mu \sum_{k=1}^{i+1} \bar{u}^k \sum_{j=1}^{i+1} T_1^j \int_{Z_0}^{Z_T} \psi_j \phi_k \psi_i dZ \\
&+ \frac{f}{R} \sum_{k=1}^{i+1} \bar{u}^k \sum_{j=1}^{i+1} V_2^j \int_{Z_0}^{Z_T} \frac{d\phi_k}{dZ} \phi_j \psi_i dZ \\
&- \sum_{k=1}^{i+1} \bar{T}^k \sum_{j=1}^{i+1} W_2^j \int_{Z_0}^{Z_T} \frac{d\psi_k}{dZ} \psi_j \psi_i dZ + \sum_{j=1}^{i+1} Q_2^j \int_{Z_0}^{Z_T} \psi_j \psi_i dZ.
\end{aligned} \tag{D.2}$$

Note that in these equations the basis functions are functions of Z ($\phi_i = \phi_i(Z)$ and $\psi_i = \psi_i(Z)$). All of the other variables, Q , T , u , U , V , and W , are functions of time ($Q_i = Q_i(t)$, $T_i = T_i(t)$, $u_i = u_i(t)$, $U_i = U_i(t)$, $V_i = V_i(t)$, $W_i = W_i(t)$).

APPENDIX E. GALERKIN FORM OF FEM-C PROGNOSTIC EQUATIONS

1. The vorticity equations have the same form as the vorticity equations for model FEM-A, equations (B.1) and (B.2).

2. Divergence Equations (2.27) and (2.28):

$$\begin{aligned}
 \sum_{j=i-1}^{i+1} \frac{dD_1^j}{dt} \int_{Z_0}^{Z_\tau} \phi_j \phi_i dZ &= f \sum_{j=i-1}^{i+1} A_1^j \int_{Z_0}^{Z_\tau} \phi_j \phi_i dZ \\
 - \mu \sum_{k=i-1}^{i+1} \bar{u}^k \sum_{j=i-1}^{i+1} D_2^j \int_{Z_0}^{Z_\tau} \phi_j \phi_k \phi_i dZ &- \beta \sum_{j=i-1}^{i+1} U_1^j \int_{Z_0}^{Z_\tau} \phi_j \phi_i dZ \\
 - \mu \sum_{k=i-1}^{i+1} \bar{u}^k \sum_{j=i-1}^{i+1} W_2^j \int_{Z_0}^{Z_\tau} \frac{d\phi_k}{dZ} \phi_j \phi_i dZ &+ \mu^2 \sum_{j=i-1}^{i+1} H_1^j \int_{Z_0}^{Z_\tau} \phi_j \phi_i dZ.
 \end{aligned} \tag{E.1}$$

$$\begin{aligned}
\sum_{j=i-1}^{i+1} \frac{dD_2^j}{dt} \int_{Z_0}^{Z_\tau} \phi_j \phi_i dZ &= f \sum_{j=i-1}^{i+1} A_2^j \int_{Z_0}^{Z_\tau} \phi_j \phi_i dZ \\
&+ \mu \sum_{k=i-1}^{i+1} \bar{u}^k \sum_{j=i-1}^{i+1} D_1^j \int_{Z_0}^{Z_\tau} \phi_j \phi_k \phi_i dZ - \beta \sum_{j=i-1}^{i+1} U_2^j \int_{Z_0}^{Z_\tau} \phi_j \phi_i dZ \\
&+ \mu \sum_{k=i-1}^{i+1} \bar{u}^k \sum_{j=i-1}^{i+1} W_1^j \int_{Z_0}^{Z_\tau} \frac{d\phi_k}{dZ} \phi_j \phi_i dZ + \mu^2 \sum_{j=i-1}^{i+1} H_2^j \int_{Z_0}^{Z_\tau} \phi_j \phi_i dZ. \quad (E.2)
\end{aligned}$$

Note that in these equations, and the equations that follow, the basis functions are functions of Z ($\phi_i = \phi_i(Z)$ and $\psi_i = \psi_i(Z)$). All of the other variables, A , D , H , Q , T , u , U , V and W , are functions of time ($A_i = A_i(t)$, $D_i = D_i(t)$, $H_i = H_i(t)$, $Q_i = Q_i(t)$, $T_i = T_i(t)$, $u_i = u_i(t)$, $U_i = U_i(t)$, $V_i = V_i(t)$ and $W_i = W_i(t)$).

3. Thermodynamic Equations (2.29) and (2.30):

$$\begin{aligned}
\sum_{j=i-1}^{i+1} \frac{dT_1^j}{dt} \int_{Z_0}^{Z_\tau} \phi_j \phi_i dZ &= -\mu \sum_{k=i-1}^{i+1} \bar{u}^k \sum_{j=i-1}^{i+1} T_2^j \int_{Z_0}^{Z_\tau} \phi_j \phi_k \phi_i dZ \\
&+ \frac{f}{R} \sum_{k=i-1}^{i+1} \bar{u}^k \sum_{j=i-1}^{i+1} V_1^j \int_{Z_0}^{Z_\tau} \frac{d\phi_k}{dZ} \phi_j \phi_i dZ \\
&- \sum_{k=i-1}^{i+1} \bar{T}^k \sum_{j=i-1}^{i+1} W_1^j \int_{Z_0}^{Z_\tau} \frac{d\phi_k}{dZ} \phi_j \phi_i dZ + \sum_{j=i-1}^{i+1} Q_1^j \int_{Z_0}^{Z_\tau} \phi_j \phi_i dZ. \quad (E.3)
\end{aligned}$$

$$\begin{aligned}
\sum_{j=i-1}^{i+1} \frac{dT_2^j}{dt} \int_{Z_0}^{Z_T} \phi_j \phi_i dZ &= \mu \sum_{k=i-1}^{i+1} \bar{u}^k \sum_{j=i-1}^{i+1} T_1^j \int_{Z_0}^{Z_T} \phi_j \phi_k \phi_i dZ \\
&+ \frac{f}{R} \sum_{k=i-1}^{i+1} \bar{u}^k \sum_{j=i-1}^{i+1} v_2^j \int_{Z_0}^{Z_T} \frac{d\phi_k}{dZ} \phi_j \phi_i dZ \\
&- \sum_{k=i-1}^{i+1} \bar{T}^k \sum_{j=i-1}^{i+1} w_2^j \int_{Z_0}^{Z_T} \frac{d\phi_k}{dZ} \phi_j \phi_i dZ + \sum_{j=i-1}^{i+1} Q_2^j \int_{Z_0}^{Z_T} \phi_j \phi_i dZ.
\end{aligned} \tag{E.4}$$

LIST OF REFERENCES

- Arakawa, A., 1984: Vertical differencing of filtered models. Proc. of European Centre for Medium Range Weather Forecasts: 1983 Seminar on Numerical Method for Weather Prediction. 1, 183-206.
- _____, and V. R. Lamb, 1977: Computational design of the basic dynamical processes of the UCLA general circulation model. *Methods of Computational Physics*, 17, 173-265.
- Charney, J. G., and N. A. Phillips, 1953: Numerical integration of the quasigeostrophic equations for barotropic and dimple baroclinic flows. *J. of Meteor.*, 10, 71-79.
- Cullen, M. J. P., 1973: A simple finite-element method for meteorological problems. *J. Inst. Math Applies.*, 11, 15-31
- Eady, E. T., 1949: Long waves and cyclone waves. *Tellus.*, 1, no. 3, 33-52.
- Farrell, B., 1985: Transient growth of damped baroclinic waves. *J. Atmos. Sci.*, 42, 2718-2727.
- Gall, R. L., 1976: A comparison of linear baroclinic theory with the eddy statistics of a general circulation model. *J. Atmos. Sci.*, 33, 349-373.
- Gray, W. G., and G. F. Pinder, 1976: An analysis of the numerical solution of the transport equation. *Water Resour. Res.*, 12, 547.
- Haltiner, G. J., and R. T. Williams, 1980: Numerical Prediction and Dynamic Meteorology. John Wiley and Sons, Inc., 477pp.
- Hinsman, D. E., 1975: Application of a finite element method to the barotropic primitive equations. M. S. Thesis, Naval Postgraduate School, Monterey, CA, 116pp.
- Hoskins, B. J., and F. Bretherton, 1972: Atmospheric frontogenesis models: Mathematical formulation and solution. *J. Atmos. Sci.*, 29, 11-37.
- Jordan, M. S., 1985: A comparison of six vertical discretization schemes. M. S. Thesis, Naval Postgraduate School, Monterey, CA, 174pp.
- Lorenz, E. N., 1960: Energy and numerical weather prediction. *Tellus*, 12, 364-373.
- Neta, B., and R. T. Williams, 1986: Stability and phase speed for various finite element formulations of the advection equation. *Computers and Fluids*, 14, 393-410.
- _____, _____, and D. E. Hinsman, 1986: Studies in a shallow water fluid model with topography in Numerical Mathematics and Applications (R. Vichevetsky, J. Vignes, eds.). *Elsevier Sci. Pub.*, 347-354.

- Satyamurty, P., V. B. Rao and A. D. Moura, 1982: Subsynoptic-scale baroclinic instability. *J. Atmos. Sci.*, **39**, 1052-1061.
- Schoenstadt, A. L., 1980: A transfer function analysis of numerical schemes used to simulate geostrophic adjustment. *Mo. Wea. Rev.*, **108**, 1245-1259.
- Shapiro, B. B., 1987: A study of finite difference and finite element vertical discretization schemes for baroclinic prediction equations. M. S. Thesis, Naval Postgraduate School, Monterey, CA, 86pp.
- Staniforth, A. N., and R. W. Daley, 1977: A finite-element formulation for the vertical discretization of sigma-coordinate primitive equation models. *Mo. Wea. Rev.*, **105**, 1108-1118.
- _____, _____, 1979: A baroclinic finite-element model for regional forecasting with the primitive equations. *Mo. Wea. Rev.*, **107**, 107-121.
- Staniforth, A. N., and H. L. Mitchell, 1977: A semi-implicit finite-element barotropic model. *Mo. Wea. Rev.*, **105**, 154-169.
- _____, _____, 1978: A variable-resolution finite-element technique for regional forecasting with the primitive equations. *Mo. Wea. Rev.*, **106**, 439-447.
- Tokioka, T., 1978: Some considerations on vertical differencing. *J. of the Met. Soc. of Japan*, **56**, 98-111.
- Williams, R. T., 1967: Atmospheric frontogenesis: A numerical experiment. *J. Atmos. Sci.*, **24**, 627-641.
- Winninghoff, F., 1968: On the adjustment toward a geostrophic balance in a simple primitive equation model with application to the problem on initialization and objective analysis. Doctoral dissertation, UCLA.
- Zienkiewicz, O. C., 1977: The Finite Element Method. McGraw-Hill, New York, 787 pp.

INITIAL DISTRIBUTION LIST

	No. Copies
1. Defense Technical Information Center Cameron Station Alexandria, VA 22304-6145	2
2. Library, Code 0142 Naval Postgraduate School Monterey, CA 93943-5002	2
3. Meteorology Reference Center, (Code 63) Department of Meteorology Naval Postgraduate School Monterey, CA 93943-5000	1
4. Chairman (Code 63Rd) Department of Meteorology Naval Postgraduate School Monterey, CA 93943-5000	1
5. Dr. Roger T. Williams. (Code 63Wu) Department of Meteorology Naval Postgraduate School Monterey, CA 93943-5000	5
6. Professor B. Neta (Code 53Nd) Department of Mathematics Naval Postgraduate School Monterey, CA 93943-5000	5
7. USAF ETAC LD Air Weather Service Technical Library Scott AFB, IL 62225-5000	1
8. Program Manager (AFIT CIR) Air Force Institute of Technology Wright-Patterson AFB, OH 45433	1
9. Commander Air Weather Service Scott AFB, IL 62225	1
10. Commander Air Force Global Weather Central Offutt AFB, NE 68113	1
11. Commander Naval Oceanography Command	1

- NSTL Station
Bay St. Louis, MS 39522
12. Chief of Naval Research 1
800 N. Quincy Street
Arlington, VA 22217-5000
 13. Dr. Paul Twitchell 1
Office of Naval Research
800 N. Quincy Street
Arlington, VA 22217-5000
 14. Commanding Officer 1
Naval Environmental Prediction Research Facility
Monterey, CA 93943-5006
 15. Commanding Officer 1
Fleet Numerical Oceanography Center
Monterey, CA 93943-5005
 16. Commanding Officer 1
Naval Ocean Research and Development Activity
NSTL Station
Bay St. Louis, MS 39522
 17. Capt. Bruce G. Shapiro, USAF 1
Hq Air Force Global Weather Central
Offutt, AFB NE 86113
 18. Capt. Donn E. Sloniker, USAF 2
General Delivery
APO Miami 34001-5000
 19. Dr. T. Rosmond 1
Naval Environmental Prediction Research Facility
Monterey, CA 93943-5006
 20. Professor R. L. Elsberry (Code 63Es) 1
Department of Meteorology
Naval Postgraduate School
Monterey, CA 93943-5000
 21. Professor A. L. Schoenstadt (Code 53Zh) 1
Department of Mathematics
Naval Postgraduate School
Monterey, CA 93943-5000
 22. Professor R. E. Newton (Code 69Ne) 1
Department of Mechanical Engineering
Naval Postgraduate School
Monterey, CA 93943-5000

23. Professor M. A. Rennick (Code 63Rn) 1
 Department of Meteorology
 Naval Postgraduate School
 Monterey, CA 93943-5000

24. Dr. J. Steppeler 1
 European Center for Medium Range Weather Forecasts
 Shinfield Park
 Reading, Berkshire RG2 9AX
 England

25. Dr. M.J.P. Culler 1
 Meteorological Office
 Bracknell, Berks, United Kingdom
 Pentagon
 Washington, D.C. 20350-1000

26. Dr. Robert L. Lee 1
 Atmospheric and Geophysical Science Division
 University of California
 P.O. Box 808
 Livermore, CA 94550

27. Dr. N. A. Phillips 1
 National Meteorological Center/NOAA
 World Weather Building
 Washington, D.C. 20233

28. Dr. Y. Sasake 1
 Department of Meteorolgy
 University of Oklahoma
 Norman, OK 73069

29. Dr. Andrew Staniforth 1
 Recherche-en-Prevision Numerique
 West Isle Office Tower, 5 ieme etage
 2121 route Trans-Canada
 Dorval, Quebec H9P1J3, Canada

30. Professor O. C. Zienkiewicz 1
 Head of Civil Engineering Department
 Applied Science Building
 Singleton Park
 Swansea SA2 8PP
 United Kingdom

31. Dr. T. Rosmond 1
 Naval Environmental Prediction Research Facility
 Monterey, CA 93943-5006